Centrale à inertie (INS) miniature combinée au système de positionnement par satellites (GNSS) pour la gravimétrie statique et mobile : une méthode opportuniste pour les applications géophysiques et environnementales

Benjamin Beirens

Université Fédérale
Toulouse Midi-Pyrénées

THÈSE

En vue de l'obtention du
DOCTORAT DE L'UNIVERSITÉ DE TOULOUSE

Délivré par l'Université Toulouse 3 - Paul Sabatier

Présentée et soutenue par

Benjamin BEIRENS

Le 11 octobre 2023

Centrale à inertie (INS) miniature combinée au système de positionnement par satellites (GNSS) pour la gravimétrie statique et mobile: Une méthode opportuniste pour les applications géophysiques et environnementales

---

Ecole doctorale : **SDU2E - Sciences de l'Univers, de l'Environnement et de l'Espace**

Spécialité : **Surfaces et interfaces continentales, Hydrologie**

Unité de recherche :
GET - Geosciences Environnement Toulouse

Thèse dirigée par
José DARROZES et Guillaume RAMILLIEN

Jury

M. Minh CUONG HA, Rapporteur
Mme Lucia SEOANE, Examinatrice
M. Guillaume RAMILLIEN, Co-directeur de thèse
M. Fréderic FRAPPART, Président

Acknowledgments

I would like to express my deepest gratitude to José Darrozes and Guillaume Ramillien, my supervisors without whom this work would not have been possible. More specifically, for all the meetings, the ideas they gave me to try when I was stuck, the theoretical and practical knowledge they taught me, the experiments they organized and their help in writing this thesis. I would like to express my appreciation to the Géosciences Environment Toulouse laboratory and the SDU2E doctorate school for the resources that are made available for PhD students like myself and in particular Marc De Rafelis and Geneviève Soucail to guide me along the way. Special thanks to the people that helped during the experiments, Lucia Seoane and Patrice Médina, without whose technical aid those experiments would not have been possible. I would like to sincerely thank Mr. Frappart F., Mr. CUONG HA M. and Mr. GRANDE GIL J.A. who accepted to be rapporteurs for this thesis and their time in order to carefully read my work and share with me their remarks. I would also like to thank Mrs. SEOANE L. and Mrs. BONIFACE K. for agreeing to be part of the jury. Lastly, I would be remiss in not mentioning Colline, Karel-Jan, Betty and my parents, who supported me and pushed me to continue when I wanted to give up.

Summary

List of Figures

No. **Title** **Page No.**

List of Tables

Acronyms

AHRS Attitude and Heading Reference System
ANPP Advanced Navigation Packet Protocol
CHAMP CHAllenging Minisatellite Payload
CWT Continuous Wavelet Transform
DEM Digital Elevation Model
DTM Digital Terrain Model
DWT Discrete Wavelet Transform
FFT Fast Fourier Transform
GET Géosciences Environnement Toulouse
GNSS Global Navigation Satellite System
GOCE Gravity field and steady-state Ocean Circulation
GPS Global Positioning System
GRACE Gravity Recovery and Climate Experiment
IFFT Inverse Fourier Transform
IGN Institut Géographique Nationale
INS Inertial Navigation System
LAERO Laboratoire d'aérologie
MEMS Micro Electronic Mechanical System
MSL Mean Sea Level
NED North East Down
RMS Root Mean Square
RMSE Root Mean Square Error
SST-HL Satellite-to-Satellite Tracking High Low
SST-LL Satellite-to-Satellite Tracking Low Low
XWT Cross Wavelet Transform

Résumé français

La gravimétrie consiste à mesurer et à interpréter les variations du champ de gravité terrestre en termes de contrastes de densité et donc de structures. Bien que les grandes longueurs d'onde de la gravité soient bien restituées par les missions satellites dédiées dont les plus récentes à basses altitudes (300-400 km) sont CHAMP, GRACE et GOCE, et que les gravimètres absolus réalisent des mesures très précises mais ponctuelles, les informations relatives à la pesanteur aux échelles spatiales intermédiaires de la centaine de mètres à quelques centaines de kilomètres, restent inaccessibles. L'utilisation de centrales inertielles de types « SPATIAL » et « MOTUS » (Advanced Navigation) qui enregistrent les accélérations suivant trois axes – par conséquent de la composante verticale de la gravité - à une cadence d'échantillonnage élevée (jusqu'à 1000 Hz), permet d'accéder à ces variations dans la gamme de longueurs d'onde manquantes, en particulier si elles sont installées à bord d'une plateforme (voiture, drone, avion). Mon travail de thèse est la mise en œuvre de tels systèmes d'acquisition opportunistes pour la gravimétrie mobile afin de restituer les variations spatio-temporelles de la gravité. Mes premiers tests sur la fréquence d'échantillonnage ont mis en évidence le bruit haute fréquence d'origine thermique dû à l'échauffement des composants électroniques de la centrale, qui peut être corrigé. Dans un premier temps, les effets thermiques sur l'accélération ont été ajustés en utilisant une simple fonction linéaire des variations de température, pour corriger des données accélérométriques acquises à bord d'une voiture entre le laboratoire GET à Toulouse et le barrage des Cammazes (81) situé dans la Montagne Noire. Une fois corrigées empiriquement des effets de la température interne, ces données ont été comparées aux mesures précises d'un gravimètre absolu et ont confirmé la décroissance de la pesanteur avec l'altitude. Dans un second temps, des tests d'acquisition en mode "statique" (au repos) ont montré que les périodes des marées principales à 12h00 et 24h00 peuvent être extraites du spectre des enregistrements accélérométriques à 5 minutes puis reconstruites pour être comparées aux valeurs théoriques du logiciel Tsoft, un simulateur des variations de la gravité dues aux marées terrestres, montrant une excellente corrélation en phase et

relativement bonne en amplitude. Installée sur le drone de la société BOREAL lors de campagnes à Lannemezan puis sur un site d'éoliennes, la centrale inertielle a enregistré l'influence prédominante du catapultage, puis des virages et des vibrations mécaniques du moteur thermique sous forme d'un bruit coloré réparti sur plusieurs fréquences du spectre des mesures. Même si l'exploitation de ces mesures accélérométriques aéroportées représente encore un vrai défi et nécessite des investigations supplémentaires, leur filtrage spectral sur des portions rectilignes de sa trajectoire ont révélé les variations verticales de la gravité dus les changements d'altitude du drone.

Abstract English

Gravimetry consists of measuring and interpreting variations in the earth's gravity field in terms of density contrasts and therefore of structures. Although the long wavelengths of gravity are well restored by the dedicated satellite missions, the most recent of which at low altitudes (300-400 km) are CHAMP, GRACE and GOCE, and the absolute gravimeters carry out very precise but specific measurements, information relating to gravity at intermediate spatial scales of a hundred meters to a few hundred kilometers, remains hard to cover. The use of "SPATIAL" and "MOTUS" (Advanced Navigation) type inertial measurement units which record accelerations along three axes - and therefore the vertical component of gravity - at a high sampling rate (up to 1000 Hz), makes it possible to access these variations in the range of missing wavelengths, in particular if they are installed on board a mobile platform (car, drone, plane). My thesis work is the implementation of such opportunistic acquisition systems for mobile gravimetry in order to restore the spatio-temporal variations of gravity. My first tests on the sampling frequency highlighted the high frequency noise of thermal origin due to the heating of the electronic components of the control unit, which can be corrected. First, the thermal effects on acceleration were adjusted using a simple linear function of temperature variations, to correct accelerometric data acquired on board a car between the GET laboratory in Toulouse and the Cammazes dam (81) located in the *Montagne Noire.* Once corrected empirically for the effects of internal temperature, these data were compared with precise measurements of an absolute gravimeter and confirmed the decrease in gravity with altitude. In a second step, acquisition tests in "static" mode (at rest) showed that the periods of the main tides at 12h and 24h can be extracted from the spectrum of accelerometric recordings at 5 minutes and then reconstructed to be compared with theoretical values of the Tsoft software, a simulator of the variations of gravity due to the earth's tides, showing an excellent correlation in phase and relatively good in amplitude. Installed on the BOREAL company's drone during flights at Lannemezan and then at a wind turbine site, the inertial unit recorded the predominant influence of the catapult launch, then the turns and mechanical vibrations of the engine in the form of a colored

noise distributed over several frequencies of the measurement spectrum. Even if the exploitation of these airborne accelerometric measurements still represents a real challenge and requires additional investigations, their spectral filtering on rectilinear portions of its trajectory revealed the vertical variations of gravity due to the altitude changes of the drone.

Abstract Nederlands

Gravimetrie is het meten en interpreteren van variaties in het zwaartekrachtveld van de aarde in termen van dichtheid contrasten en dus van structuren. Hoewel de lange golflengten van de zwaartekracht goed worden gemeten door de speciale satelliet missies, waarvan de meest recente op lage hoogte (300-400 km) CHAMP, GRACE en GOCE zijn, en de absolute gravimeters voeren zeer nauwkeurige metingen uit, maar specifieke informatie met betrekking tot tot de zwaartekracht op tussenliggende ruimtelijke schalen van honderd meter tot enkele honderden kilometers, blijft ontoegankelijk. Het gebruik van traagheidsnavigatiesystemen van het type "SPATIAL" en "MOTUS" (Advanced Navigation) die versnellingen langs drie assen registreren - en dus de verticale component van de zwaartekracht - met een hoge bemonsteringsfrequentie (tot 1000 Hz), maakt het mogelijk om toegang te krijgen tot deze variaties in het bereik van ontbrekende golflengten, met name als ze aan boord van een platform (auto, drone, vliegtuig) zijn geïnstalleerd. Mijn afstudeerwerk is de implementatie van dergelijke opportunistische acquisitie systemen voor mobiele gravimetrie om de spatio-temporele variaties van de zwaartekracht te meten. Mijn eerste tests met de bemonsteringsfrequentie wezen op de hoogfrequente ruis van thermische oorsprong als gevolg van de verwarming van de elektronische componenten van de besturingseenheid, die gecorrigeerd kan worden. Eerst werden de thermische effecten op acceleratie aangepast met behulp van een eenvoudige lineaire functie van temperatuurvariaties, om versnelling gegevens te corrigeren die aan boord van een auto tussen het GET-laboratorium in Toulouse en de Cammazes-dam (81) in de *Montagne Noire* waren verkregen. Eenmaal empirisch gecorrigeerd voor de effecten van interne temperatuur, werden deze gegevens vergeleken met nauwkeurige metingen van een absolute gravimeter en bevestigden ze de afname van de zwaartekracht met de hoogte. In een tweede stap toonden acquisitie testen in "statische" modus (in rust) aan dat de perioden van de hoofdgetijden om 12.00 uur en 24.00 uur kunnen worden geëxtraheerd uit het spectrum van versnelling opnames op 5 minuten en vervolgens gereconstrueerd om te worden vergeleken met theoretische waarden van de Tsoft software, een

simulator van de variaties van de zwaartekracht als gevolg van de getijden van de aarde, met een uitstekende correlatie in fase en relatief goede amplitude. Geïnstalleerd op de drone van het bedrijf BOREAL tijdens vluchten in Lannemezan en vervolgens op een windturbine site, registreerde de traagheidsnavigatiesystemen de overheersende invloed van de katapult lancering, vervolgens de draaiingen en mechanische trillingen van de motor in de vorm van een gekleurd geluid verdeeld over verschillende frequenties van het spectrum. Zelfs als de exploitatie van deze versnelling metingen vanuit de lucht nog steeds een echte uitdaging vormt en aanvullend onderzoek vereist, onthulde hun spectrale filtering op rechtlijnige delen van het traject de verticale variaties van de zwaartekracht als gevolg van de hoogteveranderingen van de drone.

CHAPTER 1 Introduction

1.1 Contexte Scientifique (Introduction français)

L'objectif de cette thèse était de travailler avec un Système de Navigation Inertielle (INS) miniature associé à un Système Global de Navigation par Satellite (GNSS), défini ici comme INS/GNSS, deux modèles de Advanced Navigation sont utilisés : SPATIAL et MOTUS . J'étudie la viabilité de l'utilisation de ces instruments pour des applications gravimétriques (analyse de champs variables). Il existe plusieurs méthodes pour étudier la gravité sur Terre. Un gravimètre est un instrument idéal pour les mesures locales car il sera très précis (~10^{-9}m/s²), mais inefficace pour couvrir une grande surface au vu de son processus lent, c'est pourquoi les gravimètres ne couvrent que les courtes longueurs d'onde sur Terre. Les satellites placés en orbite terrestre basse sont utilisés pour étudier en continu le champ de gravité complet de la Terre, mais en raison de la grande distance entre la surface de la Terre et le satellite, la résolution spatiale sera plus faible, c'est pourquoi les satellites ne couvrent que les grandes longueurs d'onde . La gravimétrie mobile (aéroportée/UAV/voiture/bateau) a permis d'obtenir ces longueurs d'onde moyennes. Il est important que la gravimétrie couvre le spectre complet des longueurs d'onde car certains processus physiques ont une échelle spatiale qui ne peut pas être détectée par la gravimétrie par satellite (Flechtner et al., 2021) (la figure 1.1 montre la résolution spatiale et temporelle de certains de ces processus qui influencent le niveau de la mer, qui à son tour change la gravité en mer). La gravimétrie mobile consiste à placer un instrument pouvant servir à la gravimétrie (gravimètre, accéléromètres) à l'intérieur d'un véhicule afin de se déplacer et de mesurer en continu pour couvrir une plus grande surface par rapport à la réalisation de mesures in situ avec un gravimètre, un point à un temps, tout en restant plus près de la surface de la Terre pour améliorer la résolution spatiale. Cependant dans un véhicule en mouvement, il y aura des accélérations présentes (véhicule en accélération, vibrations, ..) qui ne le seraient pas (ou d'amplitude beaucoup plus

faible) lors de la gravimétrie locale ou satellitaire où les forces de frottement atmosphériques sont très faibles (Sanchèz et al., 2023). De ce fait, la position de l'instrument doit être déterminée avec une grande précision à chaque instant, pour supprimer les accélérations qui ne sont pas liées à la gravité. Lors de l'installation de l'instrument à l'intérieur du véhicule, il existe deux options. Un système strapdown, où l'instrument est solidement fixé à la caisse du véhicule (Ayres-Sampaio et al., 2015 & Skaloud et al., 2016), ou une plate-forme de stabilisation, qui va corriger les rotations d'un véhicule (par exemple à l'intérieur d'un avion) et minimiser les vibrations. Avec l'augmentation de la précision du GNSS, la précision de la gravimétrie mobile augmente également.

De nombreuses études ont été faites pour la gravimétrie mobile, dont certaines que je mentionnerai, mais la principale différence entre ces études et mon travail est la méthode opportuniste d'utilisation d'un INS/GNSS (au lieu d'un gravimètre). Un INS/GNSS est normalement utilisé pour la navigation et les accélérations mesurées par les accéléromètres sont utilisées pour mettre à jour et augmenter la précision de la navigation (Farrell et al., 1998) à l'aide d'un filtre de Kalman (Becker A., 2023 & Kim et al., 2019). Au lieu de cela, j'utiliserai ces accélérations pour la gravimétrie, car la gravité est après tout une accélération. La deuxième partie importante de ce travail est la taille de l'instrument qui est utilisé. L'idée était de travailler sur un système qui serait plus petit, moins cher, plus léger et qui pourrait être installé dans un véhicule beaucoup plus petit, par exemple, mais sans s'y limiter, un drone monorotor à voilure fixe, qui peut être déployé rapidement et survoler des zones difficiles, pour atteindre des zones que d'autres véhicules ne peuvent pas atteindre, tout en couvrant les longueurs d'onde intermédiaires (10-100 km) qui ne peuvent pas être couvertes à l'aide de satellites ou de gravimètres en surface (Featherstone, 2003). Le but ultime d'un tel système serait la facilité d'accès et d'utilisation de celui-ci dans différents pays, afin de couvrir rapidement des zones et de détecter les anomalies de gravité variable, par exemple liées à la présence d'un aquifère dans des zones qui ont le plus besoin de sources d'eau (Binley et al., 2015 & Inglezakis et al., 2016). (La figure 1.2 montre les anomalies de gravité dues aux aquifères et la précision requise en fonction de la distance à la source.)

Dans cette thèse, je donnerai un aperçu de l'histoire de la gravité, de l'importance de celle-ci qui a conduit au développement de différents modèles terrestres, qui à leur tour, ont été la clé de la conquête spatiale. Cette expansion rapide des satellites non gravitationnels (par exemple SWARM) et gravitaires (par exemple GOCE, GRACE) a ensuite ouvert la voie à une couverture mondiale du champ de gravité statique/variable de la Terre, conduisant à la création du modèle du géoïde, incorporé dans le modèles pour être plus précis. Le modèle du géoïde montre l'importance de la gravimétrie et comment les anomalies de gravité nous renseignent sur les variations temporelles et spatiales de la Terre (Schwarz et al., 1996 & Ramillien et al., 2021). J'aborderai brièvement certaines de ces variations, comme l'étude des marées terrestres solides (Wang, 1997), car elles seront liées aux résultats obtenus à l'aide de l'INS/GNSS miniature. Je soulignerai la méthodologie des différentes expériences qui ont été faites, les traitements et les corrections appliqués aux données, comme l'INS/GNSS enregistrent des niveaux de bruit élevés, et finalement les résultats de ces données. Pour finir, dans ma conclusion, je discuterai des résultats obtenus et des améliorations nécessaires pour approfondir les possibilités de ce système.

1.2 État de l'art

Au début des années 1970, la première plate-forme stabilisée pour gravimètres a été utilisée pour les essais aéroportés. La première, développée par LaCoste, utilise des gyroscopes pour assurer leur stabilisation sur trois axes. Dans les années suivantes, il n'y aura pas beaucoup de développement pour ces gravimètres aéroportés car le GNSS doit s'améliorer afin d'avoir une meilleure précision sur la position, il sera ensuite utilisée pour obtenir la vitesse et l'accélération avec une meilleure précision. Au lieu d'utiliser un gravimètre sur une plate-forme stabilisée, le gravimètre peut également être sanglé. Un gravimètre aéroporté *strapdown* aura, dans de nombreux cas, l'avantage d'être moins cher, plus facile à installer, plus petit et plus léger. Il n'aura cependant pas la même précision qu'une plate-forme stabilisée et souffrira davantage de la dérive dans le temps.

Au début du 21^{e} siècle, J. H. Kwon et C. Jekeli (J. H. Kwon & C. Jekeli, 2001) ont développé une nouvelle approche pour la gravimétrie aéroportée utilisant INS/GNSS. Leur algorithme utilise les accélérations cinématiques pour mettre à jour les positions ou les vitesses. Tous les calculs sont effectués dans le référentiel inertiel. Ils ont utilisé les données obtenues par l'Université de Calgary qui dispose des données GNSS à des intervalles de 0,5 s et des données brutes des accéléromètres et des gyroscopes à une fréquence de 50 Hz. Quatre vols ont ainsi été effectués au-dessus des montagnes Rocheuses à l'aide d'un Strapdown INS (SINS), ce qui signifie qu'il est attaché au cadre de la plate-forme. L'altitude du terrain dans cette région varie entre 500 et 3000 mètres. La vitesse de vol moyenne était donc de 430 km/h avec un filtre passe-bas de coupure de 120s, cela donne une demi-longueur d'onde de 7 km. Les quatre vols suivent approximativement la même ligne pour tester la répétabilité.

Un système de gravimétrie mobile autonome « Limo-G » (LIght MOving Gravimetry) a été développé (Bertrand de Saint Jean, 2008). Ce système combine 3 accéléromètres "QA 3000-020" et plusieurs antennes GNSS afin de mesurer l'accélération selon 3 axes. Ces accéléromètres avaient déjà été utilisés sur des satellites, des avions ainsi que des missiles. Le système tétraèdre créé était monté sur une camionnette ou un bateau, pour être connecté à un récepteur et à une batterie à l'intérieur du véhicule. Cette étude a également montré la dépendance à la température de ces accéléromètres. De plus, deux accéléromètres du même modèle ont des réponses différentes aux variations de température. Ce système s'avérerait suffisamment précis pour avoir une précision milligale.

En 2008, l'Université nationale de technologie de la défense (NUDT) en Chine a créé le SGA-WZ, le premier système gravimétrique aéroporté chinois développé à partir d'un système SINS/DGNSS (GNSS différentiel). En 2013, une équipe de chercheurs chinois a publié ses résultats en utilisant ce système sur un avion Cessna 208 (Cai et al., 2013). Pendant le vol d'essai, l'avion a suivi les mêmes lignes plusieurs fois au cours de six vols, ce qui leur a permis de tester la répétabilité. La longueur des lignes répétées était de 100 km et l'avion avait une vitesse relativement constante de 216 km/h. En utilisant une période de filtrage de 160 secondes, ils ont obtenu une

résolution spatiale de 4,8 km avec une précision aussi petite que 3,2 mGal pour leurs lignes répétées (avec 1 Gal = 10^{-2} m/s², 1 mGal = 10^{-5} m/s²).

Plus récemment en 2022, Luo et al. décrit l'intégration d'un SGA-WZ04, une version mise à jour du système utilisé dans l'étude mentionnée précédemment. Ils l'ont installé dans un UAV CH-4, un véhicule aérien sans pilote (UAV) développé par la China Academy of Aerospace Aerodynamics avec une envergure de 18 m, une masse maximale au décollage de 1300 kg et volant de 12 à 30 heures selon le poids de la charge utile. Grâce à cette plateforme, cette équipe réalise des tests de gravimétrie pendant plus de 20 heures. Tout comme l'étude mentionnée précédemment, ce drone survolait également les mêmes lignes à plusieurs reprises au cours de plusieurs vols. Avec une vitesse de croisière de 180 km/h pour obtenir une demi-longueur d'onde de 3 km, ils ont utilisé un filtre passe-bas de coupure 120s. Après traitement des données et filtrage, une précision de 0,35 mGal/3 km a été obtenue.

Un système de gravimétrie vectorielle INS/GNSS embarqué sur UAV a été développé (Lin et al., 2018) en utilisant iNAV-RQH, un système de navigation gyroscopique inertiel. Ce système était attaché à un drone quadricoptère. En mode cinématique, ce système avait une précision de 4 mGal.

En 2020, Prasad, A., Middlemiss, R.P., Noack, A. et al. a publié les résultats d'une expérience de 19 jours pour mesurer les marées terrestres avec un gravimètre MEMS. Le gravimètre utilisé se compose d'une plaque de silicium servant de support, d'une plaque centrale MEMS contenant une masse d'épreuve avec des capteurs suspendus par des flexions et d'un troisième panneau de verre équipé de capteurs pour détecter les mouvements de la masse d'épreuve. Ils ont obtenu une corrélation de 97,5 % avec le signal gravitationnel des marées terrestres (à l'aide du logiciel Tsoft).

Dans le passé, les études de gravimétrie mobile ont connu un grand succès et obtenu des données de haute précision, mais la principale différence de mon travail réside dans le fait que je n'utilise pas un gravimètre (uniquement comme outil de

référence) mais un INS/GNSS, qui s'appuie sur la méthode opportuniste d'utilisation des accélérations mesurées par les accéléromètres pour les applications gravimétriques. La deuxième différence est la taille de l'INS, qui est un INS MEMS avec une taille comparable à une clé USB. Cette taille permet de l'installer sur n'importe quel véhicule sans perturber la charge utile. Les instruments mentionnés dans les études précédentes ont des poids allant de dizaines à des centaines de kilogrammes, tandis que le MEMS INS utilisé ne pèse que quelques grammes.

1.1.b Scientific Context

The goal of this thesis was to work with a miniature Inertial Navigation System (INS) associated with a Global Navigation Satellite System (GNSS), defined herein as INS/GNSS, two models of Advanced Navigation are used: SPATIAL and MOTUS (technical characteristic in Annex). I study the viability of using these instruments for gravimetric applications (analysis of variable fields). There exist multiple methods to study the gravity on Earth. A gravimeter is an instrument that is great for local measurements as it will be highly precise (~10^{-9}m/s²), but inefficient to cover a large area as it will be a slow process, which is why gravimeters only cover the short-wavelengths on Earth. Satellites placed in a low Earth orbit are used to continuously study the complete gravity field of Earth, but because of the large distance between the surface of Earth and the satellite, the spatial resolution will be lower, which is why satellites only cover the long wavelengths. Mobile (airborne/UAV/car/boat) gravimetry gave a way to obtain these medium wavelengths. It's important that gravimetry covers the complete spectrum of wavelengths since some physical processes have a spatial scale that cannot be detected by satellite gravimetry (Flechtner et al., 2021) (Fig. 1.1 shows the spatial and temporal resolution of some of these processes that influence the sea level, which in turn changes gravity at sea). Mobile gravimetry consists of placing an instrument that can be used for gravimetry (gravimeter, accelerometers) inside a vehicle in order to move around and measure continuously to cover a bigger area compared to making in situ measurements with a gravimeter, one point at a time, while also staying closer to the surface of the Earth to improve the spatial resolution. However in a moving vehicle, there will be accelerations present (accelerating vehicle, vibrations, ..) that would not

be present (or much lower amplitude) during local or satellite gravimetry where the atmospheric friction forces are very low (Sanchèz et al., 2023). Because of this, the position of the instrument needs to be determined with high precision at every moment, to remove the accelerations that are not related to gravity. When installing the instrument inside the vehicle there are two options. A strapdown system, where the instrument is firmly attached to the body of the vehicle (Ayres-Sampaio et al., 2015 & Skaloud et al., 2016), or a stabilization platform, which will correct the rotations of a vehicle (e.g. inside a plane) and minimize vibrations. With the precision of GNSS increasing, so does the precision of mobile gravimetry.

Many studies have been done for mobile gravimetry, some of which I will mention, but the main difference between these studies and my work is the opportunistic method of using a miniature INS/GNSS (instead of a gravimeter), which is normally used for navigation and the accelerations measured by the accelerometers are used to update and increase the precision of the navigation (Farrell et al., 1998) using a Kalman filter (Becker A., 2023 & Kim et al., 2019). Instead I will be using those accelerations for gravimetry, as gravity after all is an acceleration. The second important part of this work is the size of the instrument that is being used. The idea was to work on a system that would be smaller, cheaper, lighter and could be installed in a much smaller vehicle, for example but not limited to a fixed-wing single rotor drone, which can be deployed quickly and fly over hard-to-reach areas that other vehicles can't reach, while also covering the intermediate wavelengths (10-100 km) that cannot be covered using satellites or gravimeters on the surface (Featherstone, 2003). The ultimate goal of such a system would be the ease of access and use of it in different countries, in order to cover areas quickly and detect the variable gravity anomalies, for example related to the presence of an aquifer in areas that are in dire need of sources of water (Binley et al., 2015 & Inglezakis et al., 2016). (Fig. 1.2 shows the gravity anomalies due to aquifers and the precision required depending on the distance to the source.)

In this thesis, I will give an overview of the history of gravity, the importance of it that led to the development of different Earth models, which in turn, was key for the spatial conquest. That rapid expansion of non-gravity (e.g. SWARM) and gravity (e.g. GOCE, GRACE) satellites then gave a way for global coverage of the static/variable

gravity field of Earth, leading to the creation of the geoid model (Grafarend, 1994), incorporated in the Earth's models to be more precise. The geoid model shows the importance of gravimetry and how gravity anomalies give us information about temporal and spatial variations on Earth (Schwarz et al., 1996 & Ramillien et al., 2021). Some of these variations I will briefly touch upon, like the study of the solid Earth tides (Wang, 1997), as they will relate to the results obtained using the miniature INS/GNSS. I will highlight the methodology of the different experiments that were done, the processing and corrections applied to the data, as INS/GNSS record high noise levels, and ultimately the results of this data. To finish, in my conclusion I will discuss the results obtained and the improvements that are required to further the possibilities of this system.

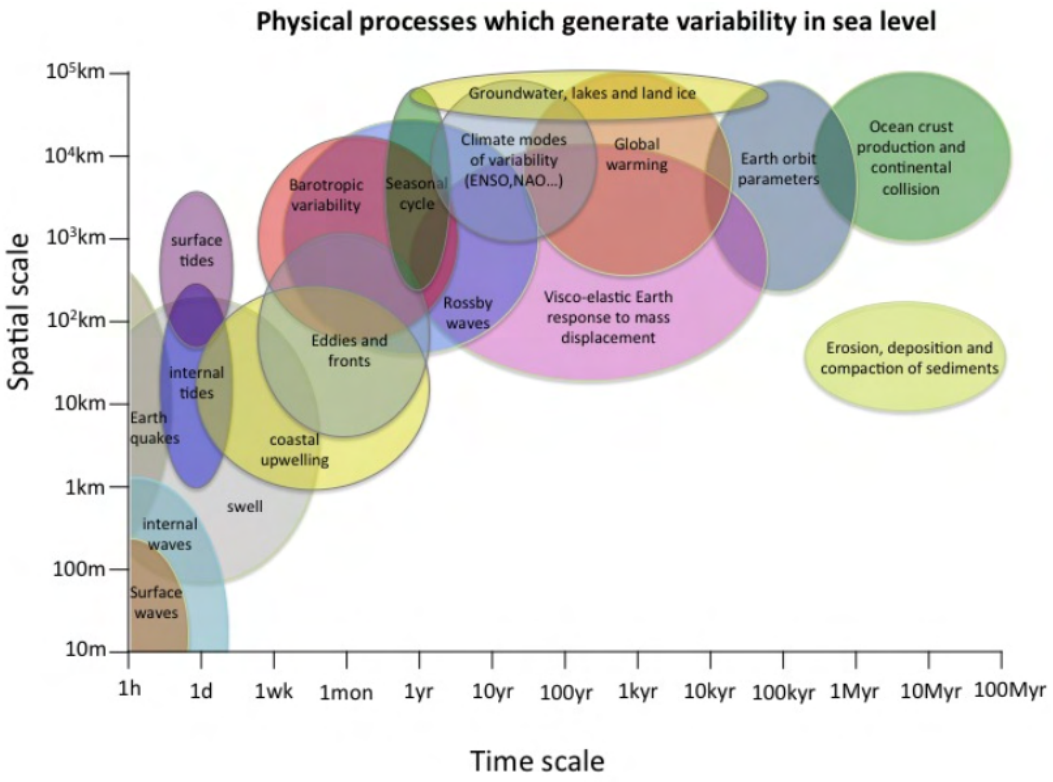

Fig. 1.1 Spatio-temporal scale of the main physical phenomena affecting the ocean surface

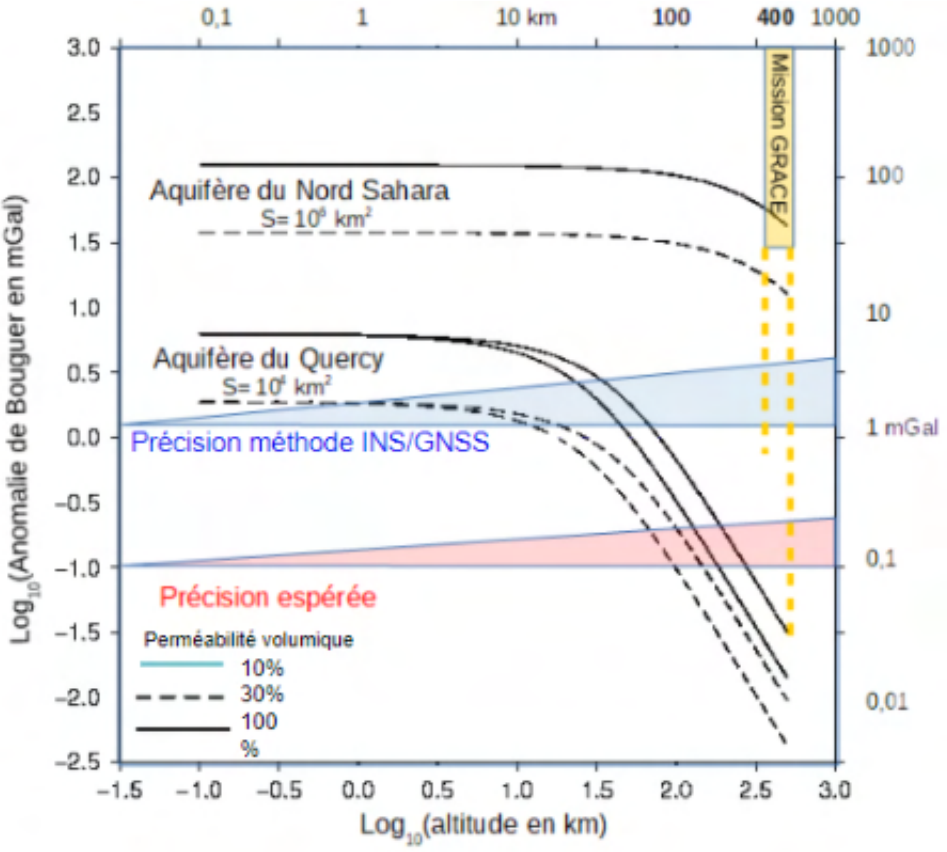

Fig. 1.2 Modeling of the accuracy needed to find anomalies in some groundwater reservoirs as a function of the source/gravimeter distance

1.2.b State of the art

In the early 1970's is when the first stabilized platform for airborne gravimeters was used for airborne testing. The first one was developed by LaCoste and these platforms use gyroscopes to ensure their three axis stabilization. In the following years not much development would happen for these airborne gravimeters because GNSS had to improve with it in order to have a better precision on the position, which would then be used to obtain the velocity and acceleration with a better accuracy. Instead of using a gravimeter on a stabilized platform, the gravimeter can also be strapped down. A strapdown airborne gravimeter will have, in many cases, the advantage of being cheaper, easier to install, smaller and lighter but will not have the same precision as a stabilized platform and will suffer more from drift over time.

At the start of the 21st century, J. H. Kwon and C. Jekeli (J. H. Kwon & C. Jekeli, 2001) developed a new approach for airborne gravimetry using INS/GNSS. Their algorithm uses kinematic accelerations as updates instead of positions or velocities and all calculations are done in the inertial frame for simplification. They used the data obtained by the University of Calgary which has the GNSS data at 0.5s intervals and the raw data from the accelerometers and gyroscopes at a rate of 50Hz. Four flights were done over the Rocky Mountains using a Strapdown INS (SINS), meaning it's attached to the frame of the platform. The terrain elevation in this region ranges between 500 to 3000 meters. The average flight speed was 430 km/h so with a cutoff low-pass filter of 120s this gives a half-wavelength of 7 km. The four flights follow approximately the same line to test the repeatability.

An autonomous mobile gravimetry system "Limo-G" (LIght MOving Gravimetry) was developed (Bertrand de Saint Jean, 2008). This system combined 3 "QA 3000-020" accelerometers and multiple GNSS antennas to measure the accelerometry along 3-axis. These accelerometers had already been used on satellites, planes and even missiles. The tetrahedron system created would be mounted on a van or boat as it also had to be connected to a receptor and battery inside the vehicle. This study also showed the temperature dependency these accelerometers have and that two accelerometers of the same model have different responses to temperature variations. This system would prove precise enough to have a milligal precision.

In 2008, the National University of Defense Technology (NUDT) in China made the SGA-WZ, the first Chinese airborne gravimetry system that is developed from a SINS/DGNSS system (Differential GNSS). In 2013, a team of Chinese researchers published their results using this system on a Cessna 208 plane (Cai et al., 2013). During the test flight the plane followed the same lines multiple times over the course of six flights, this allowed them to test the repeatability. The length of the repeated lines was 100 km and the plane has a relatively consistent speed of 216 km/h. Using a filter period of 160 seconds they obtained a spatial resolution of 4.8 km with a precision as small as 3.2 mGal for their repeated lines (with 1 Gal = 10^{-2}m/s², 1 mGal = 10^{-5}m/s²).

Most recently in 2022, Luo et al. described the integration of a SGA-WZ04, an updated version of the system used in the previously mentioned study, installed in a CH-4 UAV, which is an unmanned aerial vehicle (UAV) developed by the China Academy of Aerospace Aerodynamics with a wingspan of 18 m, a maximum takeoff weight of 1300 kg and can fly 12 to 30 hours depending on the weight of the payload. Using this platform this team carries out gravimetry tests for over 20 hours. Just like the previously mentioned study, this UAV would also fly over the same lines repeatedly over the course of multiple flights. With a cruising speed of 180 km/h to obtain a half-wavelength of 3 km they used a 120s cutoff low-pass filter. After data-processing and filtering an accuracy of 0.35 mGal/3 km was obtained.

An INS/GNSS UAV-borne vectory gravimetry system was developed (Lin et al., 2018) using iNAV-RQH, an inertial gyro navigation system. This system was attached to a quadcopter drone. In kinematic mode this system had a precision of 4 mGal.

In 2020 Prasad, A., Middlemiss, R.P., Noack, A. *et al.* published the results of a 19-day experiment to measure Earth tides with a MEMS gravimeter. The gravimeter they used consists of a silicon plate which serves as a support, a middle MEMS plate that holds a proof mass with sensors that is suspended by flexures and a third glass panel that is equipped with sensors to detect the movements of the proof mass. They obtained a 97.5% correlation with the gravitational signal of Earth tides (obtained using the Tsoft software).

Mobile gravimetry studies in the past have known great success and obtained high precision data, but the main difference my work has is that I don’t use a gravimeter (only as a reference tool) but an INS/GNSS, which relies on the opportunistic method of using the accelerations measured by the accelerometers for gravimetric applications. The second difference is the size of the INS, which is a MEMS INS with a size comparable to a USB flash drive, that can be installed on any vehicle without disturbing the payload. The instruments mentioned in the previous studies would have weights ranging from tens to hundreds of kilograms, while the MEMS INS used would only weigh a few grams.

1.3 History of gravity

“The magnitude of the gravitational force between two masses is proportional to each mass and inversely proportional to the square of their separation/distance” (Newton, 1686). Out of the four known forces of nature (gravity, weak nuclear force, electromagnetism and strong nuclear force) gravity is the weakest one but it is also the most dominant one at the same time. A force that has been extensively researched and has allowed us to study many different aspects of Earth and the universe and yet at the same time we don’t know what gravity is. We’ve developed precise models to predict the behavior of bodies of mass due to gravitational attractions, but we just can’t explain why that attraction is there yet.

Newton’s theory of universal gravitational attraction gave birth to the formula:

$$F = \frac{G M_1 M_2}{r^2} \qquad \textit{(Eq. 1.1)}$$

where the distance r in a Cartesian coordinate system is expressed as:

$$r = [(x - x')^2 + (y - y')^2 + (z - z')^2]^{1/2} \quad \textit{(Eq. 1.2)}$$

This law means the attraction between bodies is proportional to the product of their masses, the force acts along the line that intersects with the center of both bodies and is inversely proportional to the square of the distance between the center of gravity of both bodies. However, it was not Isaac Newton that measured the first value for the gravitational constant, G as the experimental advancements at that time would not allow for an accurate measurement. That honor goes to Henry Cavendish, more than 100 years after Newton’s discovery, who measured a value very close to today’s standard of $6.674310 * 10^{-11} m^3 kg^{-1} s^{-2}$. Thanks to Newton’s law and the value for the gravitational constant we can calculate the acceleration g on Earth:

$$g = \frac{G M_{(Earth)}}{r^2} \qquad \textit{(Eq. 1.3)}$$

Given the mass of Earth is $5.98 * 10^{24} kg$ and the distance between the surface and center of Earth is $6.38 * 10^{6} m$, we obtain the value of $9.8\, m/s^2$. This formula is also used to calculate the gravitational attraction of any mass. For several masses the attraction is an additive superposition of their individual gravitational attractions (Newton (1686); Blakely (1995)). Modern developments in the calculation of the Earth's gravity field take into account the ellipticity of the Earth with the ellipsoid Geodetic Reference System of 1980 (GRS80) of the WSG84 system as reference (see 1.3.2 and 1.3.3).

These scientific advancements at the time would make way for more precise models for the prediction of the motion of planets, moons and stars because of gravity. The prediction of the motion of the moon would in turn allow us to better predict the tides but also the solid Earth tides (Harriet et al, 2023).

Today, land-based gravimetry methods measure gravity with an accuracy in the order of μGals for spring systems, to nm/s² for superconductor systems.

1.3.1 Earth models

By studying gravity we have also been able to develop better models for Earth. In fact it was Isaac Newton that also realized Earth wasn't a perfect sphere and its form would be better described as an ellipsoid. The main reason for this is due to Earth's rotation around its axis, this acceleration, which is strongest at the equator and almost zero at the poles, causes flattening (Chambat et al., 2010). Today the parameters of that ellipsoid GRS80 are described by the standard World Geodetic System 84 (WSG84), which is the reference system today for GPS. The parameters of the reference ellipsoid are so that it coincides best with the Mean Sea Level (MSL).

It was during the second half of the 20th century that the necessity arose to have a global unified system that resulted in the creation of WSG60, 66, 72 and 84. The main two reasons were to have maps of the whole world for different applications like aviation, navigation and geodesy (Heiskanen et al., 1967) and the other reason was the developments in astronautics at the time. These systems were created by a collaboration of scientists from different institutions around the world by surveying

data globally and measuring the distance between different stations. These surveyors also found elevation differences due to local gravity fields. This led to the inclusion of a geoid model in the WSG84. The form of the geoid is described as the form the surface of the ocean takes because of the influence of gravity on Earth. This includes the dynamic effect due to the rotation of Earth but not that of wind and tides. Earth's gravitational field is not constant in time and space. The changes in Earth's shape, rotation and density distribution is responsible for gravity field variations. These gravity anomalies are deviations from the reference model. Gravity residuals are temporal signals after the correction for known variations (Crossley, Hinderer & Riccardi (2013)). In regions with a stronger gravitational pull, a positive gravity anomaly, the sea level will rise and in the regions with a weaker gravitational pull, negative gravity anomaly, the sea level will fall. This means that this is an equipotential surface because every point on this surface experiences the same force of gravity and this force is perpendicular to the surface at each point. The difference in height between the reference ellipsoid, described by the WSG84 parameters, and the geoid is called the geoidal height or geoidal undulation. The main reason for these local variations in gravity is due to density changes of the Earth. The Earth is not made of a homogeneous material, so any change in density will result in a change of mass which in turn creates a gravity anomaly.

The geoid reference included in the WSG84 is the Earth Gravitational Model 2008 (EGM2008) (Koks, 2022). It was an updated model that included new, most importantly that provided by the GRACE (Gravity Recovery And Climate Experiment) satellite mission. This mission consisted of two satellites that were launched in polar orbits. The way these satellites would measure gravity anomalies was by constantly measuring the distance between both spacecraft. When the first one passes a region with a stronger gravitational pull it would accelerate it, which would change the distance to the second one. Once it has passed the region it would decelerate again and the second one would accelerate. From these small variations in distance between both of them the gravity anomalies can be calculated. These satellites would circle around the Earth 15 times each day and would help create a model for Earth's gravity. These satellites were also equipped with accelerometers which measure the total accelerations exerted on the satellites. These accelerometers are necessary to remove the acceleration components that are not due to Earth's gravity anomalies, like drag or solar pressure. This geoid will soon be replaced by the

EGM2020 which is updated from satellite gravity information (i.e. GOCE and Grace missions) (Barnes et al., 2015).

The altitudes recorded by our INS/GNSS instrument are the elevations, also called orthometric height. In general the altitude recorded by the Advanced Navigations instruments is the height referenced to the WSG84 ellipsoid, the ellipsoid height (Fig. 1.3). The geoid height at Toulouse is 49 meters so using the following formula the orthometric height can be calculated.

$H = h - N$, where h is the ellipsoid height and N the geoid height *(Eq. 1.4)*

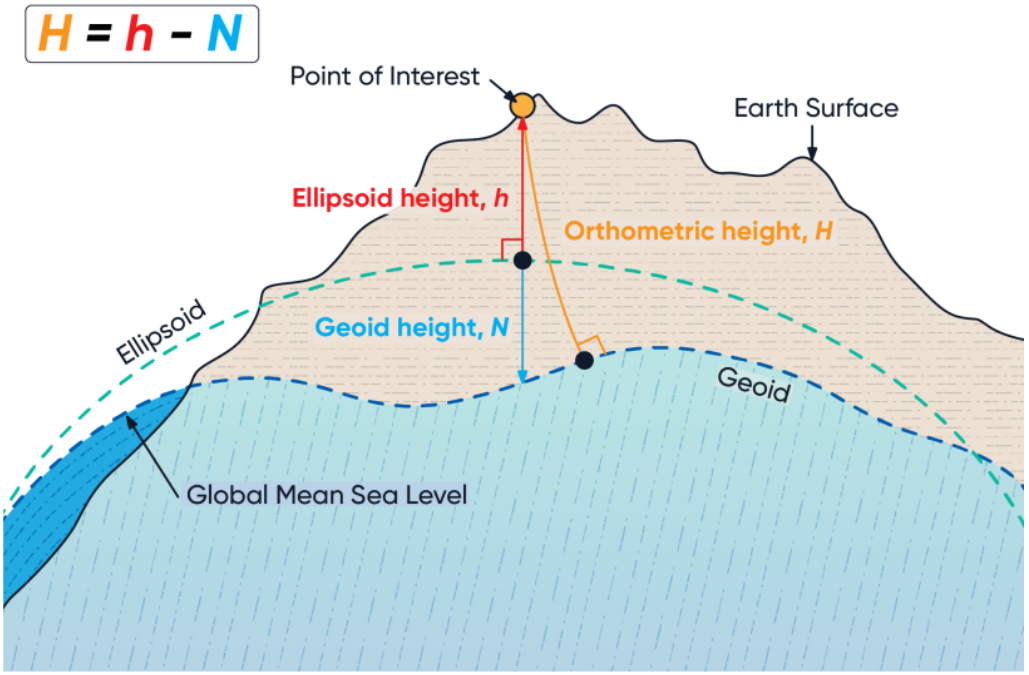

Fig 1.3. Visual representation of the Mean Sea Level (MSL), ellipsoid and geoid (image credit: Advanced Navigations)

1.3.2 International gravity formula

Over time more precise formulas were created to calculate the theoretical gravity depending on the latitude on Earth. The first one in 1930 by the International Association of Geodesy under the following form (Tscherning, 1984):

$g(\varphi) = g_e[1 + A\sin^2(\varphi) + B\sin^2(2\varphi)]$, where g_e the measured gravity at the equator ($\varphi=0°$)

(*Eq. 1.5)*

using the parameters from the Geodetic Reference System of 1980 (GRS80) this formula would be

$$g(\varphi) = 9.780327\,[1 + 0.0053024\,\sin^2(\varphi) - 0.0000058\,\sin^2(2\varphi)] \quad (m/s^2) \qquad (Eq.\ 1.6)$$

The modern formula for theoretical gravity is the Somigliana equation:

$$g(\varphi) = \frac{1 + k\sin^2(\varphi)}{\sqrt{1-e^2\sin^2(\varphi)}}, \qquad (Eq.\ 1.7)$$

with $k = \frac{bg_p - ag_e}{ag_e}$ and g_p, g_e the gravity at the pole and equator

a, b the semi-axes at the equator and polar and e the eccentricity

Using the parameters of the WGS84, where g_p = 9.83218493786340046183 (m/s²), a = 6378137.0 (m), b = 6356752.31424517949756 (m):

$$g(\varphi) = 9.780325335903891718546\,[\frac{1+0.00193185265245827352087\,\sin^2(\varphi)}{\sqrt{1-0.00669437999014131699613\,\sin^2(\varphi)}}] \qquad (Eq\ .\ 1.8)$$

This International Gravity Formula (IGF) gives us the variation of g for different latitudes but calculated on the surface of the reference ellipsoid, the ellipsoid that best fits with the Mean Sea Level (Lambert, 1945).

The reason why the latitude on Earth influences the theoretical gravity is due to Earth's rotation. During its rotation around its polar axis, Earth's mass at the equator is 'pushed' outwards which causes a flattening and why the Earth isn't a perfect sphere but an ellipsoid. This means the semi-axis at the equator (a) is bigger than the semi-axis at the pole (b). Looking at the previously mentioned values for these semi-axes, that difference is approximately 21 km and looking at Newton's law we know an increase in radius means a decrease in the gravitational acceleration. Using the above formula (Eq .3) we can see that this difference is approximately 0.05 m/s².

Part of the measured gravity at the equator is also due to the Earth's rotation. The major component of the gravitational acceleration is due to the Earth's gravitational pull, but a small component will come from its rotation. The closer to the poles, the smaller this component becomes, until it reaches zero at the poles.

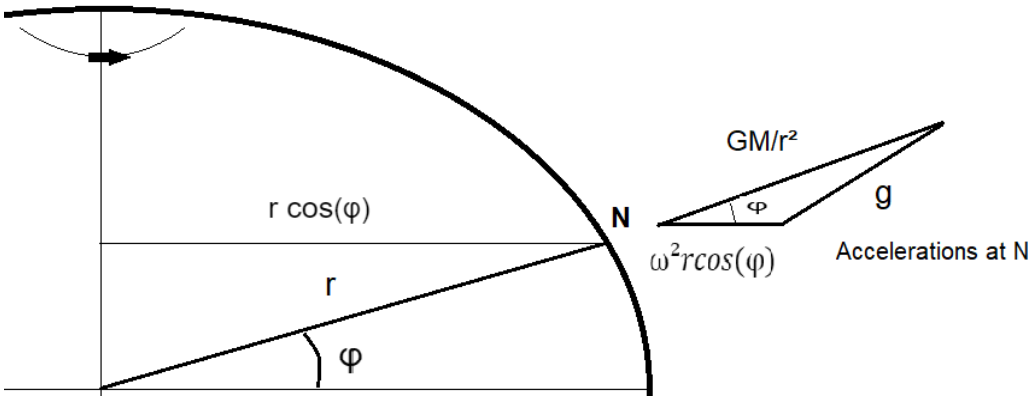

Fig. 1.4 Component of gravity associated to Earth's rotation and latitude

At a point N with latitude φ on the reference ellipsoid, the centripetal acceleration will be $\omega^2 r cos(\varphi)$ (Fig. 1.4). The radial part of this acceleration will be $\omega^2 r cos^2(\varphi)$. The radial velocity ω, with the Earth's rotation being 24 hours is:

$$\omega = \frac{2\pi}{24*60*60} = 7.292124 * 10^{-5} \text{ (rad/s)} \quad \textit{(Eq. 1.9)}$$

so at the equator ($\varphi = 0°$) , $\omega^2 r cos^2(\varphi)$ = 0.033916 m/s². This does not change the gravitational acceleration of the Earth, since that's only dependent on its mass and the radius, this reduces the observed gravitational acceleration.

1.3.3 Free-air and Bouguer correction

Using the IGF another correction that needs to be applied is the free-air correction, which accounts for the elevation which affects the gravity measurements. From Newton's law we know the distance to the center of the Earth changes the gravitational attraction by a factor of $\frac{1}{r^2}$. When measuring gravity at an elevation, for example in a plane, if we want to know the gravity at the point on Earth below the plane, we need to correct for the added distance between the plane and the center

of the Earth. This free-air correction is $0.3085\ \frac{mGal}{m}$ for latitudes of 45° and is calculated as followed:

$$g = \frac{GM}{R^2},\ \frac{dg}{dR} = \frac{-2GM}{R^3} = \frac{-2g}{R}$$, where R is Earth's radius *(Eq. 1.10)*

The WELMEC formula (Swhartz and Lindau, 2002) takes the IGF and adds this height dependency.

$$g(\varphi) = 9.780327\ [1 + 0.0053024\ \sin^2(\varphi) - 0.0000058\ \sin^2(2\varphi)] - 3.085 * 10^{-6} * h$$

(Eq. 1.11)

This formula with these parameters is mainly used for European latitudes (45°), because the free-air correction changes with latitude.

Another correction is the Bouguer correction, which is a correction for the height (free-air correction) and the difference in attraction due to the terrain. In an area that is mostly flat (small undulations permitted) there is no need for a topographic correction, which requires a digital terrain model (DTM) to calculate. The Bouguer correction is used when measuring the gravity in an area that has layers with different densities. It assumes each layer is horizontal, has a constant density and that their distance extends well beyond their thickness. The Bouguer correction formula is

$$g_b = 2\pi\rho G h$$ *(Eq. 1.12)*

with ρ the density of the layer and h its thickness (Karl, 1971).

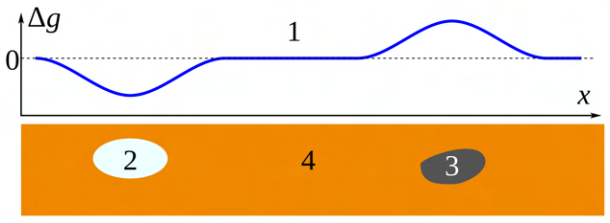

Fig. 1.5 Impact of mass redistribution in the Earth's interior on variations in gravitational acceleration

In Fig. 1.5, the body (2) has a lower density than the crust (4) and the body (3) has a higher density. The gravity measured on the surface at (2) will be lower than at (4), and higher at (3) which has a positive contrast due to the higher density.

The topography correction (g_t) takes into account the deviations from the horizontal layer considered in the Bouguer correction. Terrain that is above the observation point decreases the gravitational effect, similarly the absence of terrain, when it was considered infinitely extended, will also decrease the gravitational effect. The complete Bouguer *(cb)* can be described as: (Blakely, 1995)

$$g_{cb} = g_{obs} - g_b - g_t - g_{fa} - g_0 \qquad \textit{(Eq. 1.13)}$$

1.4 Satellite gravimetry

If Earth were a perfect homogeneous sphere every satellite, given its original launch orbit and speed, would always describe the same circular or ellipsoidal orbit. Earth not being a perfect sphere and not having a homogenous mass distribution this is not the case. Every temporal or spatial change in Earth's gravity field will have an, albeit small, effect on the orbit of a satellite. Spatial variations of the gravity correspond to density changes in the crust, the flattening of the Earth or the presence and absence of structures like mountains or canyons. Temporal variations would for example be redistribution of water mass from hydrology.

The small changes in satellite orbits due to variations in the gravity field is used to resolve the inverse problem to calculate the gravity anomalies on Earth and what is responsible for them.

From Newton's law we know that the effect of gravity reduces with a factor of $1/r^2$ so for a better spatial resolution, the closer the satellite orbits around Earth, the higher its sensitivity to gravitational changes (Fig. 1.2). On the other hand if the orbit is too close to Earth the satellite will be subject to high atmospheric drag, causing degradation of the satellite, deceleration and vibrations. For satellite missions that want to study Earth's gravity field from space, i.e. GOCE for the static field (van der Meijde et al., 2015) and GRACE (Ray et al., 2003 & Chen et al., 2022) for the variable one, having vibrations and deceleration is a big problem because it will add noise to the gravitational signal. For this reason all satellite missions for spatial

gravimetry are placed in a low Earth orbit (LEO) at an altitude between 400 and 500 km.

In 1992 the satellite TOPEX/Poseidon was launched (Fu et al, 1994), its goals included measuring the tides, the ocean sea levels and the temperature of the oceans and how heat is transferred because of the currents (Andersen, 1995). Satellites for altimetry are equipped with a radar, sending an electromagnetic signal to the surface of the ocean and measuring the time to travel back the rippling of the ocean can be calculated. Ground stations, using laser reflectors, radar and the Doppler signal, are able to determine the orbit of satellites with high precision in regards to the reference ellipsoid (Patton, 1960). Subtracting the height measured of the ocean and the altitude of the satellite to the reference altitude, the rippling of the marine geoid is mapped. This in turn allowed the gravity field of the ocean to be determined with high precision. The TOPEX/Poseidon mission was a major breakthrough because it greatly improved the spatial resolution for gravimetry of the oceans. However this method is not able to determine the gravity field at the surface of the continents as it was not designed to.

The first satellite launched for gravimetry was CHAMP (CHAllenging Minisatellite Payload) in 2000 (Reigber et al., 2002), some of its other goals included the study of Earth's magnetic field and the ionosphere and atmosphere. The orbit of this satellite was determined with high precision thanks to GNSS satellites and by analyzing the small changes in its orbit, Earth's gravity field could be mapped. Part of the payload also included multiple accelerometers to determine the small perturbations of the satellite's acceleration along three axes, which can be due to atmospheric drag or radiation pressure from the Sun. This observation principle is called Satellite-to-satellite tracking in the high-low mode (SST-HL) (Fig. 1.6) (Godah et al., 2019), because the GNSS satellites used to determine its position are at a higher altitude (>20000 km) than the CHAMP satellite which is in a low Earth orbit (450 km).

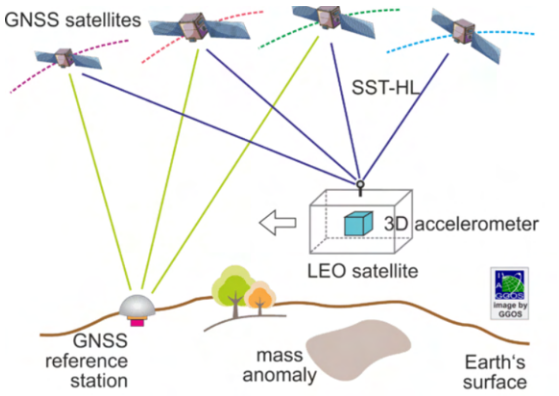

Fig. 1.6 Visualization of SST-HL principle (image credit: GGOS, Laura Sanchez)

The second observation principle is SST-LL, or satellite-to-satellite in the low-low mode (Fig. 1.7) (Rummel, 2019 & Shen et al., 2005). The satellite mission GRACE (Gravity Recovery And Climate Experiment), launched in 2002 and the second mission launched for global gravimetry, used the SST-LL principle. Two (almost) identical satellites are placed in the same low Earth orbit, separated by a few hundred kilometers, and their distance to one another are continuously measured. When the first satellite approaches a positive gravity anomaly, for example a mountainous region, it will accelerate forward, increasing its acceleration and the distance to the second satellite. When it has passed the anomaly it will decelerate again and in turn the second satellite will accelerate and reduce the distance between both satellites (Fig. 1.8). Non-gravitational accelerations are also corrected thanks to the presence of accelerometers along the three axes. Using the changes in distance between both satellites and variations in acceleration, the gravity anomalies of Earth's gravity field can be mapped. The GRACE mission ended in 2017 and in 2018 the mission GRACE-FO (GRACE Follow-Up) was launched. There is a data gap between 2017-2018 that some authors have filled using GNSS measurements from other satellites like the Swarm constellation (Teixeira et al., 2020)

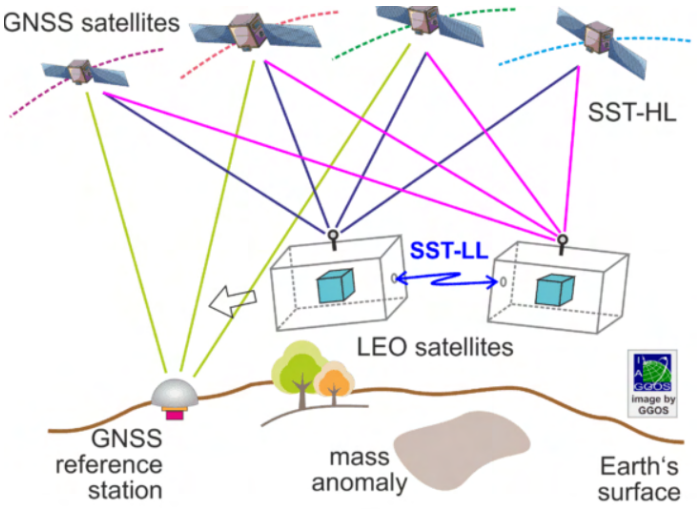

Fig. 1.7 Visualization of SST-LL principle (image credit: GGOS, Laura Sanchez)

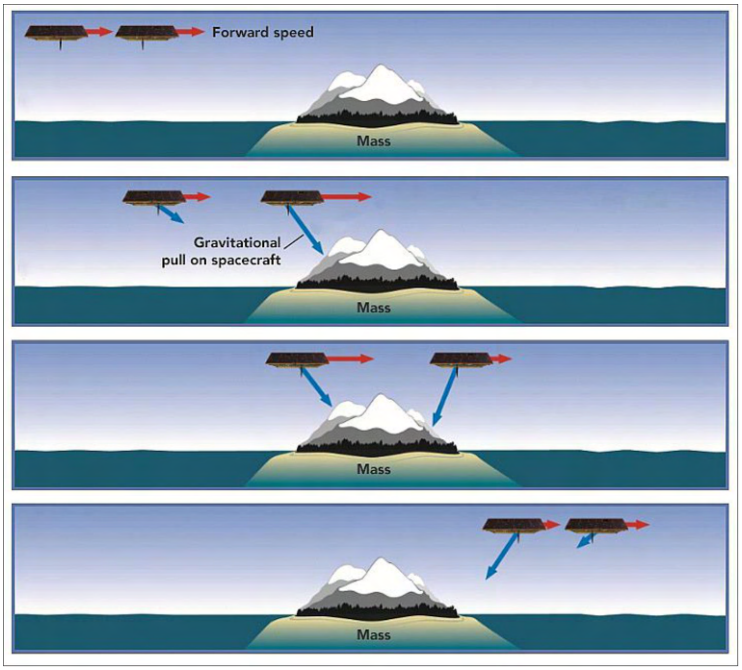

Fig.1.8 Representation of what would happen if the GRACE satellites pass over a mountainous region. (image credit: NASA, Earth Observatory)

The third observation principle for satellite gravimetry is Satellite Gravity Gradiometry, which studies the variations of Earth's gravity field through measurements of the spatial gradient of gravitational acceleration with the help of accelerometers on board the satellite, (SGG) (Koop, 1993) (Fig. 1.9) used for the GOCE (Gravity field and steady-state Ocean Circulation Explorer) mission. This type of observation measures the acceleration variations directly instead of measuring the effect it has and solving the inverse problem. The GOCE satellite had 6

accelerometers (3 pairs of accelerometers), equipped along the three axes and with the pairs separated in order to have one on each side. This way the non-gravitational accelerations could be removed by differentiation because any non-gravitational acceleration would be sensed by all accelerometers and the gravitational accelerations would be slightly different because of the distance separating the pairs. The GOCE satellite was made to orbit at a lower altitude (~250 km) than any other gravimetry mission and the GNSS constellation would also be used for orbit determination. For the mission to succeed at this altitude, as there would be a high increase in atmospheric drag (Jastrow et al., 1957), the satellite had an aerodynamic shape and had an ion propulsion that would accelerate the satellite to counteract the deceleration due to the drag, using a closed-loop system, so that the accelerations measured would not include that caused by the atmospheric drag. The advantage of an electric ion propulsion (Bassner et al., 2000) is also that it would not cause vibrations that add noise to the data of the accelerometers. The duration of the mission would directly depend on the remaining xenon fuel because when the satellite runs out of fuel, it can no longer counteract the deceleration of the drag and would slow down, decreasing the orbit altitude until it made reentry on Earth.

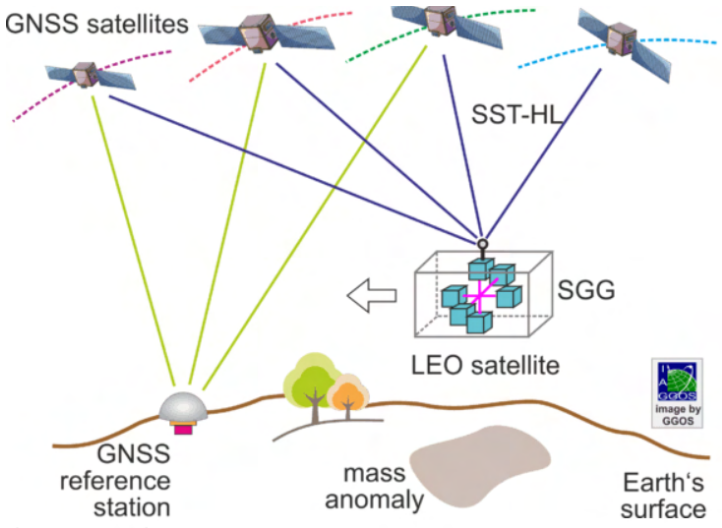

Fig. 1.9 Visualization of SGG principle (image credit: GGOS, Laura Sanchez)

Knowing the gravitational anomalies at the surface of Earth gives us a lot of information about the distribution of masses inside the Earth (static fields on human time scale) but also the fluid envelopes (variable fields on daily, seasonal or annual scales). As explained before the ocean level will rise or fall depending on the gravitational pull below it but also above it.

1.4.1 Bathymetry using gravity anomalies from satellite gravimetry

The gravitational pull below the ocean surface allows for the creation of models that calculate underwater topography such as the height and form of seamounts, underwater mountains or the depth of oceanic trenches. This has been an important step in bathymetry (McKenzie et al., 1976, Smith et al., 1997), the study of underwater depth. At first the depth of the ocean floor was calculated using sonar. An echo sounder, which emits sound pulses, is attached to a boat that sends a signal towards the ocean floor, knowing the speed of the signal traveling through water, the depth can be calculated depending on the time it took for the signal to bounce back. However this method would only give one line of data during the boat's trip. For this reason today multiple echosounders would be attached next to each other, this way a larger area could be covered during a trip. However this method would still be very slow if we'd want to cover the entire ocean floor. Using the data from satellites like Topex/Poseidon and the Jason-1,-2 & -3, which measure the ocean level with high precision, we can look at the differences in sea level to create models of the ocean floor much quicker and cover a much larger area. In 2022, L. Seoane et al. presented the effectiveness of using only data from satellite altimetry. This method, using an extended Kalman filter, was applied to the real case of the topography around the Great Meteor seamount (Atlantic Ocean) and shows an RMS similar to that using single beam depth observations. This approach can be used to gather knowledge of seafloor topography in regions where no echo-sounder measurements have been made.

1.5 Temporal variations of Earth's gravity field

The redistribution of mass on Earth's surface happens through physical processes such as atmospheric depressions, storms, soil moisture and free water (sea, ocean, rivers, lakes, flooded areas) or groundwater. In this case we can consider these redistributions to be rapid spatial and temporal variations of the gravity field.

However there are temporal variations that change the redistribution of mass on Earth, which in turn change its gravity field, these can be categorized by their frequency, periodicity, erraticism and origin (Crossley et al., 2013).

1.5.1 Ocean and Solid Earth tides

The biggest influence on Earth's gravity field at the surface level that is time-variable will be that caused by the tides. The gravitational attraction of celestial bodies, most prominently the Moon and to a lesser extent the Sun, will cause the water in the oceans to be displaced (Cartwright, 1977). Because of the motion of Earth and other celestial bodies, the influence of their gravitational field will vary and their periodicity will be reflected by the ocean's tides. The ocean tides allow us to observe this gravitational pull easily but it isn't just the water of the ocean that is affected, but Earth in its totality. The solid crust of Earth is also deformed but this is less noticeable because of its rigidity, nonetheless the highest signal amplitude from solid Earth tides can reach over 3 μm/s².

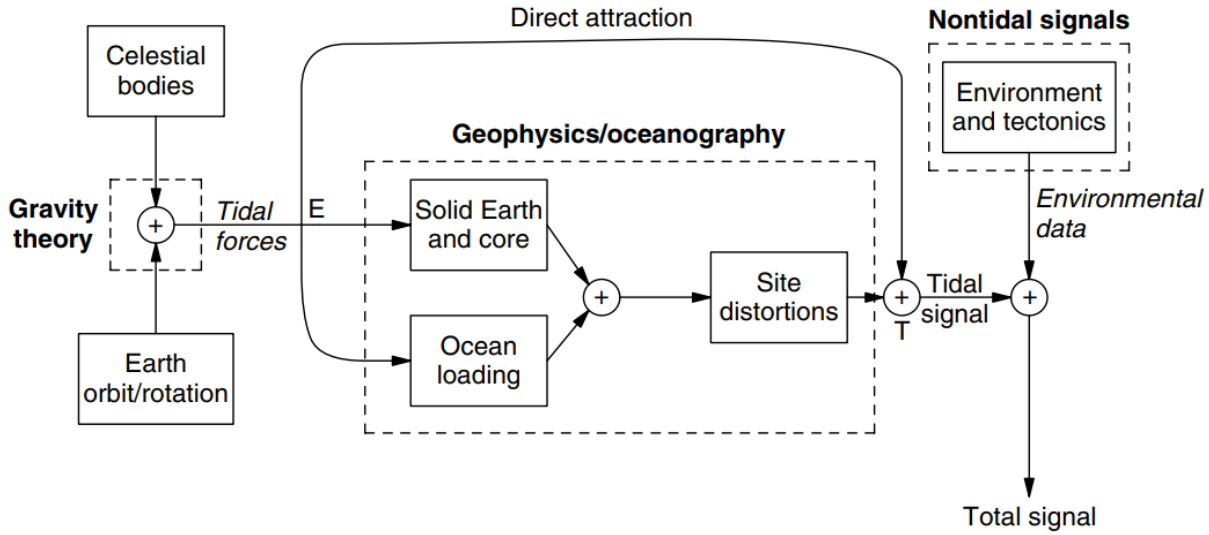

Fig. 1.10 Tidal flowchart. Italics; things we know to very high accuracy, bold; (over the dashed boxes) represent things we can learn about using tidal data (Agnew, 2015)

Figure 1.10 explains what makes up the tidal signal. Firstly the box *Tidal Forces* are the forces that are obtained from theoretical models due to the movement of the celestial bodies and the rotation of Earth. The effect of these forces is calculated on

an oceanless Earth to obtain the solid Earth tides at a location E. Using an ocean model the effect on the ocean tides is calculated, but also the effect of the displacement of water mass on Earth which causes a deformation of Earth, called ocean tides loading. Together these tides give the total tidal signal. (Agnew, 2015)

1.5.2 Effect of polar motion on centrifugal acceleration

Because Earth isn't a perfect sphere, when it is rotating there will be small deviations from the theoretical axis of rotation. This deviation, discovered by Seth Carlo Chandler, is called the Chandler Wobble and has a period of approximately 435 days. On top of that there is also an annual oscillation of the polar axis. These two components together are responsible for the polar motion of Earth. With the presence of a centrifugal acceleration on Earth due to its rotation (strongest at the equator, weakest at the poles), these changes in the polar motion will cause a change in the centrifugal acceleration at different latitudes.

The aforementioned phenomena are periodic and can be predicted with different models. However there are also non-periodic phenomena that influence Earth's gravity field.

1.5.3 Pressure of the atmosphere

Deviations of the nominal pressure value (101,325 Pa) in regional atmospheric pressure increase the load on the ocean or land below. This change in load can cause surface deformation, but this deformation will depend on the region and its corresponding admittance factor.

$$P_{nom} = 1013.25 * (1 - \frac{0.0065h}{288.15})^{5.2559} \quad \textit{(Eq. 1.14)}$$

$$\delta g_{atmos} = \alpha * (P(t) - P_{nom}) \quad \textit{(Eq. 1.15)}$$

(Crossley et al, 2002)

1.5.4 Hydrologic temporal variations

Changes in rainfall, the amount of water stored in the ground, moisture, etc. are also non-periodic variations that influence the gravity field at the surface. Some changes in hydrology are linked to the seasons and seasonal variations in gravity have been linked to hydrology mass changes (Vörösmartyet al., 2005 & Marshall, 2014) that happen during those periods using superconducting gravimeters (Amalvict et al., 2004). The effect on gravity is calculated using the following equation (Eq. 1.16), with ϕ is the porosity of the soil (value ranging between 0-100%). This equation also considers a horizontal plate that extends far enough where the distance causes the gravitational effect to become negligible (Bouguer Slab).

$$\delta g = 2\pi G \phi h \rho_{water} \qquad \textit{(Eq. 1.16)}$$

For 1 m of water on top of the surface, not in the soil (ϕ = 1), δg = 0.419 µm/s² or 41.9 µGal.

1.6 Mobile gravimetry

The intermediate spatial resolution for wavelengths from tens kilometers to some hundred kilometers do not have good coverage from terrestrial and space-borne gravimetry. Mobile gravimetry tries to fill the gaps in this spectrum in order to provide a complete view of Earth's gravity field. Mobile gravimetry is the study of gravimetry on a moving terrestrial vehicle like a car, a boat, a plane, a UA,... (Verdun et al., 2022). With airborne gravimetry being the study of gravimetry in the air using for example a multi-rotor drone, a fixed wing rotor, a plane, a helicopter,... (Gerlach et al., 2004).

A gravimeter or accelerometer alone in a moving vehicle is not able to measure Earth's gravity because it measures the specific force at any given time, this includes any acceleration that is proper to the vehicle on which it is mounted. In order to be able to calculate the gravity, another system like GNSS is required to measure the accelerations that are due to the moving vehicle so that they can be removed from the specific force recorded by the accelerometers.

The principal airborne vector gravimetry equation (Eq. 1.17) is based on Newton's second law of motion for a non-rotating coordinate frame in free-fall. This inertial frame (i-frame) can have the Earth's core as its origin.

$$\ddot{\mathrm{x}}^{i} = a^{i} + g^{i} \qquad \textit{(Eq. 1.17)}$$

with $\ddot{\mathrm{x}}^{i}$ the second time derivative of positions, obtained from GPS, a^{i} the specific force, obtained from the INS/GNSS accelerometers and g^{i} the gravitation. The specific forces are the non-gravitational forces per unit of mass acting on a body, meaning it's not an actual force but an acceleration. An accelerometer measures the specific forces acting on it, which are the acceleration relative to free-fall, mechanical effects due to the vehicle etc. An accelerometer being only in free-fall will record a specific force of 0 m/s² as no other acceleration besides that of gravity is acting on it. An accelerometer at rest on the ground will record a specific force of ~9.8 m/s² which is the ground exerting a force on it (+9.8 m/s² if the z-axis is pointing in the UP direction in the ENU-frame, -9.8 m/s² if its z-axis is pointing in the DOWN direction in the NED-frame), which is the ground exerting a force on it). Unlike what its name implies, the specific force is not a force (kg*m/s²) but an acceleration (m/s²).

The history of airborne gravimetry started as early as 1958, when the first Lacoste-Romberg Model "S" Air-Sea gravimeter was fixed on the inside of a jet tanker and the first helicopter airborne gravimetry happened in 1965.

I have mentioned the main difference of my work with those of the studies mentioned in 1.2, is the INS/GNSS instrument and the smaller lightweight drone used. With the basics of gravimetry and different concepts explained, I will describe the material that I used myself in the next chapter.

CHAPTER 2 Material and methodology

In this chapter I will go over the strategy to accomplish my research. This chapter serves as an overview of both the material and the methods that I used during my experiments, which will be presented later.

2.1 Material

2.1.1 Spatial INS/GNSS

To provide a solution for hard-to-reach regions while also being a cheaper and faster solution, I worked on a system using a much smaller INS/GNSS system, with the size and weight comparable to that of a USB flash drive (Fig. 2.1 & 2.3). Because of its size and weight it can easily be installed on lighter vehicles like a fixed wing rotor drone (Fig. 2.2), without disturbing the rest of the payload. The ultimate goal, with sufficient enough precision, is that this system could quickly be deployed over a hard-to-reach region where we want to study its gravimetric properties, with for example an important application being the search of gravimetric anomalies that indicate the presence of a possible aquifer (Cooke A.-K., 2020).

The INS/GNSS used is the SPATIAL model developed by Advanced Navigation. This model features Advanced Navigation's AI navigation algorithm. This neural network sensor fusion algorithm provides an accuracy of up to 10 times that of a traditional Kalman filter.

Table 1.1 is a condensed overview of the SPATIAL specifications.

Parameter	Value
Horizontal Position Accuracy (with L1 RTK)	0.02
Vertical Position Accuracy (with L1 RTK)	0.03 m
Velocity Accuracy	0.05 m/s
Roll and Pitch Accuracy (Dynamic)	0.2 °
Heading Accuracy (Dynamic with GNSS)	0.2 °

Parameter	Accelerometers	Gyroscopes
Bias Instability	$20\mu g$	3 °/hr
Initial Bias	< 5 mg	< 0.2 °/s
Scale Factor Stability	< 0.06 %	$< 0.05\%$
Noise Density	100 $\mu g/\sqrt{Hz}$	0.004 °/s/$\sqrt{Hz}$

Table 1.1 - GNSS, accelerometer and gyroscope specifications of SPATIAL

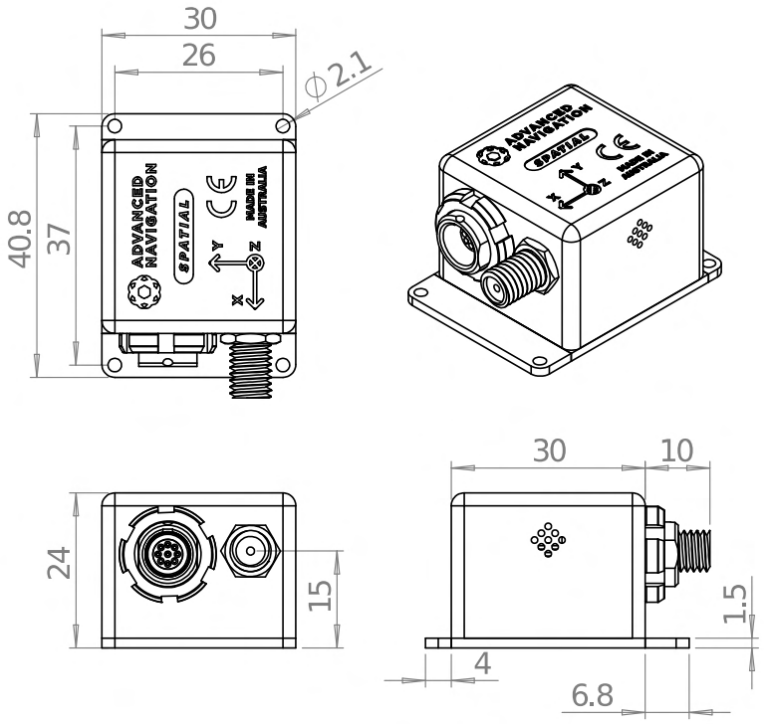

Fig. 2.1 Mechanical drawing of the SPATIAL INS/GNSS (units: mm, image credit: Advanced Navigation)

Fig. 2.2 The Boreal LAB drone (fixed-wing rotor drone)

Fig 2.3. MEMS INS/GNSS model SPATIAL next to a USB flash drive

2.1.2 Relative gravimeter

The gravimeters used in the previously mentioned studies use a spring to measure gravity. The spring counteracts the force of gravity that is applied to an object. Knowing the properties of the object, also named the proof mass and that of the spring, the change in length of the spring is used to determine the changes in gravity. This proof mass is enclosed in a vacuum chamber so that external factors like wind, pressure changes don't influence the measurement of gravity.

Most of the modern gravimeters, and the CG5 gravimeter that I used (Fig. 2.4) as a reference for some experiments, use quartz based zero-length springs. The reason these types of springs are used is because their oscillation is very long, meaning that vibrations or noise from the mechanical components of the gravimeter, won't have an effect on the measurements

Fig. 2.4 CG-5 Gravimeter (Scintrex)

These types of gravimeters are called relative gravimeters (Timmen, 2010) because the value given by the instrument depends on its calibration. Usually they are

calibrated at a location where the absolute value of gravity is known with high precision (using for example the IGN database for reference points) and afterwards transporting the gravimeter to a location where the value of gravity is unknown to measure the difference. Relative gravimeters do have an inherent drift over time and thermal drift (Francis, 2021). By recording data over a long period of time (multiple hours or days) this drift must be quantified and corrected (Fores et al., 2017). However time-dependent gravity changes, for example those caused by Earth tides, need to be accounted for so that they are not included in the drift correction.
An absolute gravimeter measures the time it takes for a proof mass to fall in a vacuum chamber, the acceleration is measured using atomic clocks and laser interferometers (Niebauer, 2007). These types of gravimeters aren't practical to be used in the field as they are much larger than relative gravimeters and are used to calibrate the relative gravimeters or used in monitoring stations.

In recent years MEMS gravimeters have been developed and used for the measurement of solid Earth tides (Middlemiss et al., 2016), which removes the limiting weight factor of commercial gravimeters like the CG5. MEMS stands for micro-electromechanical systems. This technology uses microscopic devices, which use components whose size range from 1 to 100 micrometers.

The SPATIAL model I used is a MEMS INS. Meaning the sensors that make up this INS are microscopic devices which is why its size is so small even though it has so many components included.

I'll go over the important components which data I used that are in an INS and the difference between an IMU, AHRS, INS and how they differ from gravimeters.

2.1.3 ACCELEROMETER

An accelerometer measures the proper acceleration applied to it in its own instantaneous rest frame. Important to note that accelerometers will interpret the accelerations according to the definition used in general relativity and not that of

Newtonian gravity. This means that an accelerometer at rest with its z-axis pointing upwards will measure a value of 1g and in free-fall it will read a value of 0g.

Most modern accelerometers are also MEMS. A MEMS accelerometer is essentially a mass suspended by a spring, as shown in Fig. 2.5. The mass is called the proof mass and the direction in which the mass can move is called the sensitivity axis. When an accelerometer is subjected to a linear acceleration along the sensitivity axis, the acceleration causes the proof mass to move to one side, the amount of deflection being proportional to the acceleration (Albarbar et al., 2009).

Using piezoresistors in the beams, the acceleration which causes the deformation will in turn cause a change in the electrical resistivity of the resistors. This difference in resistivity is then used to calculate the acceleration that caused it. By mounting 3 accelerometers perpendicularly to one another the acceleration can be measured along three axes for an object moving in 3 dimensional space. Accelerometers used for gravimetry purposes are known to come with a lot of noise and signals that are of no interest for gravimetry studies but are due to the high sensitivity of the accelerometers to various other phenomena than gravity like vehicle acceleration, vibration of mechanical engine parts, etc. It's also evident that the trade-off to have smaller instruments is more noise and precision taking a hit. Accelerometers also come with strong temperature bias.

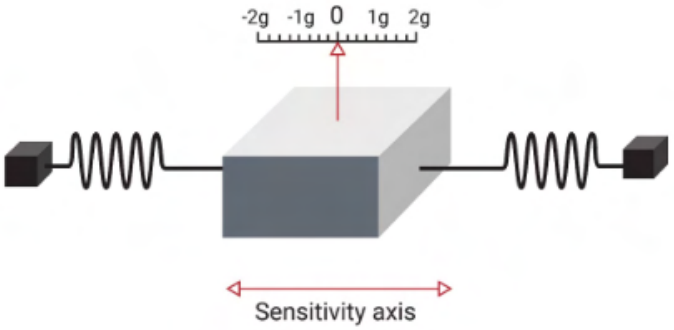

Fig. 2.5 Visualization of the working of a MEMS accelerometer (one single direction)

2.1.4 GYROSCOPES

A gyroscope is an inertial sensor that measures the angular velocity of an object relative to an inertial reference frame. MEMS gyroscopes measure angular velocity

by applying the theory of the Coriolis effect, which refers to the inertial force acting on moving objects relative to the inertial reference frame (Din et al., 2021). To better understand this, consider a mass suspended from springs, as shown in Fig. 2.6. This mass is subjected to a driving force on the x-axis which causes it to oscillate rapidly on this axis. While it is in motion, an angular velocity, ω, is applied about the z-axis. The mass then experiences a force in the y-axis due to the Coriolis force, and the resulting displacement is measured by a capacitive sensor. The position of the mass, *m*, in the inertial frame is given by:

$$^{B}\boldsymbol{r} = \begin{bmatrix} x \\ y \end{bmatrix} \quad \text{(Eq. 2.1)}$$

The inertial velocity of the mass in the body frame is then defined as the derivative of the position plus the tangential velocity due to rotation:

$$^{B}\dot{\boldsymbol{r}} = \begin{bmatrix} \dot{x} \\ \dot{y} \end{bmatrix} + {}^{B}\boldsymbol{\omega} \times {}^{B}\boldsymbol{r} = \begin{bmatrix} \dot{x} - \omega y \\ \dot{y} + \omega x \end{bmatrix} \quad \text{(Eq. 2.2)}$$

The inertial acceleration of the mass in the frame is the derivative of the velocity plus the tangential acceleration due to rotation:

$$^{B}\ddot{\boldsymbol{r}} = \begin{bmatrix} \ddot{x} - \omega\dot{y} \\ \ddot{y} + \omega\dot{x} \end{bmatrix} + {}^{B}\boldsymbol{\omega} \times {}^{B}\dot{\boldsymbol{r}} = \begin{bmatrix} \ddot{x} - 2\omega\dot{y} - \omega^2 x \\ \ddot{y} + 2\omega\dot{x} - \omega^2 y \end{bmatrix} \quad \text{(Eq. 2.3)}$$

The first term of the previous equation (Eq. 2.3) represents the acceleration experienced by the driven axis, which is actively controlled by the gyroscope electronics. The second term represents the acceleration of the gyroscope sensing axis. According to Newton's second law of motion, the sum of the forces in the sensing direction is equal to the product of the mass of the block, *m*, and the acceleration in the sensing direction.

In the past few years the market for MEMS gyroscopes has grown a lot thanks to their small size, low price and use in many devices, for example smartphones, game controllers and VR headsets.

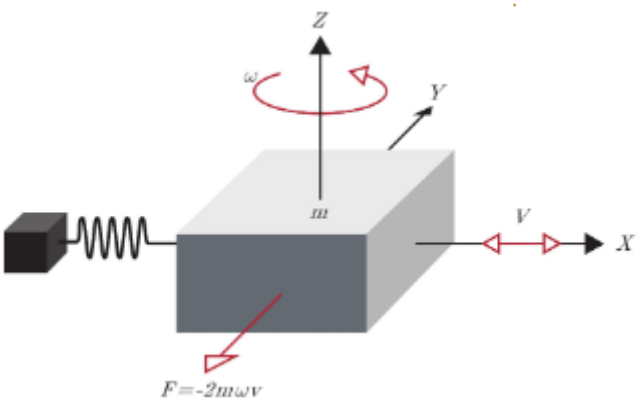

Fig. 2.6 Visualization of the working of a MEMS gyroscope

2.1.5 IMU

Inertial Measuring Unit or IMU is a device with accelerometers, gyroscopes and often also include magnetometers. An IMU that has a minimum of 3 accelerometers and a gyroscope that can pivot along three axes (or multiple gyroscopes to cover the three axes) is able to detect movements along 6 degrees of freedom, accelerations along the x,y and z-axis and the roll, pitch and yaw. Using the data given by an IMU, you can calculate the movements of an object, by using the integral of the acceleration over time to find the change in velocity and the integral of the velocity over time to find the position. However this will only give you the movements of the object but won't be able to give a position on Earth, unless you know the exact coordinates, velocity and acceleration at the starting point. This instrument usually does not come with a system to perform the calculations and filtering to provide the position.

The MOTUS, also developed by Advanced Navigation, is a MEMS IMU (Fig. 2.7). Because this is an IMU, it does not come with GNSS aid, and only 3 accelerometers, gyroscopes and magnetometers.

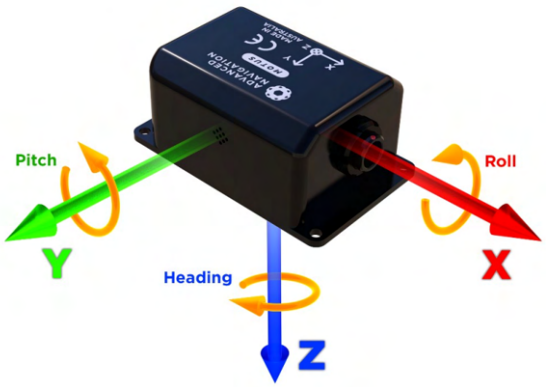

Fig. 2.7 Representation of the three axes of the MOTUS IMU and the three possible rotations.

2.1.6 AHRS

AHRS is an Attitude Heading Reference System. It is a combination of accelerometers, magnetometers and gyroscopes but the difference with an IMU is that it includes a system to calculate the heading of the platform. With gyroscopes suffering from natural drift, this system will also include a sensor fusion algorithm to compensate for this drift using the data from the magnetometers and accelerometers (Wang et al., 2015). Roll and pitch can be calculated using acceleration data, however yaw cannot be calculated from acceleration because gravity is always pulling in the same direction, no matter what the rotation of the accelerometers are. The heading of a vehicle is the direction it's pointing to. A heading of 0° means the vehicle is pointing with its noise towards the true north on Earth.

2.1.7 Magnetometers

A magnetometer measures the direction and strength of a magnetic field. The most basic example of a magnetometer is a compass, which points to the north of Earth's magnetic field. Magnetometers are used in the AHRS of a vehicle as a heading reference. The MOTUS uses a 3-axis magnetometer.

2.1.8 Sensor fusion algorithm

The SPATIAL INS/GNSS comes with Advanced Navigation's sensor fusion algorithm, which they claim is up to ten times more accurate than a standard Kalman filter. A sensor fusion algorithm is important in our case during a kinematic experiment to mitigate the drift of the gyroscopes. Gyroscopes suffer from drift which if not corrected or mitigated would be horrible when the accelerations needs to be corrected using a rotation matrix that uses the roll, pitch and yaw (Slabaugh, 1999).

A Kalman filter is an estimation algorithm, it estimates hidden variables using measurements that are inaccurate and uncertain and will also estimate the future state of the system using past estimations. It is a recursive algorithm because the new measurements are processed as soon as they're obtained, instead of having to wait until all measurements are made before being processed. It's called a filter because it makes the best estimate from data that contains noise, so it does filter out noise. The reason Advanced Navigation's algorithm can be so much more accurate than a standard Kalman filter is because the input of the precision and noise type of each measurement (accelerometer, gyroscope) is important for accurate predictions. Because they have intimate knowledge of the parameters of each sensor, that input will be more accurate compared to using a best estimate. This sensor fusion algorithm combines measurements made by different sensors in order to improve the estimate and predictions it outputs.

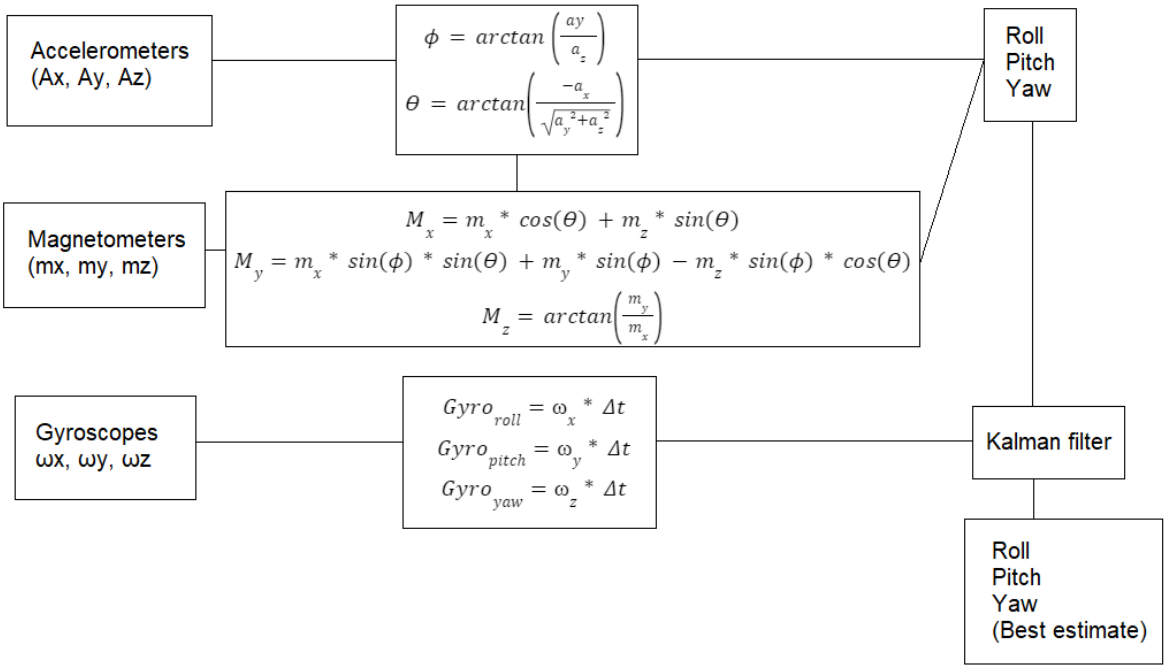

Fig. 2.8 Visual representation of a sensor fusion algorithm

On Fig. 2.8 m_x, m_y, m_z are the measurements made by the magnetometers along the x-, y- and z-axis that need to be adjusted for the heading/rotation of the platform to obtain the values in a geocentric reference frame, ω_x, ω_y, ω_z the angular velocity around the x-, y- and z-axis.

2.1.9 INS

An INS is the combination of accelerometers, gyroscopes and a GPS with a system to filter and calculate the position of the object. Usually a Kalman filter will be used for real-time kinematics (RTK). The Kalman filter will fuse the sensor data provided by the different instruments, which will be more precise than only using accelerations or accelerations and gyroscope, to predict future positions using previous data but also uses the noise type that was observed in the laboratory to make better predictions. The predictions are updated once the observations are made for the next-step and the result that is output will be a weighted average from the prediction and observation step.

The MEMS INS/GNSS model Spatial, developed by Advanced Navigations, is a miniature INS. This model is equipped with 3 accelerometers, 3 magnetometers, 3 gyroscopes, a thermometer, barometric pressure sensor and a GNSS receiver. It is

incorporated with a neural network sensor fusion algorithm from Advanced Navigation.

2.1.10 Fixed-wing rotor drone

Thanks to the very low constraints while using this INS/GNSS model (low voltage, small size and low weight), there is almost no platform the SPATIAL can't be mounted on. For my airborne gravimetry experiment I opted for a fixed-wing rotor drone (Fig. 2.9) called the BOREAL LAB drone. This model can fly for 8 hours and can be deployed in as little as 30 minutes. It has a maximum payload of 7kg and comes with an integrated 60W generator. A fixed-wing rotor drone means it has one rigid wing, which depending on the model can be detached for easier storage and transportation. Just like a plane the wing will be responsible for the lift, unlike multi-rotor drones that use their rotors for lift. The rotor, attached to the back of the drone, is used to move forward. On the wings are also the flaps to increase lift and drag (Fig. 2.10). The types of drones are usually launched using a slingshot launch platform. A support that can move on the railing is pulled back and the cord attached to it is wound up (Fig. 2.11). The drone is installed on the support, which is blocked at the back so it doesn't fall off and open at the front so the drone can be launched off it. Using a ripcord the support is no longer locked in place and launches forward. At the end of the railing the support is blocked and the drone launches off the platform. During the launch a trained professional uses a drone controller to manually control the movements of the drone. Once a high altitude is reached he switches over to an automatic flight that is pre-set but can be modified on the fly.

Fig. 2.9 The Boreal Lab drone approaching the end of the slingshot launch platform, moments before taking flight

Fig. 2.10 Back of drone showing the rotor and flaps on the wings

Fig. 2.11 Portable crane scale shows the force on the cord before launch (203.3 kg or 1993.7 N)

One of the earlier test flights at the ONERA flight area in *Esperce* was set up to study the vibrations that are sensed by the different instruments on-board. For this, 7 accelerometers were placed at different locations on the drone (seen on Fig. 2.12) in order to analyze the vibrations at each part. Rubber bushings were also used to try and minimize the vibrations recorded by the accelerometers. Figure 2.13 shows the wind tunnel data for this drone model.

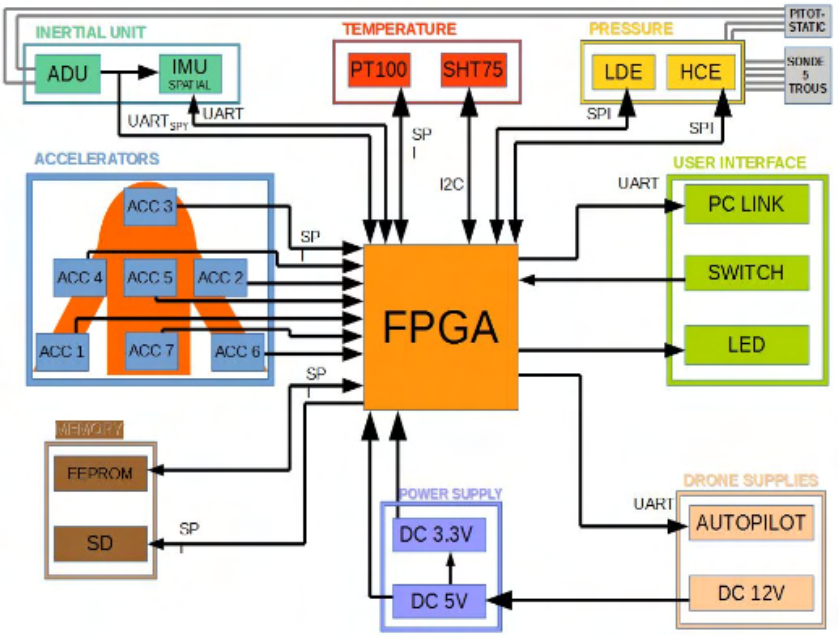

Fig. 2.12 Visual representation of the layout of the 7 different accelerometers on-board and how all parts are connected to the Field-programmable gate array (FPGA)

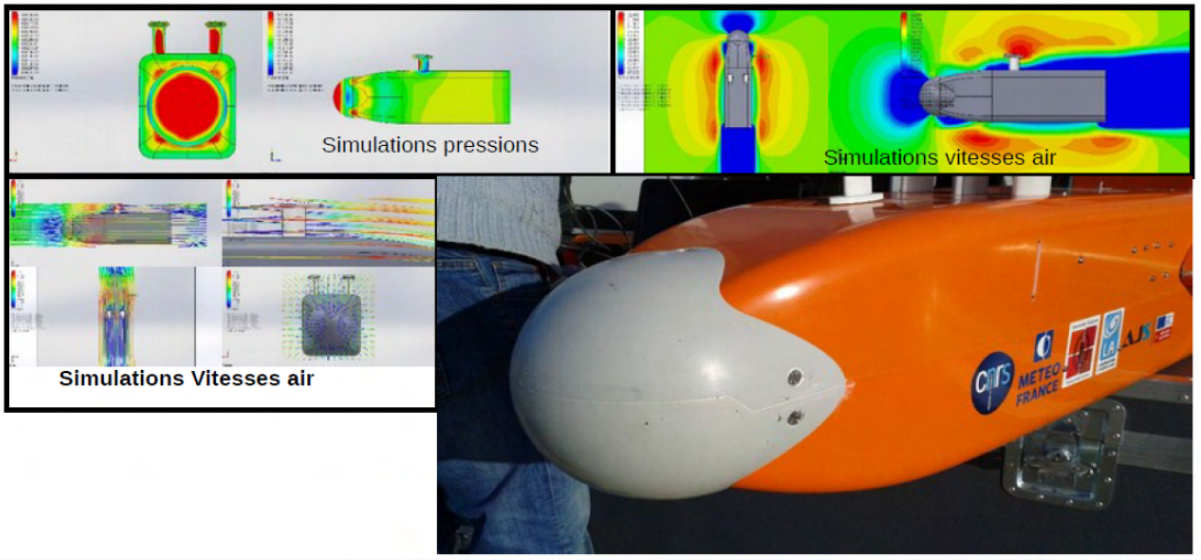

Fig. 2.13 Wind tunnel data of the fuselage of the Boreal LAB drone, performed by aerology laboratory LAERO (OMP)

2.2 Methodology

2.2.1 Rotation Matrix

In the previous chapter we saw that for mobile gravimetry, in order to obtain the gravitational component I need to remove the kinematic accelerations (derived from GNSS data) from the specific forces recorded by the accelerometers (Eq. 1.17). The gravitational component will be along the z-axis of the INS/GNSS when it is placed perfectly horizontal. For an in situ experiment (e.g. solid Earth tides experiment which will be presented later) this can be arranged since the INS/GNSS will not move so the z-axis stays aligned with the Down axis which points to the center of the Earth, as seen on Fig. 2.14 and 2.15. For mobile gravimetry however when the INS/GNSS is attached to the inside of a van (see Cammazes dam experiment, chapter 5) or a UAV (see airborne gravimetry experiment, chapter 6) the INS/GNSS will not be perfectly horizontal. In those situations the radial gravitational component will be measured partly by the three different accelerometers. In order to record the radial gravitational component along the z-axis of the INS/GNSS and to remove the kinematic accelerations (Eq. 1.17), I will use a rotation matrix for those experiments in order to always work in the NED-frame (the GNSS data will also be converted to the NED-frame in chapter 6). To apply the rotation matrix I will use the roll, pitch and yaw recorded by the INS/GNSS gyroscopes.

A body can rotate about its three orthogonal axes (x, y and z). The rotation about the x-axis is the roll, the y-axis is the pitch and z-axis is the yaw. Three orthogonal accelerometers and gyroscopes can therefore measure movements along 6 dimensions of freedom. For the SPATIAL the Tait-Bryan angle convention is used, where an elevation of zero degrees means the platform is horizontal (versus Euler angle convention where zero degrees means the platform is vertical).

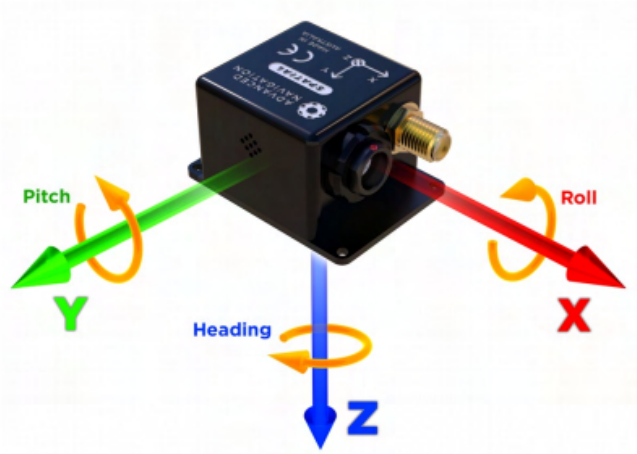

Fig. 2.14 Representation of the three axes of the SPATIAL INS/GNSS and the three possible rotations.

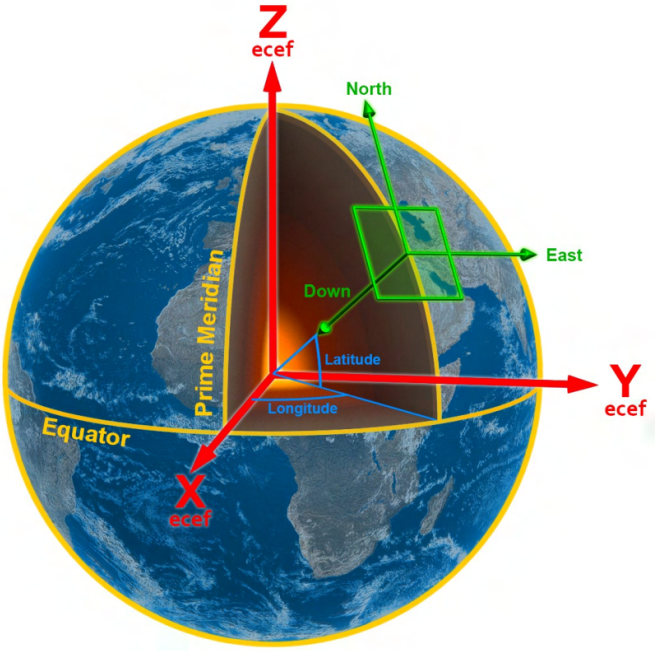

Fig. 2.15 Visual presentation of Earth and the XYZ reference frame (Earth's core as origin) and the NED local reference frame of an instrument positioned horizontally on Earth with the x-axis pointing North (image credit: Advanced Navigations)

These three possible rotations can be presented by the following basic rotation matrices.

$$R_z(\gamma) = \begin{bmatrix} cos\,\gamma & sin\,\gamma & 0 \\ -sin\,\gamma & cos\,\gamma & 0 \\ 0 & 0 & 1 \end{bmatrix}$$
$$R_y(\beta) = \begin{bmatrix} cos\,\beta & 0 & -sin\,\beta \\ 0 & 1 & 0 \\ sin\,\beta & 0 & cos\,\beta \end{bmatrix} \quad \text{(Eq. 2.4.a)}$$
$$R_x(\alpha) = \begin{bmatrix} 1 & 0 & 0 \\ 0 & cos\,\alpha & sin\,\alpha \\ 0 & -sin\,\alpha & cos\,\alpha \end{bmatrix}$$

A single rotation matrix that describes the rotations of a body along the three axes can be obtained by multiplying these three elemental matrices. The order in which they are multiplied will be important as they do not commute, so a total of 6 possible composite rotation matrices can be obtained that are all valid (all possible solutions are included in the annex).

For aerospace applications the most common order is yaw, pitch and lastly roll, the order of rotations goes from right to left, first R_y * R_z are multiplied, then R_x * R_{yz} .

$$\mathrm{R}=\mathrm{R}_x(\alpha)R_y(\beta)R_z(\gamma)$$
$$= \begin{bmatrix} 1 & 0 & 0 \\ 0 & cos\,\alpha & sin\,\alpha \\ 0 & -sin\,\alpha & cos\,\alpha \end{bmatrix} \begin{bmatrix} cos\,\beta & 0 & -sin\,\beta \\ 0 & 1 & 0 \\ sin\,\beta & 0 & cos\,\beta \end{bmatrix} \begin{bmatrix} cos\,\gamma & sin\,\gamma & 0 \\ -sin\,\gamma & cos\,\gamma & 0 \\ 0 & 0 & 1 \end{bmatrix}$$
$$= \begin{bmatrix} cos\,\beta\,cos\,\gamma & cos\,\beta\,sin\,\gamma & -sin\,\beta \\ sin\,\alpha\,sin\,\beta\,cos\,\gamma - cos\,\alpha\,sin\,\gamma & sin\,\alpha\,sin\,\beta\,sin\,\gamma + cos\,\alpha\,cos\,\gamma & sin\,\alpha\,cos\,\beta \\ cos\,\alpha\,sin\,\beta\,cos\,\gamma + sin\,\alpha\,sin\,\gamma & cos\,\alpha\,sin\,\beta\,sin\,\gamma - sin\,\alpha\,cos\,\gamma & cos\,\alpha\,cos\,\beta \end{bmatrix}$$

(Eq. 2.4.b)

The SPATIAL placed horizontally on a table will see the gravity vector aligned with its z-axis. If I multiply the composite rotation matrix by a vector along a z-axis I obtain the following:

$$= \begin{bmatrix} cos\,\beta\,cos\,\gamma & cos\,\beta\,sin\,\gamma & -sin\,\beta \\ sin\,\alpha\,sin\,\beta\,cos\,\gamma - cos\,\alpha\,sin\,\gamma & sin\,\alpha\,sin\,\beta\,sin\,\gamma + cos\,\alpha\,cos\,\gamma & sin\,\alpha\,cos\,\beta \\ cos\,\alpha\,sin\,\beta\,cos\,\gamma + sin\,\alpha\,sin\,\gamma & cos\,\alpha\,sin\,\beta\,sin\,\gamma - sin\,\alpha\,cos\,\gamma & cos\,\alpha\,cos\,\beta \end{bmatrix} \begin{bmatrix} 0 \\ 0 \\ 1 \end{bmatrix}$$

$$= \begin{bmatrix} -sin\,\beta \\ cos\,\beta\ sin\,\alpha \\ cos\,\beta\ cos\,\alpha \end{bmatrix} \quad \text{(Eq. 2.4.c)}$$

Using the above matrices and the values recorded by the accelerometers, the roll and pitch can be calculated from the accelerations measured along the x-, y- and z-axis which is used for the sensor fusion algorithm (Fig. 2.8). As mentioned earlier the yaw can not be calculated using only the accelerations measured by the accelerometers. The equations to do so are listed below:

$$\phi = arctan\left(\frac{ay}{a_z}\right)(roll) \quad \text{(Eq. 2.5)}$$

$$\theta = arctan\left(\frac{-a_x}{\sqrt{a_y{}^2+a_z{}^2}}\right)(pitch) \quad \text{(Eq. 2.6)}$$

2.2.2 Fourier analysis

During the airborne gravimetry experiment (chapter 6) the INS/GNSS and IMU recorded with a sampling frequency of 16.6Hz on top of that during that experiment there were high levels of noise recorded due to vibrations caused by the rotor, on-board equipment and wind. The resulting signal was very noisy for both amplitude and frequency. In order to study the small effect of altitude changes on the gravimetric component, this signal would need to be filtered extensively. From the airborne gravimetry studies mentioned in the state of the art (Ch. 1.2), low-pass filters of 120-160s were used and I will use the same for my airborne gravimetry study. For this method I apply the fast Fourier transform (FFT) (Cochran et al., 1967) to my signal, which will compute the discrete Fourier transform (DFT). This allows me to change my signal from its time domain to its frequency domain.

```
next_ACC = 2^nextpow2(length(ACC));
fft_ACC = fft(ACC, next_ACC);
fshift_ACC = Fs*(0:next_ACC/2)/next_ACC;
power_ACC = abs(fft_ACC)/next_ACC;
power1_ACC = power_ACC(1:next_ACC/2+1);
power1_ACC(2:end-1) = 2*power1_ACC(2:end-1);
yshift_ACC = fftshift(fft_ACC);

for i=1:1:509
    yshift_ACC(i) = 0;
end
for i=513:1:1024
    yshift_ACC(i) = 0;
end

ifft_ACC = ifft(ifftshift(yshift_ACC));
ACC_filtered = real(ifft_ACC);
ACC_filtered = ACC_filtered';
```

Fig. 2.16 Example of MatLab code for FFT and filtering

First I would add a padding to my numerical data until its length reaches the next power of 2, this padding would consist of trailing zeros at the end of the signal. From this data I take the FFT, calculate the frequency range and the amplitude associated with each frequency (Fig. 2.16).

In this example, Fs*(0:next_ACC/2)/next_ACC is to satisfy the Nyquist limit (Eq. 2.7). With the sampling frequency set to 16.6Hz, to recover all the Fourier components of a waveform, the highest waveform frequency will be 8.3Hz, else I would not be able to correctly reconstruct the signal.

$$f_{Nyquist} = \frac{1}{2}\mathcal{V},\ with\ \mathcal{V}\ =\ 16.6Hz \qquad \text{(Eq. 2.7)}$$

The graph below (Fig. 2.17) is an example of the spectrum of a signal's frequency domain, where 8.3Hz is the highest frequency.

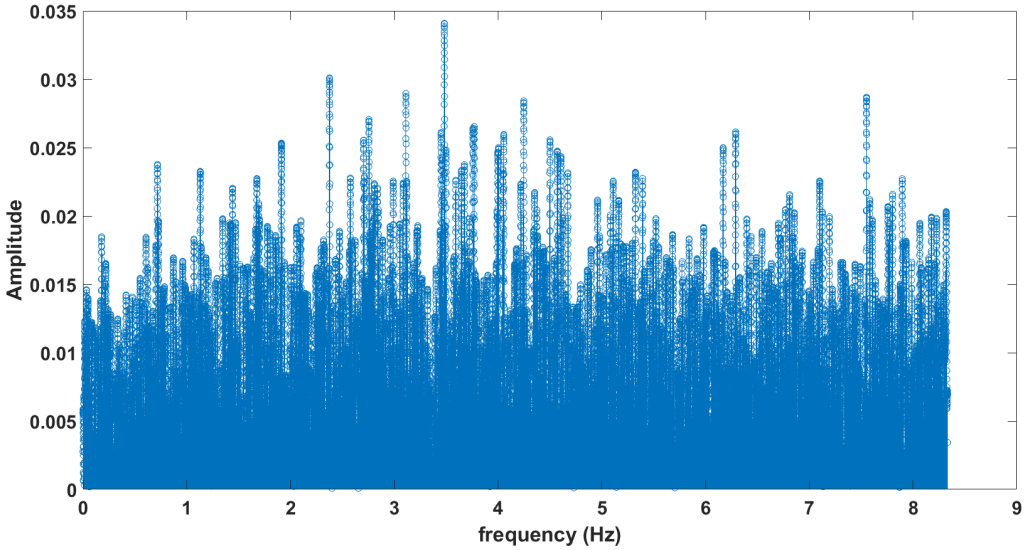

Fig. 2.17 Frequency domain of the signal when the drone was at rest with the motor turned on

If I would not remove any frequencies and reconstruct the signal from its Fourier components above I would obtain the following figure.

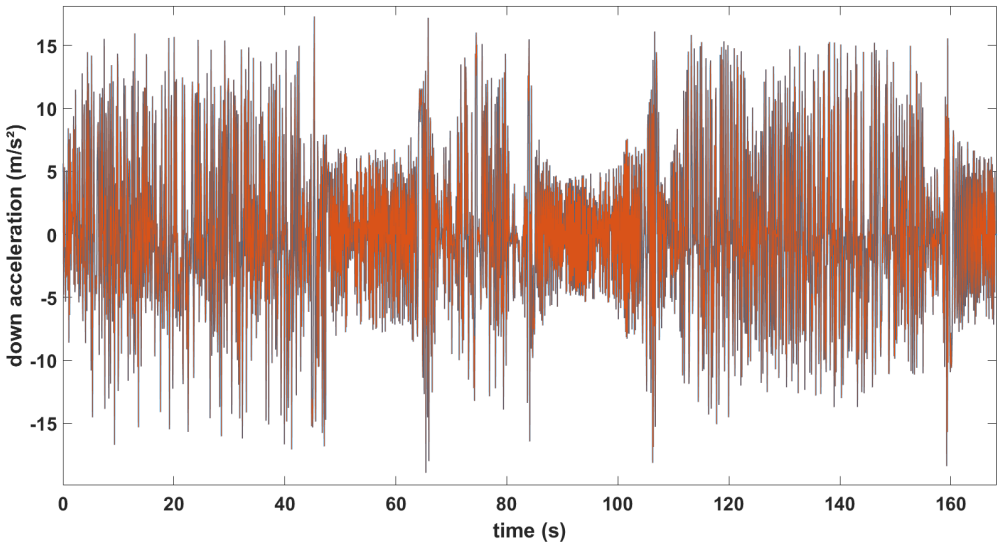

Fig. 2.18 Acceleration (down) caused by the motor when the drone is at rest. Raw signal in blue and reconstructed signal from Fourier components, satisfying Nyquist limit

On figure 2.18 the original signal is presented in blue with a slightly bigger linewidth, but is barely visible because, as expected, since the Nyquist limit is satisfied both signals are the same.

By finding the number associated with the frequencies that I want to eliminate I can set the values at these frequencies to 0 before I reconstruct the signal with the remaining frequencies (Fig. 2.19. To smoothen the filtering different window functions can be used (e.g. Hamming function).

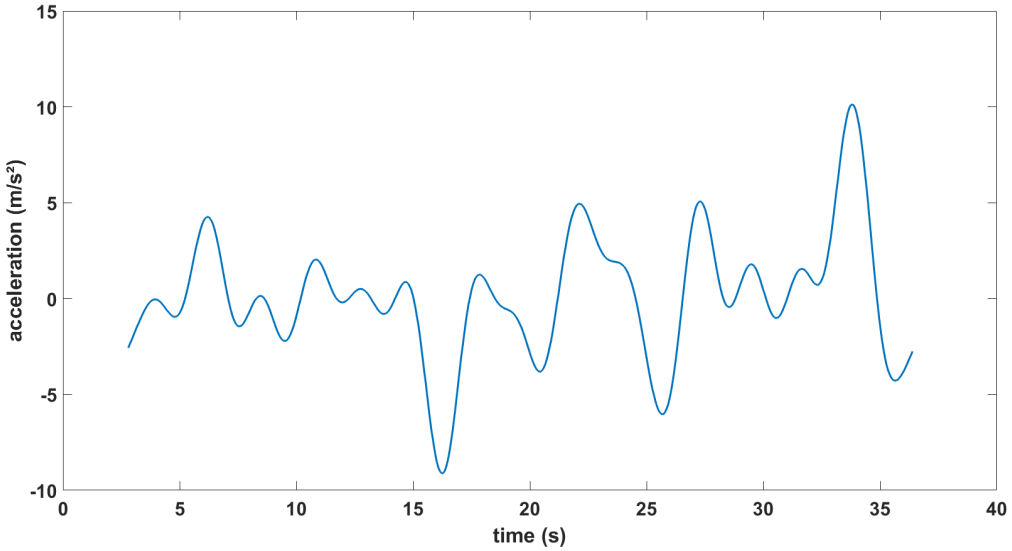

Fig. 2.19 Example if a signal after filtering out (low-pass) certain frequencies

2.2.3 Cross wavelet transform

In chapter 4 I will present the study of using the INS/GNSS and CG-5 gravimeter to detect the solid Earth tide signals using the data of an in situ experiment. Unlike the previous method that aims at filtering a signal, I will want to analyze the correlation between the recorded data and the theoretical signal of the Earth tides. A simple calculation of the correlation between both signals will give a very bad result since the INS/GNSS data contains a lot of noise and the theoretical signal will not. The best way to extract a correlation for certain periods between those signals is a cross wavelet transform (Torrence et al., 1998 & Torrence et al., 1999).

A Fourier analysis of my data assumes that the underlying processes for those signals are stationary in time, which isn't the case for solid Earth tides. A wavelet transform changes the time series into time frequency space, so it can find localized intermittent periodicities (Gaillot et al., 1997 & Meyer and Roques, 1993 & Grinsted et al., 2004 & Jevrejeva et al., 2003 & Chambodut et al., 2005). The two classes of

wavelet transforms are Continuous Wavelet Transform (CWT) and the Discrete Wavelet Transform (DWT). Because of our noisy INS/GNSS data and the low amplitudes of solid Earth tides I will want to extract low signal-to-noise ratio (SNR) signals for which CWT is better. Using two CWTs, the Cross Wavelet Transform (XWT) can be calculated, which presents the common power and phase in time frequency space.

A wavelet is a function with zero mean and is localized in both frequency and time. The Morlet wavelet (Fig. 2.20, which is the wavelet that I used for my CWT and XWT is defined as:

$$\psi_0(\eta) = \pi^{-1/4} e^{i\omega_0 \eta} e^{(-1/2)\eta^2} \qquad \text{(Eq. 2.8)}$$

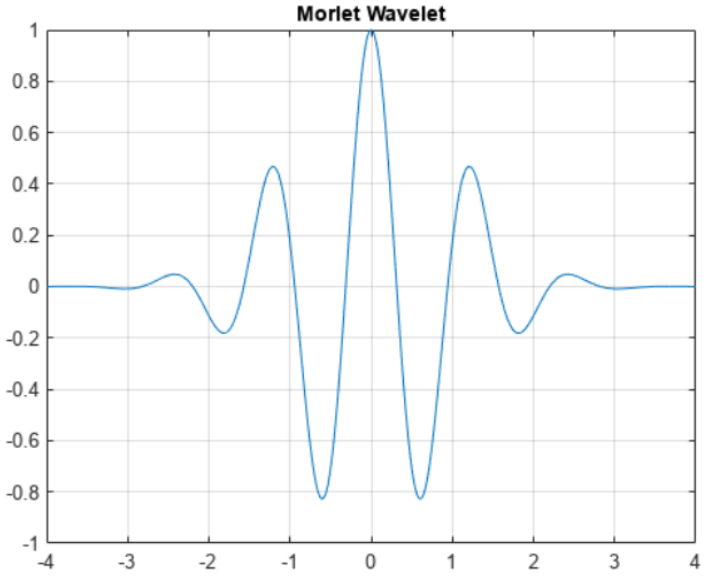

Fig. 2.20 Example of Morlet wavelet

This wavelet is applied to our time series as a band-pass filter to obtain the CWT. An example of a CWT is presented on Fig. 2.21 which uses a theoretical signal of the solid Earth tides. The horizontal axis presents the time while the vertical axis shows the different frequencies. A yellow color means a high correlation of the signal with those frequencies at that specific time. A wavelet varies in scale (s) and time (t) with η=s*t and normalized to have the unit energy. The convolution of the time series (x_n) with the scaled and normalized wavelet is

$$W_n^X(s) = \sqrt{\frac{\delta t}{s}} \sum_{n'=1}^{N} x_{n'} \psi_0\left[(n' - n)\frac{\delta t}{s}\right] \qquad \text{(Eq. 2.9)}$$

The wavelet power is $\left|W_n^X(s)\right|^2$ and the complex part is the phase. A cone of influence is added because the wavelet is not entirely localized in time. Everything that falls outside of this cone can be ignored due to edge effects.

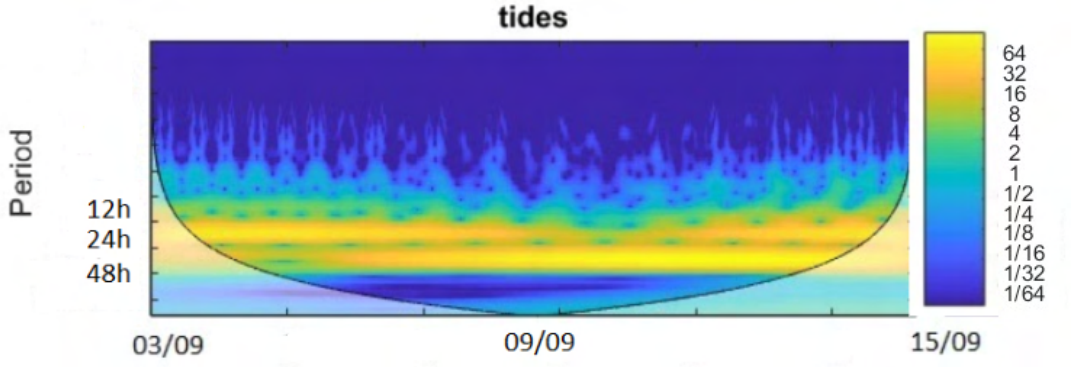

Fig. 2.21 Example of CWT of the theoretical tide signal (Ch. 4)

The cross wavelet transform of two time series (e.g. theoretical tides: x_n and recorded data: y_n) is $W^{xy} = W^x W^{y^*}$, the cross wavelet power is calculated from $\left|W^{xy}\right|$ and the complex argument of W^{xy} is the relative phase between both signals. Fig. 2.22 is an example of a cross wavelet transform where we can see high correlation for certain frequencies between the data recorded by a CG-5 and theoretical data. Arrows pointing to the right means the signals are in phase at those times, up and down means the signals are out of phase, with up (+90°) corresponding to the first time series leading the second one, down (-90°) means the second signal is leading.

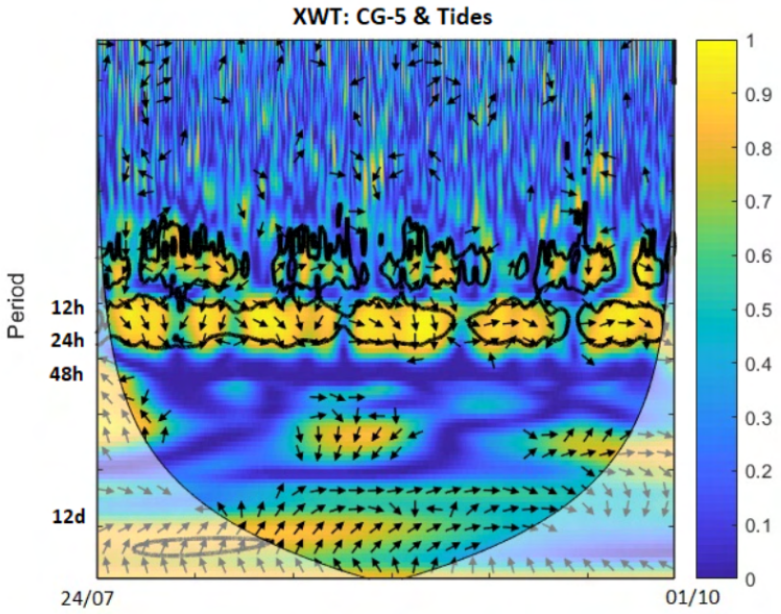

Fig. 2.22 Example of XWT of theoretical tides and CG-5 data

2.2.4 Earth tide model used

In our study to validate the results obtained by the MEMS INS I decided to compare our measurements with the well-known theoretical solid tide model called Tsoft (Van Camp and Vauterin, 2005). This software predicts the periodical gravity variations due to solid Earth tides. It integrates pre-processing to correct the artifacts of the analyzed time series (outlier, step, missing data). For this purpose, it is based on powerful filtering tools either in the frequency domain (FFT) or in the time domain (e.g. 2-poles Butterworth filter).

Land tides or solid tides are also defined as body tides in solid Earth geosciences (Sung-Ho, 2020). Like ocean tides, the Moon has the greatest effect on body tides because it is closer to the Earth. The Sun does have an effect on body tides as well because of its very large mass and its strong gravitational field. As the Earth rotates around the Sun and the Moon each of their gravitational fields pull on the Earth. Because of this pull there are small deformations (or bulges) on the Earth's surface known as body tides. These bulges face the Moon and the Sun as the Earth rotates. Tsoft model predict Earth displacement and gravity change due to Earth tides in time but also in space. Body tides are lower than ocean tides and the displacement of the Earth's surface is usually no greater than ±30 cm.

A simplified model was given to express the gravity solid tides g_s:

$$g_s = g_0 - g_d - g_a - g_{oc} - \varepsilon \qquad \text{(Eq. 2.10)}$$

where g_0 are gravity observations, g_d zero drift (for spring gravimeter and for INS due to temperature), g_a the atmospheric load, g_{oc} the ocean loading and ε represents errors and noises. Removing g_0, g_d, g_a, g_{oc} then g_s is regarded as the sum of different solid tide waves.

Now that I've introduced the material I used for my experiments and the methodology, I will now go over the different experiments performed in the following chapters. The order not necessarily being the order that they were performed, but rather the idea and method behind them.

CHAPTER 3 Study case: Analysis of temperature and altitude influence

Before using the INS/GNSS for mobile gravimetry, I first learned the technical characteristics and how the instrument worked. I then modified the software to record the data shown on the Advanced Navigation software interface. I studied its characteristics during an experiment at the GET (Géosciences et Environnement Toulouse) laboratory over the course of multiple months to answer the first question, is the precision of this instrument good enough for gravimetric measurements.

Advance Navigation uses the same protocol for all their products. The Advanced Navigation Packet Protocol (ANPP, table 3.1) is used to send the data from the instrument. These packets include information about the system, state and configuration. The system packets are used to acknowledge success or failure, to identify the instrument used, its device ID, software version etc. The header of these packets include the packet ID and length. Packets with an ID less than value 20 are system packets, between 20 and 179 are state packets, and greater than 179 are configuration packets. The state packets are used to transfer the data of the different sensors. Below is some example code to read and write the data from state packet 28, which includes the raw data from the three accelerometers, three magnetometers, the temperature of the instrument and the pressure (Fig. 3.1). The configuration packets include the baud rate, the GNSS frequencies that indicate which frequencies of a constellation are enabled, the rate at which packets are received etc.

```
case ANPacket.PACKET_ID_RAW_SENSORS:
    if (packet.length == 48)
    {
    string name = DateTime.Now.ToString("yyyy-MM-dd");
    string path = @"C:\ACC_" + name + ".txt";
    using (System.IO.StreamWriter file = new System.IO.StreamWriter(path, true))
    {
        ANPacket28 anPacket28 = new ANPacket28(packet);
        this.Invoke((MethodInvoker)delegate
        {
            textBoxAccX.Text = (anPacket28.accelerometers[0]).ToString();
            textBoxAccY.Text = (anPacket28.accelerometers[1]).ToString();
            textBoxAccZ.Text = (anPacket28.accelerometers[2]).ToString();
            textBoxTemp.Text = (anPacket28.pressureTemperature).ToString();
            textBoxPressure.Text = (anPacket28.pressure).ToString();
            BoxMagX.Text = (anPacket28.magnetometers[0]).ToString();
            BoxMagY.Text = (anPacket28.magnetometers[1]).ToString();
            BoxMagZ.Text = (anPacket28.magnetometers[2]).ToString();
            richTextBox1.AppendText("Received Raw Sensors Packet\n");
            richTextBox1.AppendText(Convert.ToString(packet.id));
            richTextBox1.AppendText(" \n");

            file.WriteLine((anPacket28.accelerometers[0]).ToString() + " " + (anPacket28.accelerometers[1]).ToString() + " " +

        });
    }
```

Fig. 3.1 Part of the program to receive and write the data included in Packet 28 (ANPP), which includes the three accelerometers.

Raw Sensors Packet				
Packet ID				28
Length				48
Field #	Bytes Offset	Data Type	Size	Description
1	0	fp32	4	Accelerometer X (m/s/s)
2	4	fp32	4	Accelerometer Y (m/s/s)
3	8	fp32	4	Accelerometer Z (m/s/s)
4	12	fp32	4	Gyroscope X (rad/s)
5	16	fp32	4	Gyroscope Y (rad/s)
6	20	fp32	4	Gyroscope Z (rad/s)
7	24	fp32	4	Magnetometer X (mG)
8	28	fp32	4	Magnetometer Y (mG)
9	32	fp32	4	Magnetometer Z (mG)
10	36	fp32	4	IMU Temperature (deg C)
11	40	fp32	4	Pressure (Pascals)
12	44	fp32	4	Pressure Temperature (deg C)

Table 3.1 Information of packet 28 from SPATIAL's reference manual

3.1 Spatial Manager

I've used this software (Fig. 3.2) to configure the INS/GNSS before launching the program to record the data. Most important things to note is the virtual COM port that is created and the instrument connects to. I also use it to set the baud rate and to set

the packets I want to receive and the corresponding packet rates (Fig. 3.3). Once I've done this I disconnect the instrument, and the settings will be saved.

Fig. 3.2 General interface of Spatial Manager showing the position on a satellite image, the amount of satellites it's connected to, the rotation of the instrument.

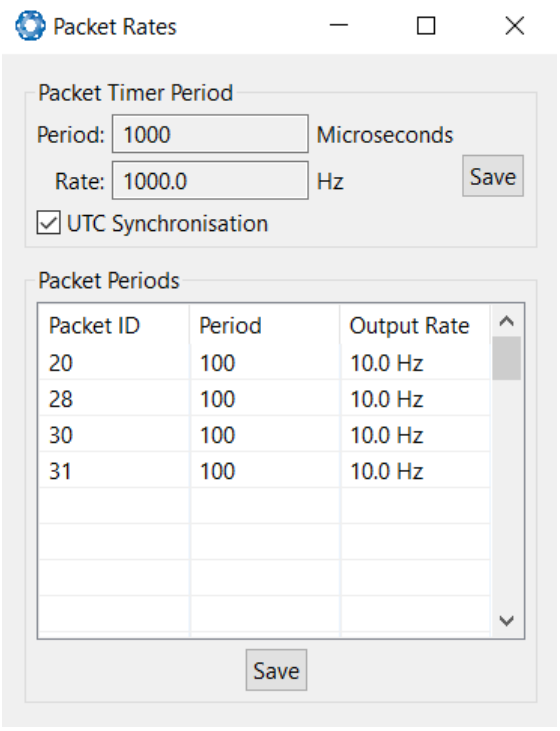

Fig. 3.3 Interface to select the packets to send and the frequency

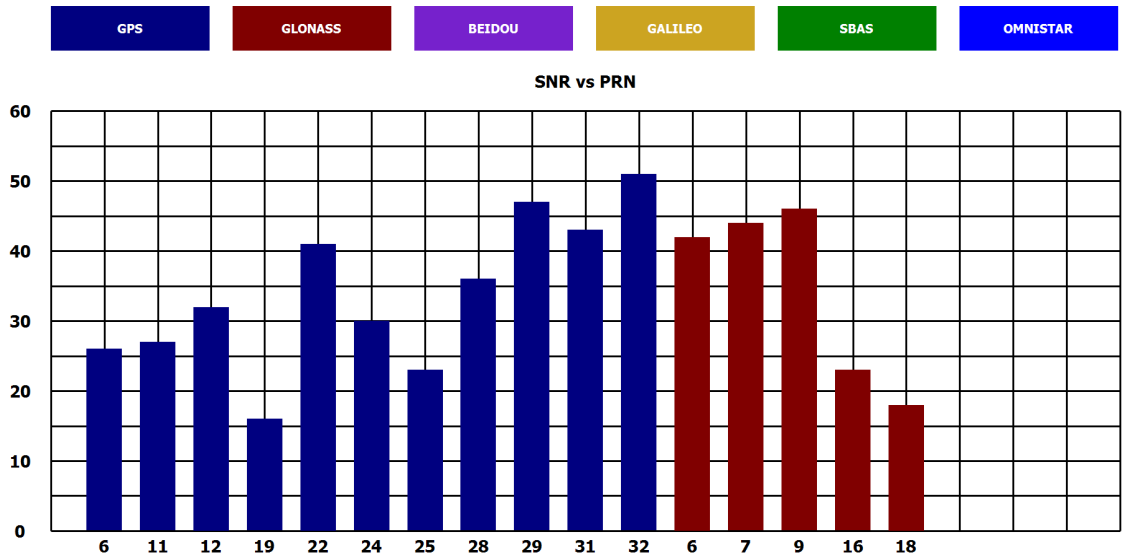

Fig. 3.4 Interface to see in detail which satellite of each constellation the instrument is connected with

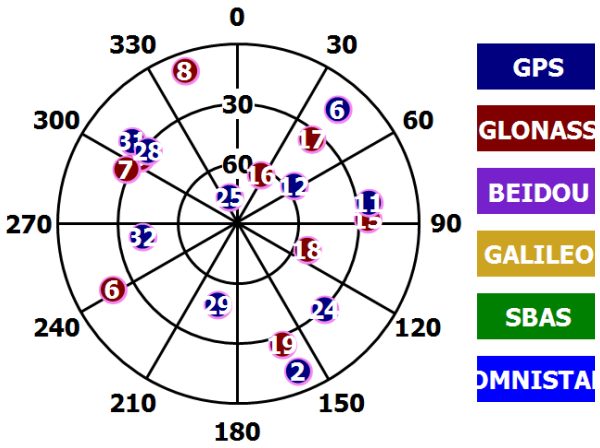

Fig. 3.5 Skymap of the connected satellites

Using the Spatial Manager software I can see in detail what satellites of each constellation we're connected to and the corresponding signal-to-noise ratio (Fig. 3.4). I can also see their position in the sky using the skymap (Fig. 3.5).

The software also provides a live plot of the velocity and acceleration measured by the INS/GNSS (Fig. 3.6). This image shows the corresponding velocity, acceleration and g-force of the INS/GNSS being pulled up quickly and then stopped. We can see a negative acceleration first, because the z-axis is pointing down followed by a positive acceleration when slowing down before coming to a complete stop.

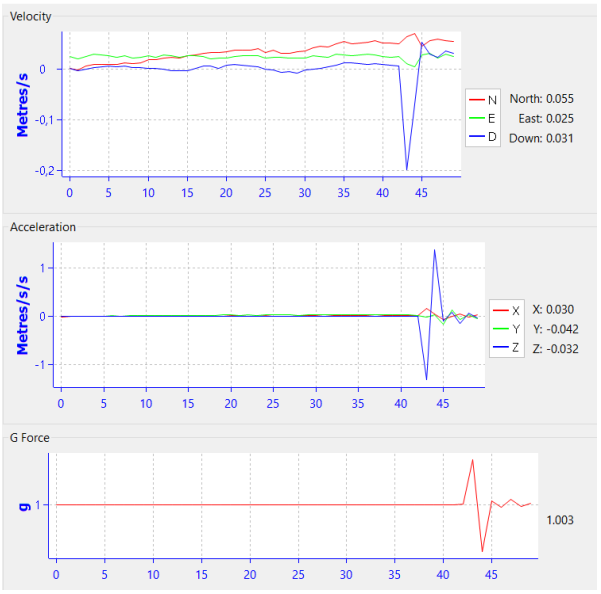

Fig. 3.6 Real-time charts of the velocity, acceleration and g in real time

When the INS/GNSS is at rest we see that the acceleration for all three axes is 0 m/s², but the INS/GNSS correctly shows a g-force close to 1g, which becomes more than 1 when pulled up (simulating increase in gravitational pull), and lower than 1 when slowing down. This is a matter of calibration, which is corrected from g(φ) (using WELMEC formula for our latitude and elevation, see Eq. 1.11), as some will prefer to show an acceleration along the z-axis equal to the local gravity value (in m/s²) and only show an acceleration of 0 m/s² when in free-fall. This is what I preferred and will be reflected in the data of the first three described experiments, however for the drone experiment the data shows an acceleration of 0 m/s² along the z-axis when at rest. These real-time charts help with understanding the orientation of

the different sensors and axes. It also helps with understanding how the accelerometers measure accelerations at rest or in free-fall.

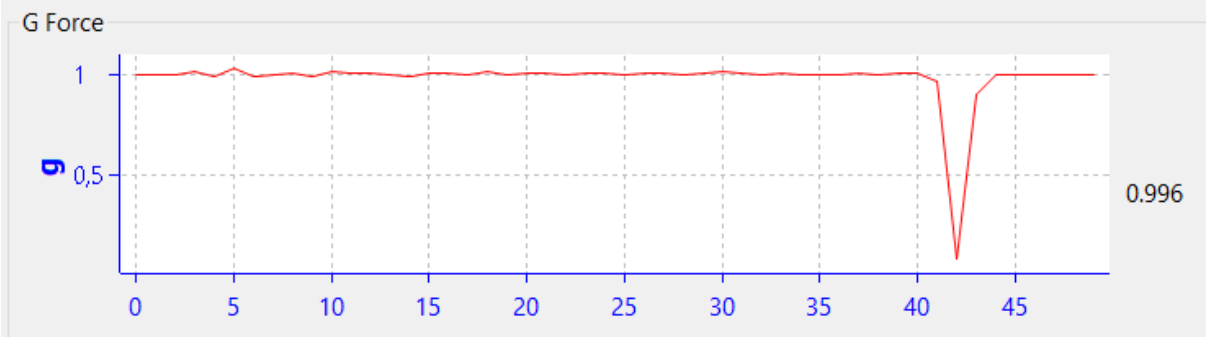

Fig. 3.7 Real-time chart of g when the instrument was dropped from a small height (free-fall)

Figure 3.7 shows the g-force when the INS/GNSS was dropped from a low height, because the INS/GNSS was in free-fall for a short duration at 42s the g-force tends towards 0.

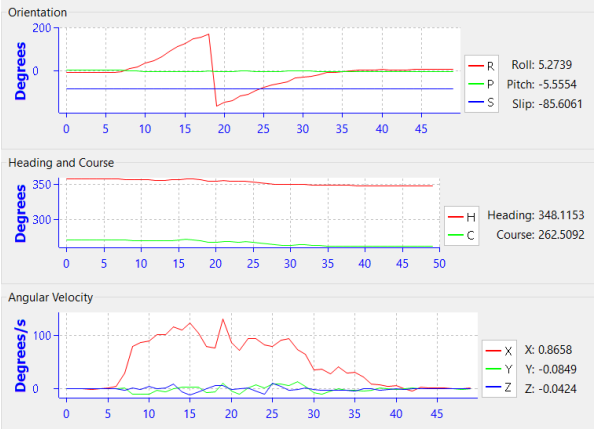

Fig. 3.8 Real-time charts of the gyroscope data

Measurements from the gyroscopes are also plotted in real time as seen in Fig. 3.8. In this example the INS/GNSS is rotated 360° around its x-axis, while pointing approximately north (heading), showing a change in roll and angular velocity around the x-axis.

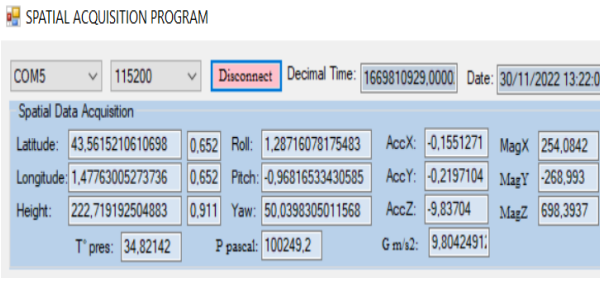

Fig. 3.9 Interface of the recording software

The Spatial acquisition program is the program I modified to save the data of the packets that are of interest to me in two text files (Fig. 3.9). This program is not used to change the settings or configuration of the INS/GNSS. One text file, named "ACC_*date*.txt" will include the sensor data, the one named "POS_*date*.txt" will contain the GNSS data.

I mentioned earlier that an accelerometer will interpret the accelerations according to general relativity and an accelerometer with its z-axis pointing in the UP direction at rest will measure an acceleration of 1g. This acceleration comes from the support counteracting the gravitational acceleration. The value measured will correspond to the gravitational pull at that point.

On Fig. 3.10 we can see an enhanced image of the INS/GNSS where we can see that the z-axis is pointing in the DOWN direction. This is why our data is presented as negative accelerations when the INS/GNSS is at rest on a support.

Fig. 3.10 Enhanced image of SPATIAL INS/GNSS

3.2 In situ experiment (Summer 2020)

The INS/GNSS was placed in a room connected to a computer from the 21st of July until the 6th of September (2020) at the GET laboratory. This room was rarely disturbed by people because it was used for storage and in general less people were present at the laboratory due to the summer holidays and a lot of people working from home as this was just after the first COVID isolation period. This was advantageous for the experiment because it meant less vibrations were recorded by people walking in the room, moving equipment etc. The INS/GNSS was placed horizontally on a foam support to absorb vibrations, and fixed to a structure to avoid any movements. Because it was placed horizontally I could just consider the accelerometric data along the z-axis which would correspond to the radial gravity component. Thanks to the presence of air conditioning throughout the summer, temperature variations in this room were lower than if the room was not cooled down. This room was positioned close to a road that leads to a parking lot, so the

presence of cars could be responsible for vibrations. There were no other instruments that could cause vibrations in this room beside the air conditioning itself.

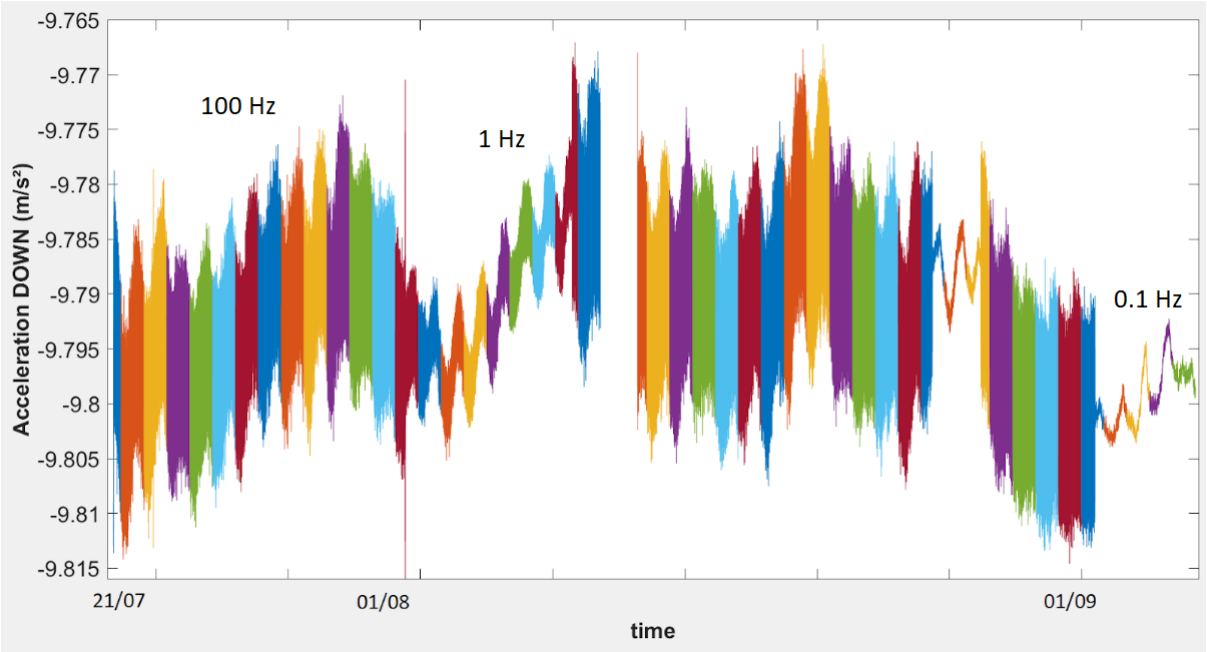

Fig. 3.11 The acceleration along the down axis, recorded from 21/07/2020 - 06/09/2020 for different frequencies.

On Fig. 3.11 each different color represents a different day. At first I recorded using a frequency of 100Hz, however I quickly noticed that with a too high frequency the noise heavily increases and the recorded data fluctuates much more around the real value. This can be clearly noticed on figure 3.11 and figure 3.12, which presents the difference between the minimum and maximum value for each day and the respective sampling frequency that was used. Each part of the graph with a different color is a different day. From the 5th of August until 11th of August a sampling frequency of 1Hz was used and there is noticeably less noise. The missing part in the graph is due to a computer malfunction that caused the data of two days to be lost. The data at the end where even less noise is visible used a sampling frequency of 0.1Hz.

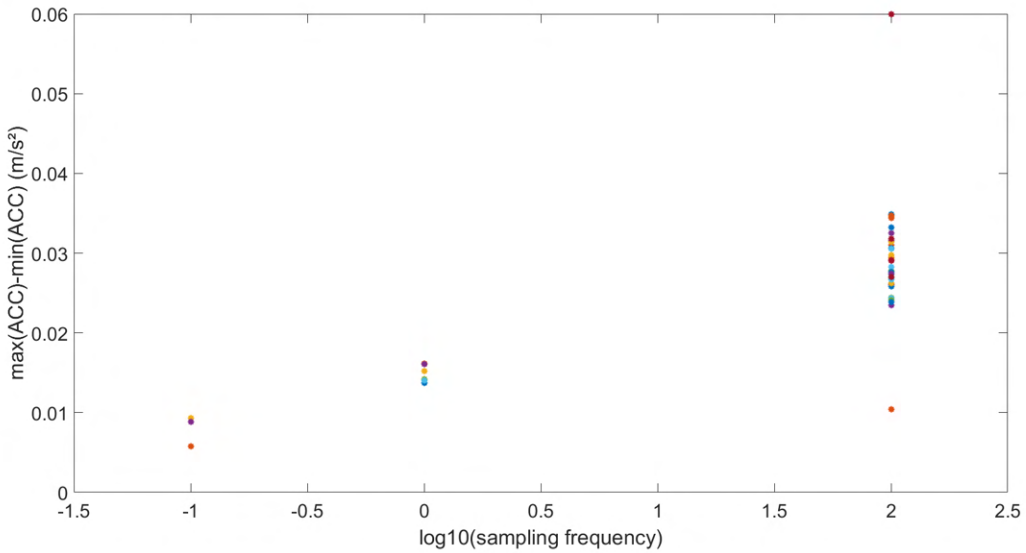

Fig. 3.12 Graph showing the difference between min-max values over the course of a day for different sampling frequencies (0.1Hz / 1Hz / 100Hz)

Analyzing figure 3.11 I immediately notice that the acceleration data shows a semidiurnal and diurnal effect. One possible phenomenon that can correspond to these diurnal and semi-diurnal variations is the solid Earth tides (Ekman, 1983; McCarty & Petit, 2004; Lau et Schindelegger, 2023, Le Provost, 2001), however they would not present such a high amplitude difference. At the time of the experiment the highest amplitude from solid Earth tides was of the order of 0.1 mGal, or 10^{-6} m/s². Figure 3.11 clearly shows that the amplitudes measured by the INS are much greater. It also shows low-frequency oscillations with a spectrum close to that of the temperature oscillations observed in Figure. 3.13. This phenomenon is well known on spring gravimeters since, if I look at the *Sung-Ho Na* model (2020) used to obtain solid tides at any point on the globe, I can see that it introduces a temperature correction, g_d (eq. 2.10) due to the temperature drift of these gravimeters. During the evening and night when the temperatures dropped the INS/GNSS would give a smaller value than throughout the morning and afternoon when temperatures rose. I also notice on figure 3.11 that the value for the acceleration along the DOWN axis rises or falls for different days in a similar way to the temperatures (Fig. 3.13). What's more, if I look at the internal temperature of the inertial unit, it too follows these same oscillations (Fig. 3.14). Another important meteorological parameter that can disrupt acquisition is atmospheric pressure. If I now look at the pressure variations observed over the same period (Fig. 3.15), I can see that they have little impact on the INS

measurements. Because it's important to distinguish if this is also a temperature dependency or a natural drift from the accelerometers I compared this with the temperature data at Toulouse for this period, figure 3.16 shows a clear correlation with a R^2=0.8528. For the days where the temperature was lower, our acceleration data is also lower, similarly for days that were hotter, the acceleration data is higher. This confirms even more the temperature influence on our measurements. Important to note is that the temperature recorded by the INS/GNSS is the temperature inside the instrument, which is higher than the outside temperature due to the heating of the electrical components while turned on.

It's no secret that accelerometers come with a strong temperature bias and a natural drift. However from this data I don't notice any major drifts, this could be in part due to the fact that when I swapped between different sampling frequencies, the INS/GNSS would be turned off and reset. I do however see that there is still a strong temperature bias, even though the material is put through extensive calibration by Advanced Navigation. It will be imperative to always consider and correct the temperature bias. On the other hand, looking at the recorded barometric pressure for the duration of this experiment, I don't notice any influence of the pressure changes, especially during the second half of the experiment, on the accelerations recorded.

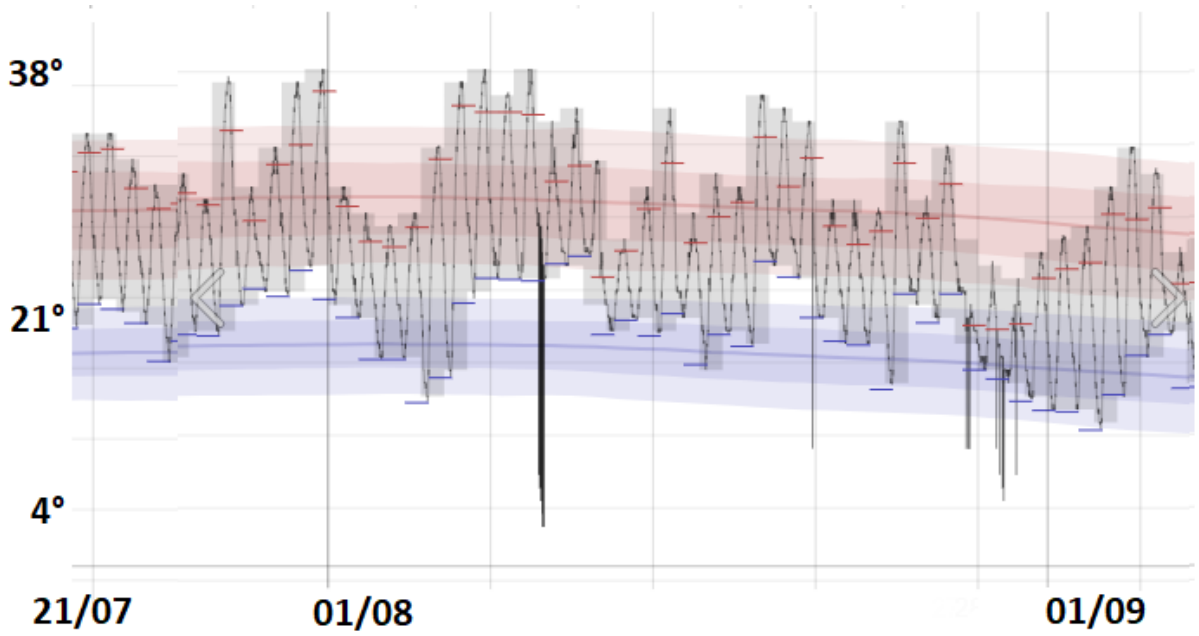

Fig. 3.13 Temperature at Toulouse for the period of the experiment (21/07/2020 - 06/09/2020) (Credit: Weatherspark.com)

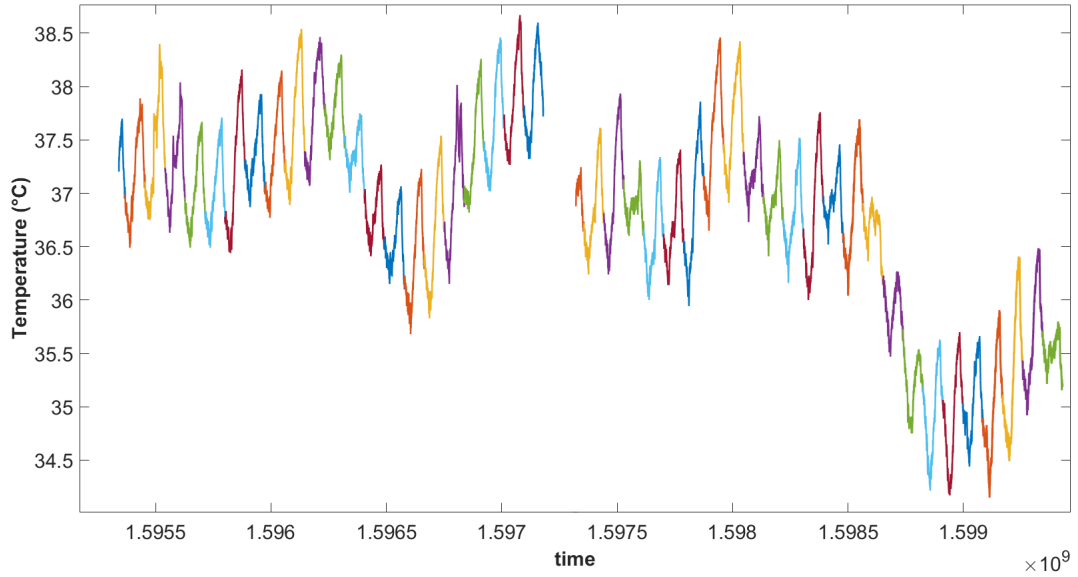

Fig. 3.14 Internal temperature measured by the INS/GNSS for the period of the experiment (21/07/2020 - 06/09/2020)

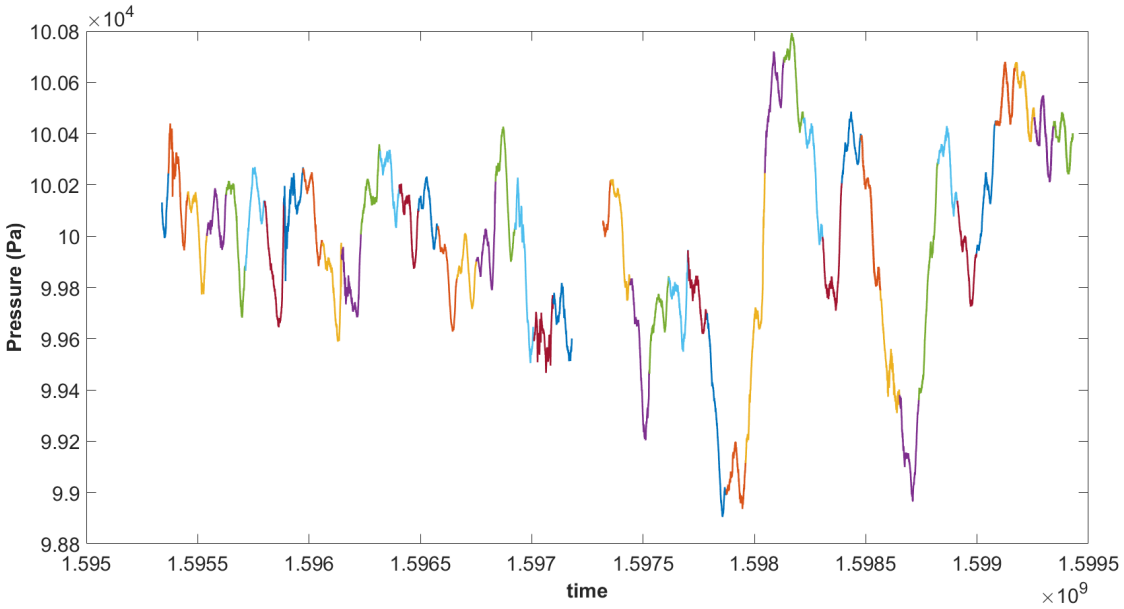

Fig. 3.15 Pressure from 21/07/2020 - 06/09/2020 for different frequencies.

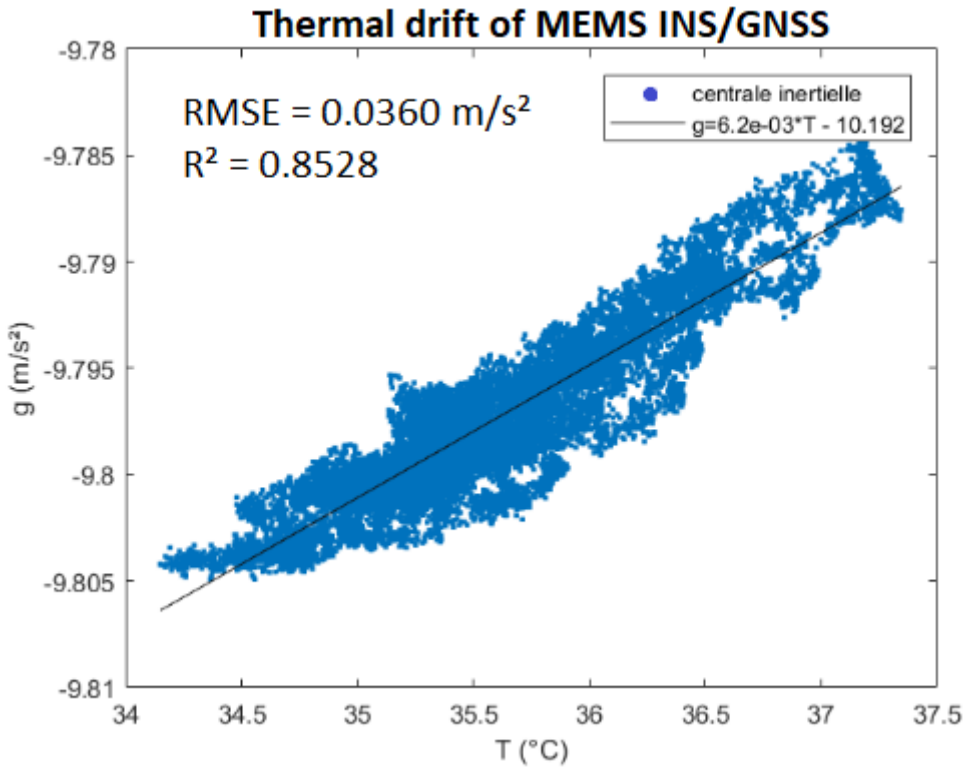

Fig. 3.16 Temperature (°C) plotted against measured down acceleration (m/s²) and the associated linear law.

In order to quantify the thermal drift of this instrument I plot all the values of acceleration (DOWN) against the recorded temperature of each point. Figure 3.16 shows a clear linear correlation between the temperature and the data recorded by the accelerometers. The variance between values for a single temperature is because this data includes all accelerometric data for the period of 21/07/2020-06/09/2020, which means it also includes the data at high sampling frequency which contained more noise than at a lower sampling frequency where the values were averaged out. This graph directly shows the influence of different temperatures on the sensors and the measurements they take.

With this linear relation between the temperature and acceleration, this drift is then corrected on the acceleration data from 21/07/2020 - 06/09/2020 (Fig. 3.17).

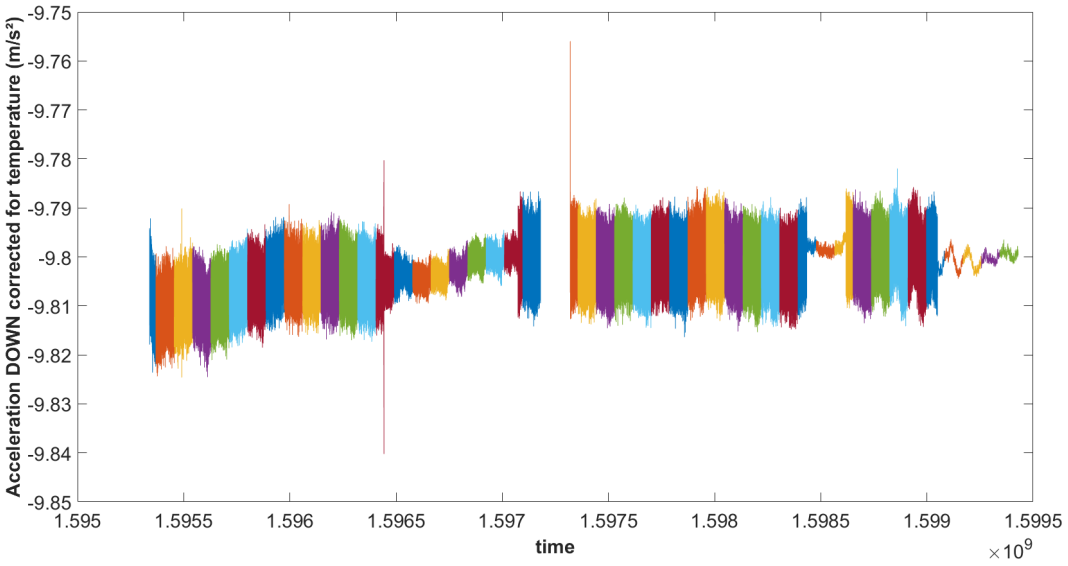

Fig. 3.17 The acceleration along the down axis, recorded from 21/07/2020 - 06/09/2020 for different frequencies, corrected for temperature.

3.3 Study at high temperatures

The technical characteristics of the INS/GNSS suggest that it can be used in extreme temperature conditions (manufacturer's data: between -40 and 85°C). However, I know that behavior at very high or very low temperatures can change, so it's important to see whether the temperature dependency remains linear, and if not, what is the temperature range in which our calibration will be valid. To do this, I used a laboratory drying oven where a Spatial INS/GNSS was enclosed. With an ambient temperature of 33°C this would be the starting temperature. During the morning I would slowly raise the temperature inside the drying oven up to 45°C over a period of 3 hours, but because the INS/GNSS gives the temperature inside the INS/GNSS it records a value of around 48°C due to the heating of the electrical components. In the afternoon I would start the oven at 40°C, raise it to 50°C before turning it off and letting the oven and INS/GNSS cool down (Fig. 3.18). What I learned from this experiment is that the temperature bias does not follow a linear law for every temperature range. At the temperature of 48°C, the increase in temperature will have the opposite effect on the accelerometric recordings. When the oven is turned off and the INS/GNSS cools down, it will follow the same law it did during the heating up period but backwards.

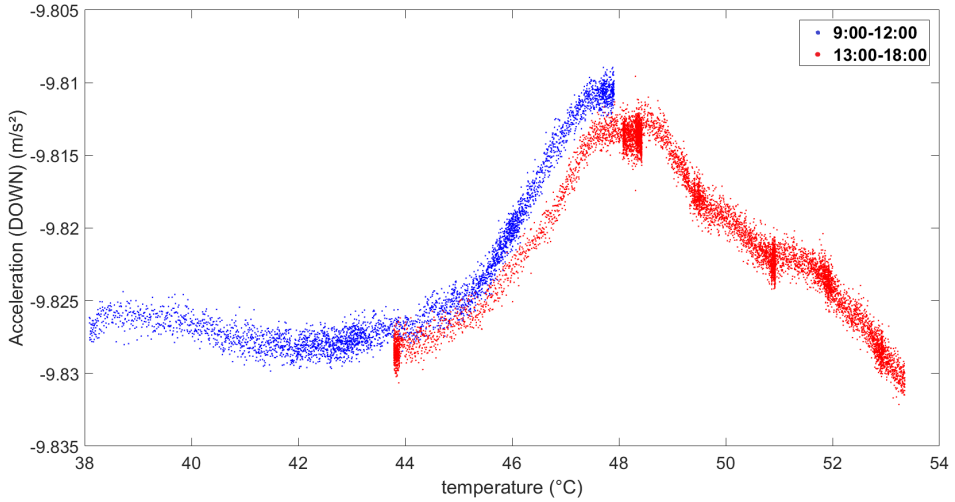

Fig. 3.18 Accelerometric data (DOWN) recorded by the INS inside a drying oven for different temperatures during the morning (heating up) and afternoon (heating up and cooling down).

Luckily this model's temperature bias follows a linear law for the realistic temperature range (20-30°C, seen earlier) when I will use it for practical applications in the field. Because this nonlinear law at higher temperatures would make it much harder to apply a correction.

At the time of this experiment using a drying oven, I had received a second instrument from Advanced Navigation to work with. This was the IMU model named MOTUS. During the experiment using the drying oven I had placed it next to the SPATIAL, recording at the same rate. From the image below (Fig. 3.19), it's clear that this IMU has no clear thermal drift compared to the INS/GNSS.

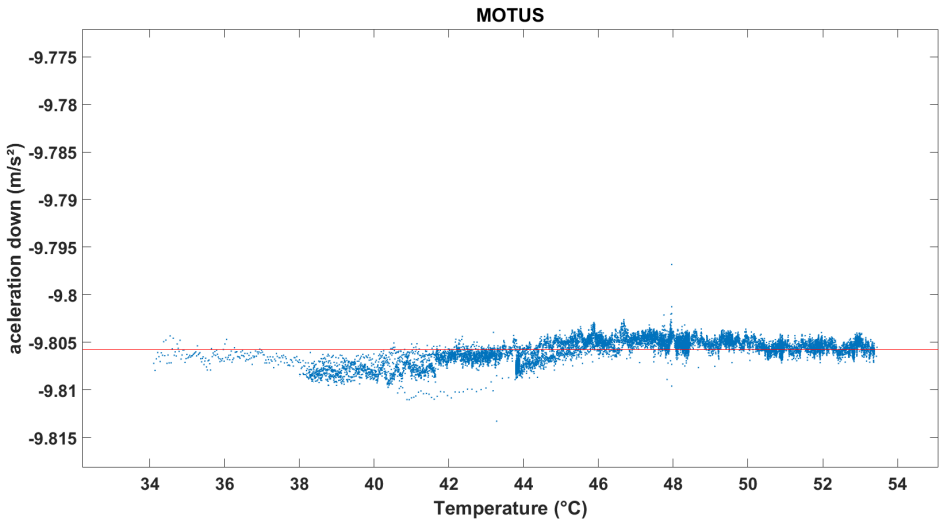

Fig. 3.19 Accelerometric data (DOWN) recorded by the IMU inside a drying oven for different temperatures ranging from 33°C to 54°C

3.4 In situ experiment with small altitude variations

From the period of early may to early june, another in situ experiment at the GET laboratory was performed. For this experiment, 2 SPATIAL INS/GNSS, 2 MOTUS IMU and 1 CG5-gravimeter were used. One SPATIAL and MOTUS, together with the gravimeter, would be placed in a room on the ground floor. The other SPATIAL and MOTUS were placed on the roof, protected from wind and rain. Throughout the 2 month period, I would swap the places of the instruments every few days. The difference in height, 6.7 meters, would cause a small change in gravity (~2 mGal), so the goal is to see if the SPATIAL, MOTUS and gravimeter will detect it when they change places.

The first data I'll look at is the gravimeter as this will present the most accurate data, presented on the graph below (Fig. 3.20). The gravity data here is relative, which isn't an issue because what's of interest to us is the difference in gravity rather than the absolute value. This relative gravimeter was calibrated to record a value of 0 mGal when the local gravity is 975300 mGal (or 9.753 m/s²). The value recorded (approximately 5162 mGal) is the difference from that calibrated value, so when the gravimeter records 5162 mGal, this means the local gravity at the laboratory (ground floor) is 975300+5162, 980462 mGal (9.80462 m/s²).

I've presented both the raw data (blue), which clearly presents a linear daily drift, and the data after correction of this drift (red). From the 29th of April until the 3rd of May the gravimeter was placed on the roof, from the 3rd of May until the 10th of May it was placed on the ground floor, and then from the 10th of May until the end of the experiment it was placed on the roof again. I can clearly notice when these changes happen looking at the jumps in data. The change in gravity is 2mGal. If I consider this a free-air anomaly, I would deduce the height difference to be $\frac{2\ mGal}{0.3085\ mGal/m} = 6.5$ meters. On this data I can also notice a periodic wave signal with an amplitude of 0.1 mGal. This signal is caused by the solid Earth tides (semidiurnal and diurnal signal) and corresponds to the amplitude obtained using Tsoft in order to obtain the theoretical model, which will be talked about more in depth in the next chapter.

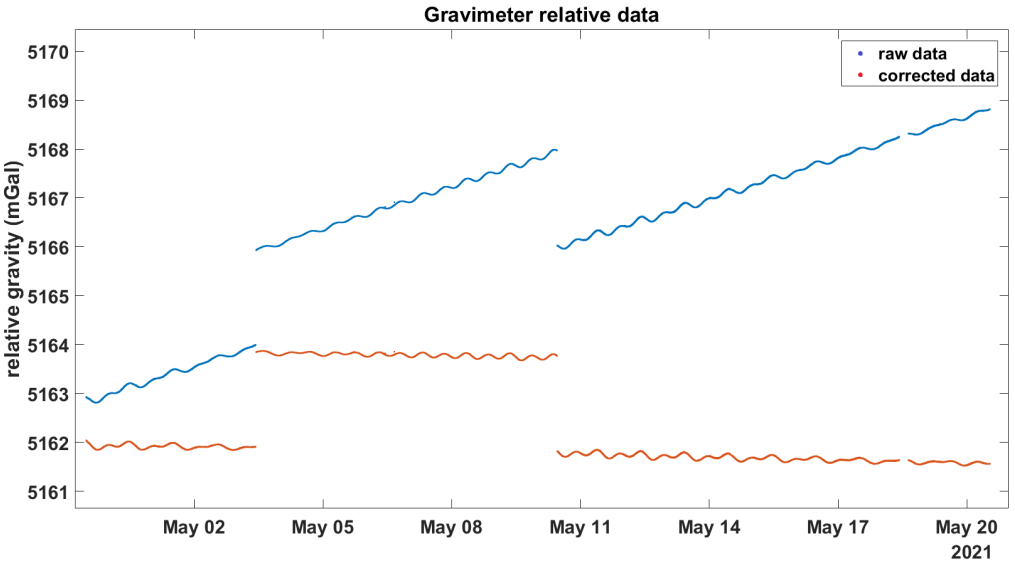

Fig. 3.20 Raw and corrected gravity data from the CG5-gravimeter, first placed on the roof, then ground floor and to finish on the roof again.

The next stage of the experiment involved two SPATIAL (INS/GNSS) and two MOTUS (IMU) which were moved at higher frequencies than the gravimeter, which needs to be stabilized after each movement. SPATIAL 1 was first placed on the roof, while the second one, SPATIAL 2 was placed on the ground floor of the GET laboratory. For starters I see that both SPATIAL are not calibrated at the same value for *g,* which is normal because they act as a relative gravimeter in this case. The units must be calibrated with an absolute gravimeter to obtain absolute measurements. On Fig. 3.21 I observe a clear jump in the data every time they were moved, however this jump has higher amplitude than what would be caused just by the altitude difference. What's more, they react in a similar way, not in opposition as should be the case i.e. stronger acceleration when one is placed on the ground floor and when the second one is placed on the roof, which theoretically results in a decrease in gravity as I move further away from the source. SPATIAL 1 & 2 also react in the same way even though they are in opposite positions, which is explained by Fig. 3.23 where we learn these two models react in opposite way to temperature variations.

This is because the jumps of data are not only to the altitude difference, but rather, to the first order, by a strong temperature difference. The instruments placed in the

room on the ground floor, would be subject to a lower temperature, due to the building's air-conditioning, than the ones on the roof which is outdoors and subject to solar radiation.

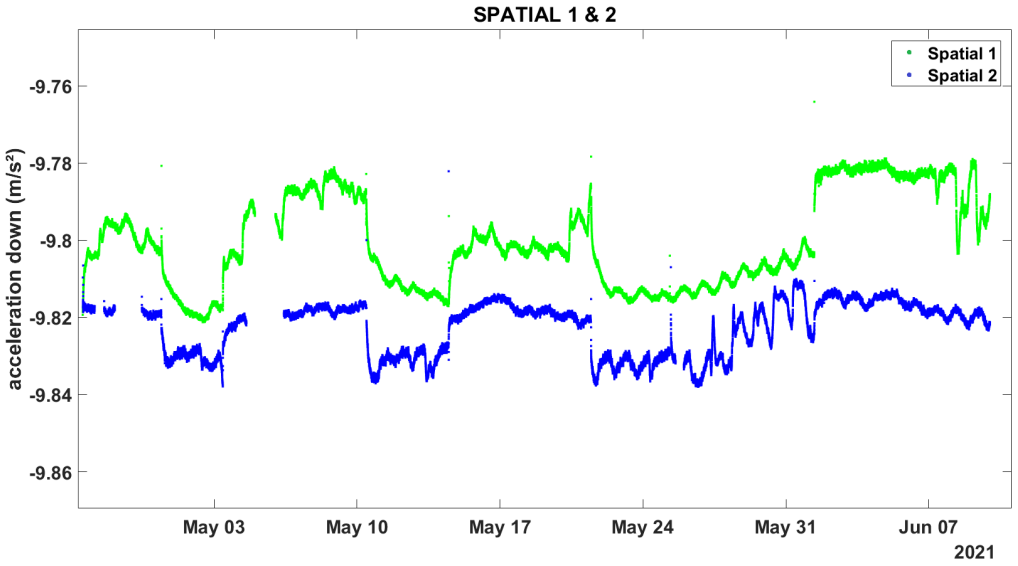

Fig. 3.21 Down acceleration data from SPATIAL 1 & 2 for the whole duration of the experiment

Figure 3.22, which represents the internal temperature of both instruments, shows more clearly these jumps. I can see when their positions are changed because of the jumps in temperature, which coincide with the jumps in acceleration data.

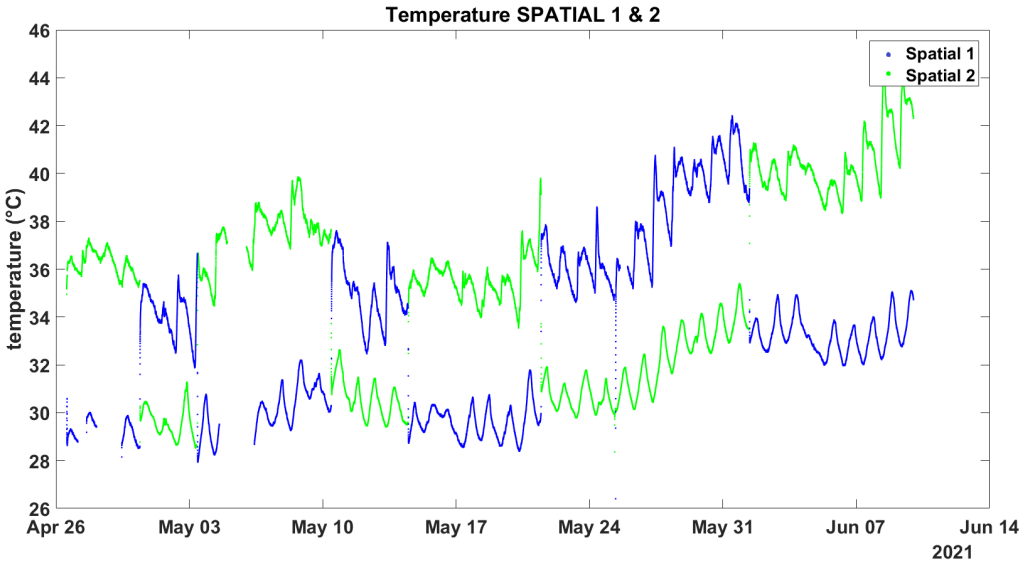

Fig. 3.22 Evolution of temperature of SPATIAL 1 & 2 over the duration of the experiment. Higher temperatures are recorded on the roof (outside) when the ground floor INS have lower ones.

On figure 3.23 is the plot of the acceleration against the recorded temperatures. SPATIAL 1 is the same instrument that was used for the first study of the influence of the temperature, and I can see the same rough linear law for the temperature range of 30°C to 38°C. On the other hand I observe that two SPATIALs react in opposite ways to the changes in temperature. When the SPATIAL 2 has its internal temperature increase, which increases the acceleration until 38° and decreases for upper temperatures. Conversely, for SPATIAL 1, when the temperature rises to 40°C, the acceleration decreases in amplitude from g=9.82m/s^2 until 9.78m/s^2. After that it increases from 9.78 until 9.81m/s^2.

This is why on the graph containing the acceleration data both instruments would react in the same way when they in fact had opposite positions (so opposite temperature changes).

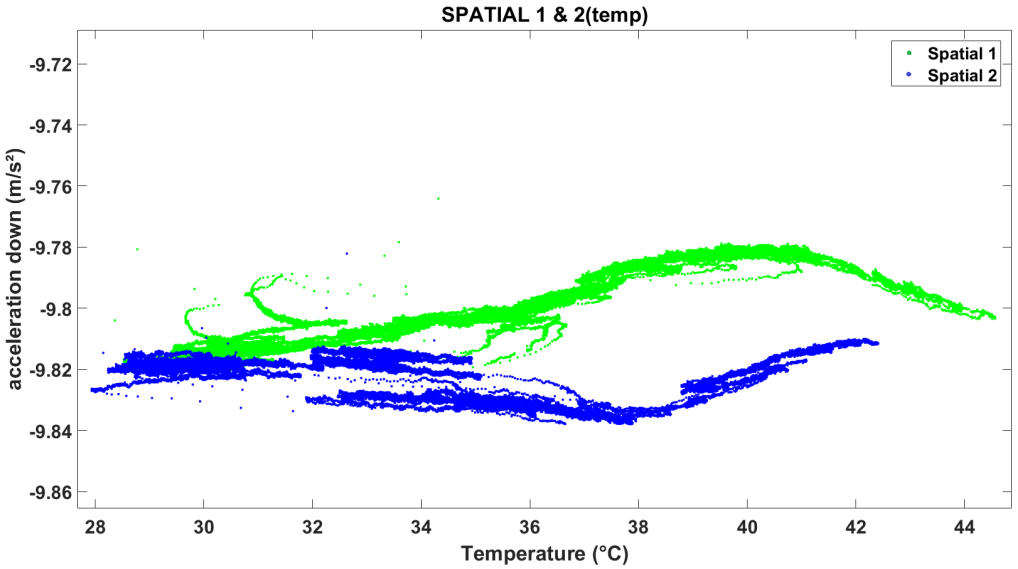

Fig. 3.23 Down acceleration of the SPATIAL 1 & 2 plotted against the recorded temperature. Two instruments of the same model not reacting in the same way to temperature variations.

During the first study of the thermal drift of SPATIAL 1, I could use the linear law found to correct the raw data, as the SPATIAL was never moved. However for this experiment that is not possible as there would be two factors changing; the altitude and the temperature. Without knowing the exact influence of one, I can't correct the other.

Earlier I also showed that the MOTUS IMU has no thermal drift for the range of 35°C to 50°C. This means, unlike the SPATIAL, for this experiment the only thing to influence the acceleration data will be the altitude variations between the two locations (roof and ground floor). Figures 3.24 and 3.25 show the acceleration data of the MOTUS 2 and 1 respectively, the vertical lines denote when the IMU were moved, “down” means it was placed on the ground floor, “up” means it was placed on the roof. The horizontal lines present the average value of the data for each period at a different location. Due to technical issues a lot of data from MOTUS 1 during the first days was lost, I also used a much higher sampling frequency for MOTUS 1 to test what would give the best results. In hindsight this was unnecessary, while more data is obtained, there is also more noise present, which I would have to filter out.

MOTUS 2 was first placed on the ground floor, which would result in a stronger down acceleration recorded. Figure 3.24 shows a weaker acceleration when moved up.

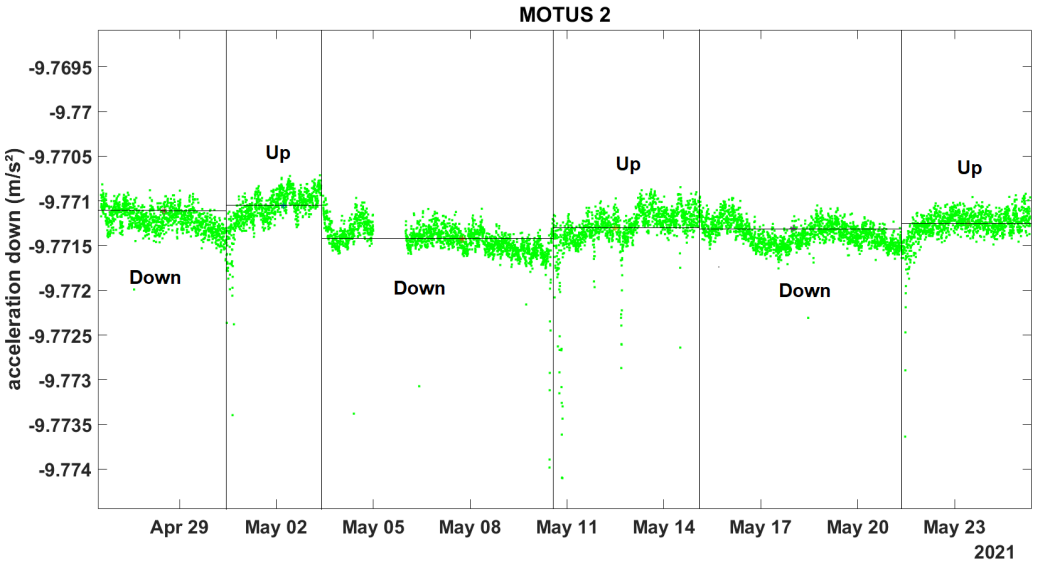

Fig. 3.24 Down acceleration recorded by the IMU MOTUS 2, vertical lines represent when the instrument changed positions. (Up; roof / Down; ground floor). The horizontal lines are set to the average value of the data for each period.

Position	Acceleration (m/s²)	Δg (mGal)
Down	-9.77111	/
Up	-9.77105	5.87
Down	-9.77143	-37.6

Up	-9.77130	12.1
Down	-9.77131	-1.02
Up	-9.77125	5.73

Table 3.2 - Average value of the down acceleration of the MOTUS 2 for each position/period and the difference in gravity compared to the previous ones.

The raw data is presented in table 3.2. When the IMU is moved from the down position to the up position Δg is positive because the gravity decreased, when moved from the roof to the ground floor conversely Δg is negative because the gravity increased.

The CG-5 corrected data presented a difference of 2 mGal between the ground floor and the roof, which is consistent with the change in altitude observed. By looking at the difference in gravity, between the average values of each location, I obtained results that are of the same order. There is only one period (starting on May 5, Fig. 3.24), when the instrument was in the down position for the second time, that shows a large difference in terms of gravity that is not coherent with the other results. This is also the period where due to some technical issues some data was lost, which could be an explanation for this abnormal result.

I will now take a look at the measurements obtained with the MOTUS 1 (Fig. 3.25), which was first placed on the roof. I can see the same pattern again, whenever the position changes the average value of the acceleration changes, with a stronger gravity in the down position. This instrument was set to a higher sampling frequency, which is noticeable from the increase in noise compared to the data from MOTUS 2 and more aberrant data points, especially during the period of the 21st of May until the 1st of June and to a lesser extend during the period of 11th of May until 14th of May. More data was lost due to technical issues during the first roof measurements. However even for the last four periods of data, the difference between the average values is much higher than what was obtained using MOTUS 2 and does not have the mGal precision that is required to study the gravity changes due to a small altitude change (<10 meters). The higher sampling frequency is not suitable for a long period experiment to detect such a small gravity anomaly. For static experiments a very low sampling frequency can and should be used, however for

mobile experiments a trade-off will need to happen between a high enough frequency to record all movements of the moving platform, but not higher than needed or more noise will be included without any benefit.

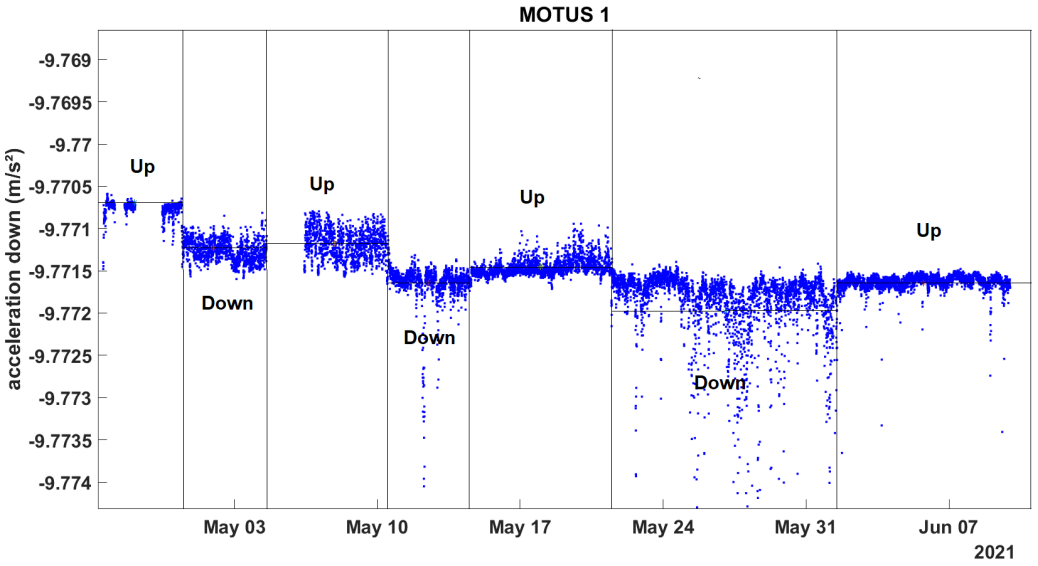

Fig. 3.25 Down acceleration recorded by the IMU MOTUS 1, vertical lines represent when the instrument changed positions. (Up; roof / Down; ground floor). The horizontal lines are set to the average value of the data for each period.

Position	Acceleration (m/s²)	Δg (mGal)
Up	-9.77069	/
Down	-9.77122	-53.0
Up	-9.77118	46.1
Down	-9.77164	-46.6
Up	-9.77145	19.0
Down	-9.77197	-52.4
Up	-9.77164	33.4

Table 3.3 - Average value of the down acceleration of the MOTUS 1 for each position/period and the difference in gravity compared to the previous ones.

CHAPTER 4 Study case: Using the INS/GNSS to detect earth tides

4.1 Scientific context

Because I acquired the data recorded by the INS/GNSS and a CG-5 microG LaCoste gravimeter over a period of multiple weeks at the laboratory during my first experiment using it, I could use this data for more than just studying its characteristics and the influence of other external factors.

The simplified image of Fig. 4.1 gives us an idea of the precision required to study different aspects of temporal and spatial variations of Earth's gravity field. The lowest gravity on the surface of Earth is 9.7639 m/s² and the highest is 9.8337 m/s², so the total change (on the surface) is less than 0.1 m/s². The standard gravity of 9.8 m/s² and the value of the first decimal has the value it has because of the size and mass of Earth. The influence of the other aspects on the precision are of course approximate and are there to give a general idea, for example the change in theoretical gravity at the equator and the poles generates a difference of 0.05 m/s², but a small change of 1° latitude will not change the second decimal value of gravity. For an in situ experiment at the laboratory it is impossible to have a change in latitude that would allow us to verify the precision of the instrument. The strongest natural phenomenon that would change the gravimetric measurements of this INS/GNSS at rest at the same location, over a period of multiple weeks, that could possibly be extracted from its data would be the solid Earth tides. That's why the data acquired during the first experiment were used to analyze the solid earth tides, which at our coordinates would have a maximum signal amplitude of approximately $1 * 10^{-5}$ m/s², or, 1mGal.

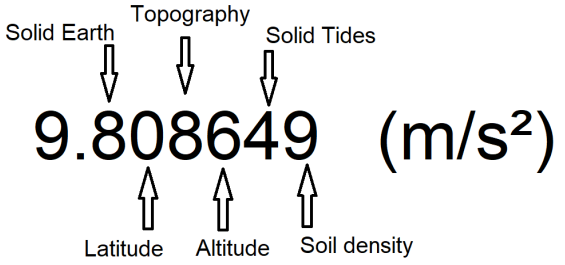

Fig. 4.1 Simplified presentation of required precision for different processes

4.2 Introduction of solid Earth tides

Ocean tides are the displacement of the Earth's water because of the gravitational pull of the moon and other celestial bodies. For instance the gravitational pull of the Sun also has an influence, but to a much lesser extent. Because the moon orbits around the Earth and the Earth itself rotates, the tides move around the Earth instead of staying in the same place. Even though the gravitational pull of Earth is so much bigger on all the water molecules on Earth, the reason of these tides is because all the water in the ocean is connected and can be seen as an unique liquid body where the sum of all these small displacements of water molecules add up to create a pressure that is big enough to be noticeable, even with the moon's gravitational pull being so much weaker than Earth's. High tides are located on the side where the moon is located because this is where the moon's gravitational pull will be strongest, but also on the opposite side on Earth, due to inertia, even though the moon's gravitational pull will be lowest here. This is why high and low tides happen (roughly) twice a day instead of only once. The principal lunar semidiurnal component is the largest constituent of tidal cycles and is known as the M2 tidal constituent.

The tidal cycle can be predicted with high precision but there are still atmospheric factors like pressure, temperature, wind, that will play a role in the maximum or minimum height of the tides that are much harder to predict.

Solid Earth tides is the Earth's crust displacement due to the same principle, the gravitational pull of the moon and Sun, just less noticeable because the crust is mostly solid so the elastic displacement will be lower than the ocean's water. If the crust had no elasticity there would be no displacement. Just like ocean tides, the solid tides' main component will be semidiurnal and diurnal. There is also a fortnightly cycle (~14 days) because the moon orbits around the Earth in a period of 27 days. When the moon, Earth and the sun are aligned (new or full moon), the ocean and solid tides are higher because the amplitude changes due to each celestial body are added together creating bigger bulges and depressions. When the

moon, Earth and Sun are at a right/perpendicular angle the amplitude of tides will be at a minimum because the bulges and amplitudes are opposite and partially cancel out. Just like the ocean tides, the cycle of solid tides can be predicted, but there are also factors that will influence the amplitude variations, for example in coastal regions, the weight displacement from the water from ocean tides can push down on the crust (known as ocean loading), reducing the height difference of the solid tides.

4.3 Theoretical tides compared with raw data of the first experiment

I used the software "Tsoft" to obtain the model of the synthetic solid tides at the coordinates of the GET laboratory. Tsoft was developed by Van Camp, M., and Vauterin (Royal observatory of Belgium). These synthetic tides, obtained from a theoretical Earth model (Wahr Dehant Defraigne 1999), do not take into account the effect of the ocean load.

For the period of the 3^{rd} of September until the 15^{th} of September, the INS/GNSS was recording uninterruptedly at the same sampling frequency of 0.0167Hz (1 measurement every 60 seconds). I'll be comparing this data with that of the synthetic tides obtained from the Tsoft model, to avoid any ambiguity in the results due to different sampling frequencies being used together. This will also allow for an easier presentation of the wavelet coherence and won't require the need for any interpolation. The reason for such a low sampling frequency is twofold. The CG-5 gravimeter was using the same sampling frequency (1 measurement every minute) and to observe the effect of solid Earth tides there is no need for a high sampling frequency because the main components are semidiurnal and diurnal, on top of that we've seen that with a higher sampling frequency there will be an increase in noise.

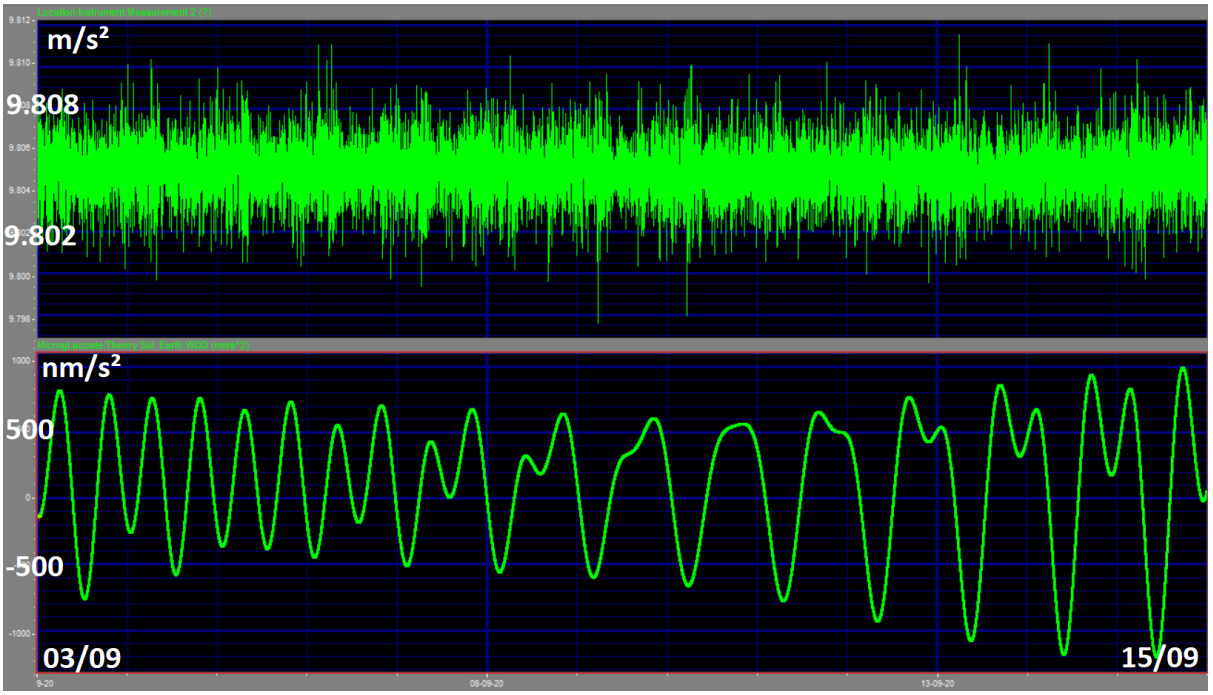

Fig. 4.2 Tsoft software with the acceleration (down) data & synthetic solid tide for the period of 03/09/2020-15/09/2020.

Figure 4.2 presents the absolute value of the accelerometric data of the z-axis (pointing down) and the modeled gravity data due to the solid Earth tides for the period of 3/09/2020-15/09/2020. This data over a two week period nicely shows the effect of the Moon's position and the effect on the solid tides. On the 3^{rd} of September 2020 the moon is 98% illuminated (1 day after Full Moon) which shows from the semidiurnal solid tides. On the opposite side, on the 15^{th} of September the Moon is 5% illuminated, 2 days before New Moon I see the same semidiurnal cycle appearing, however the amplitude is higher because the Moon is positioned between the Earth and Sun, so the gravitational pull of both celestial bodies is pulling in the same direction. Unlike the first part where the Earth is positioned between the Moon and Sun, where the gravitational pull is pulling in opposite directions, reducing the total gravitational pull and thus reducing the amplitude of the solid tides. For the middle part of this period the Sun and Moon's position are at (or close to) a 90° angle, so their gravitational pulls are counteracting the effects of one another, which is why the amplitude is lowest for this period.

4.4 Cross wavelet coherence for the periodicity of solid Earth tides

Looking at the accelerometric data, which was corrected for the temperature bias using the previously established linear law, it is impossible to notice periodic signals using the naked eye. For this reason I took the continuous wavelet transform (CWT) of both signals.

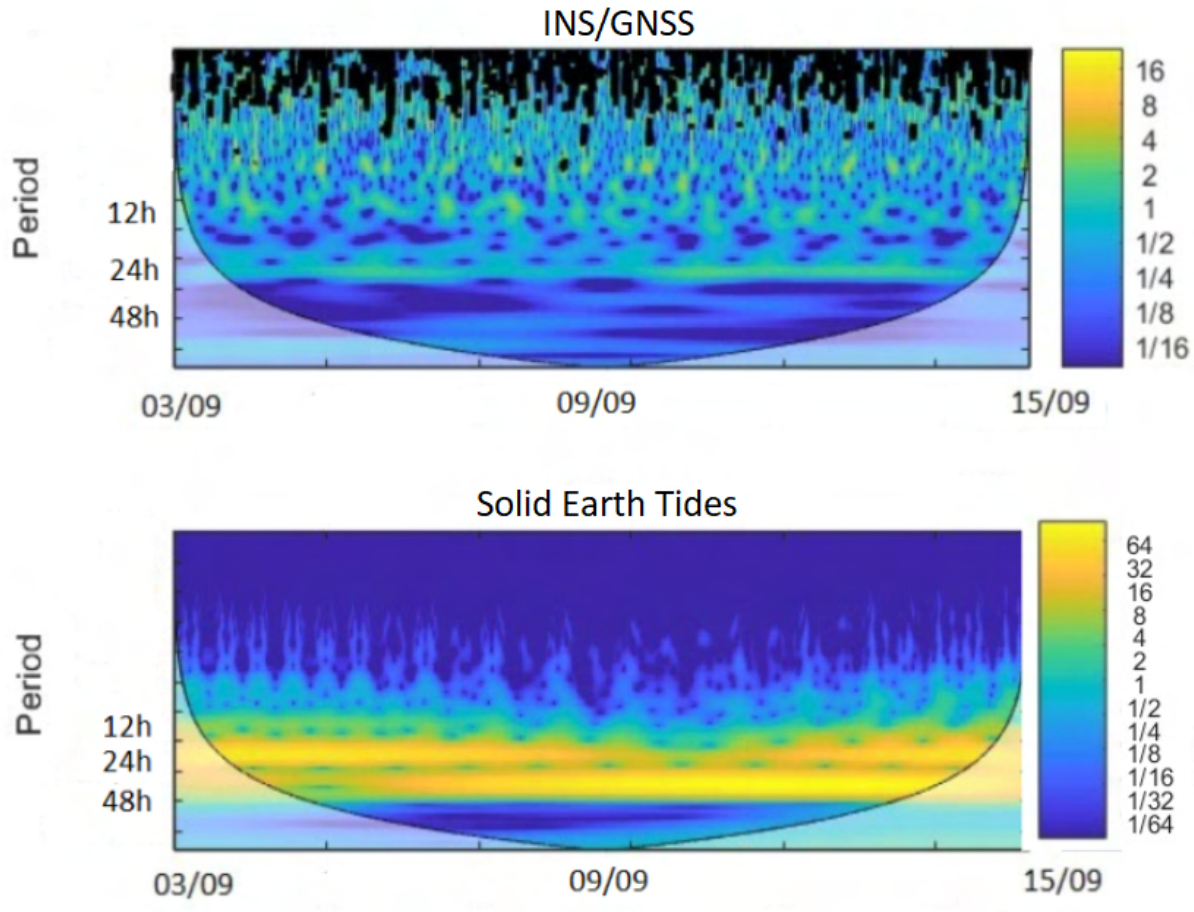

Fig. 4.3 CWT of INS/GNSS (top) and theoretical tide (Tsoft) data (bottom)

At the top of figure 4.3 is the CWT of the INS/GNSS data. Easily recognized by its high noise for low periods. I notice a clearer periodic signal around the period of 24 hours.

The bottom part is the CWT of the signal obtained with Tsoft for the synthetic solid tides. This theoretical signal of course shows no noise for the short periods and a clear signal for the periods between 12 and 48 hours.

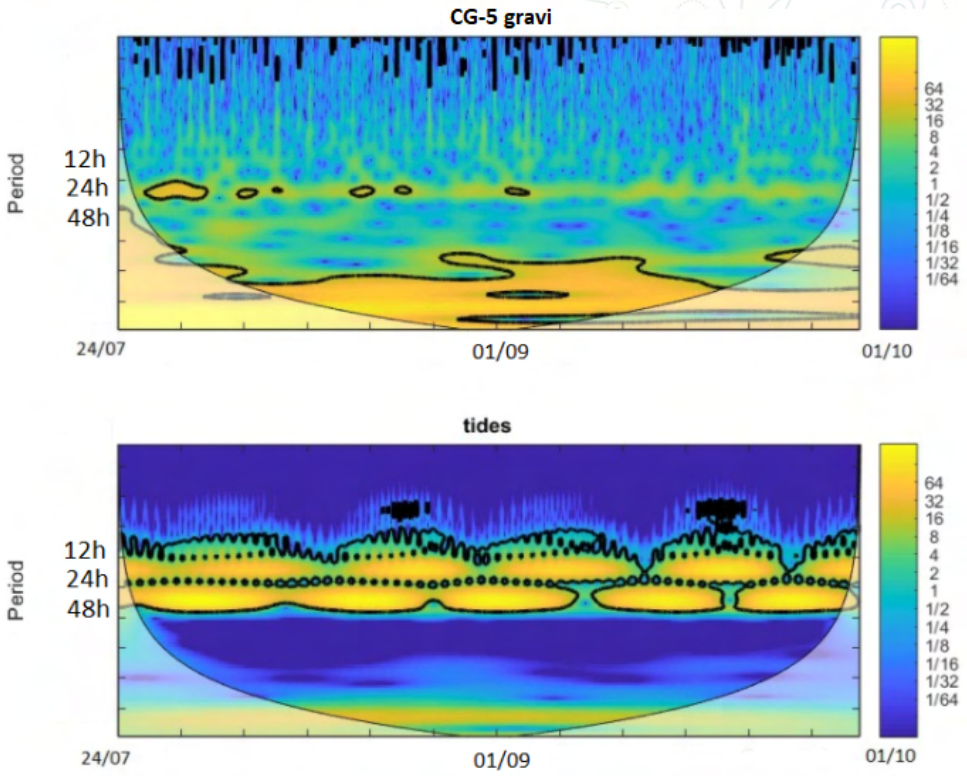

Fig. 4.4 CWT of CG-5 (top) and theoretical tide (Tsoft) data (bottom)

The same wavelet analysis was done using the CG-5 gravity data provided by the relative gravimeter which had been recording at a frequency of 0.0167Hz (1 measurement every minute) since the 24^{th} of July 2020 until the 1^{st} of October 2020. The top part of figure 4.4 shows a clearer periodic signal for the period of 24 hours compared to that of the INS/GNSS (Fig. 4.3), which is normal due to the higher precision of this instrument. I can also notice strong coefficients for the long-term periods of fourteen days.

For the explanation I also need to look at the CWT of the synthetic tide signal (Fig. 4.4, bottom part) where I also notice a signal for this same long-term period. This period corresponds to approximately 14 days, which corresponds to the fortnightly period of the moon (theoretically 13.6 days).

Looking at the cross wavelet transform (XWT, figure 4.5) I can see the coherence between the signals of the INS/GNSS and CG-5 with that of the theoretical solid tides.

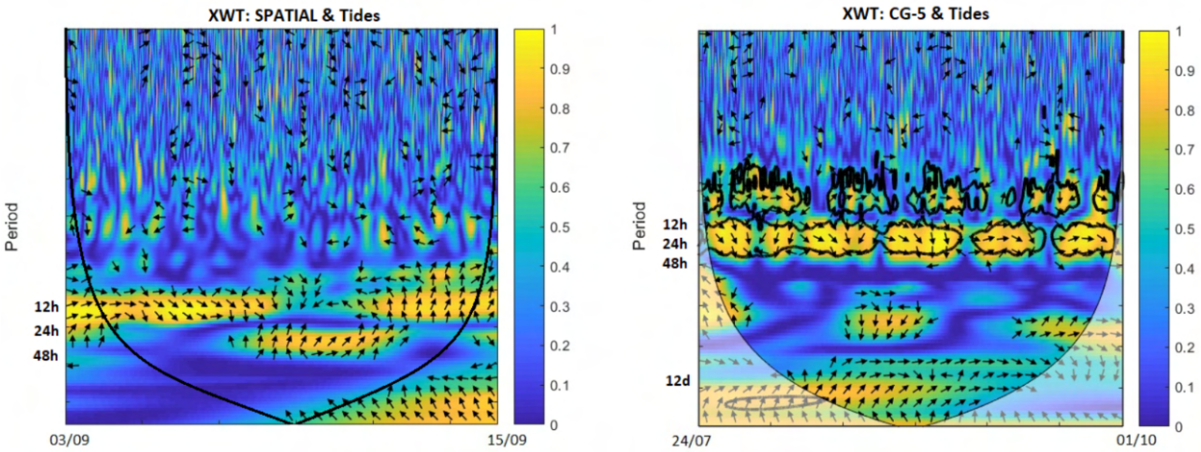

Fig. 4.5 XWT of INS/GNSS & Tsoft data (left) and CG-5 & Tsoft data (right). Arrows represent the phase delay between both signals (pointing right: in phase; up/down: out of phase, pointing left: opposition of phase)

I can indeed see for both instruments (INS/GNSS and CG-5) there is a coherence with the theoretical solid tides for the periods of 12-24 hours, and the period of 13-14 days for the CG-5 corresponding to the lunar fortnightly, which can not be seen for the INS/GNSS since the duration of the recording was only 13 days. I also notice the signals are mostly in-phase (arrows pointing right) at the start, and out of phase in the middle and end. One possible explanation for the signal being out of phase at some point is because we're comparing it to a theoretical model which also doesn't include the effect of the ocean load. This ocean load is able to slightly delay or change the amplitude of the actual solid tides, which are the ones that are measured by our instruments, compared to the theoretical solid Earth tides modeled by the software.

The upper half of both images (fig. 4.5) shows no correlation of course as there was no short-term period in the signal of the solid tides and the INS/GNSS and CG-5 would only record noise for those short periods (< 3h).

This result is very important because it shows for the first time the INS/GNSS presents the periodic signals corresponding to that of the solid Earth tides, which only has a maximum amplitude difference, at this location, of 0.2mGal for this period. However this was from data obtained while the INS/GNSS is not moving but where

mechanical vibrations (e.g. air-conditioning) and external factors (man-made effects: moving cars, people walking, etc.) add noise that needs to be filtered.

If I filter both the INS/GNSS and Tsoft data to remove all the periods of 10 hours and below (which would not remove the fundamental periods related to the solid Earth tides) and reconstruct our signal with the remaining frequencies, convert the INS/GNSS data to nm/s² and remove the offset of ~9.8m/s², I obtain the two signals presented on the top half of figure 4.6 which show a good correlation (0.84) and where I can also notice the dephasing in the middle and the end (RMSE: 405nm/s²) . I also observe two periods where there is a larger amplitude difference between both signals, one possible factor that causes this could be a change in atmospheric pressure. The bottom half of figure 4.6 represents the atmospheric pressure for this period, where I can see a lower pressure that lines up with the same periods of the amplitude differences.

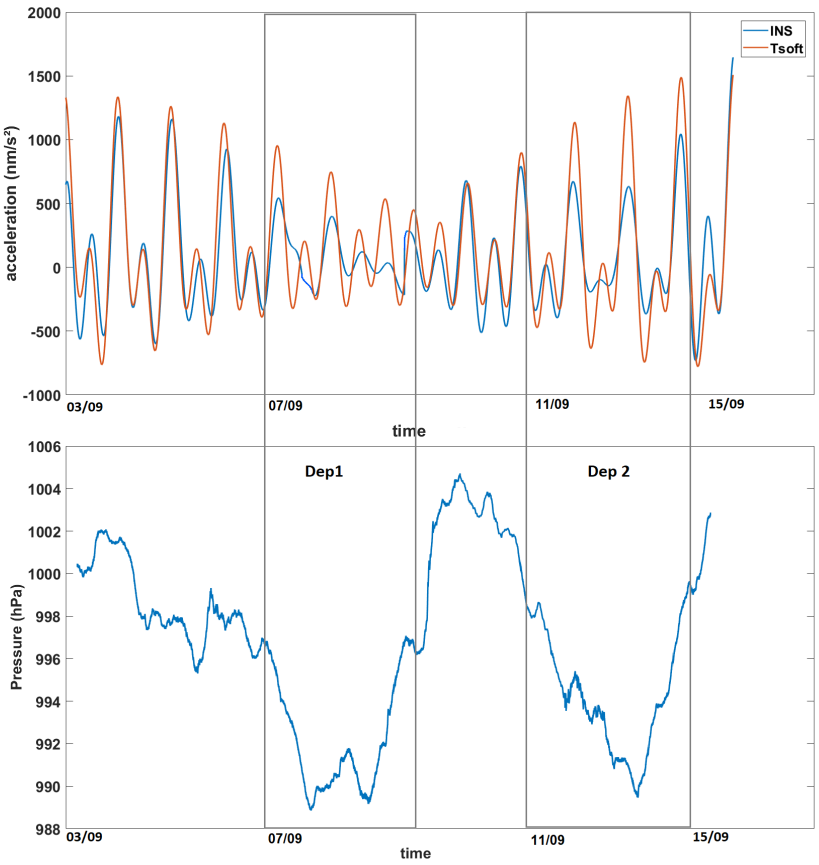

Fig. 4.6 Top: Reconstructed signals of INS/GNSS and Tsoft after filtering at 10 hours, removing the offset from the INS/GNSS data and converting to nm/s². Bottom: Atmospheric pressure recorded by the INS/GNSS for the same period.

The graph below (Fig. 4.7) shows the frequencies corresponding to the periods of 12 hours and higher, and I can clearly see strong amplitudes in both signals for the periods of 12 and 24 hours, just as I saw on the wavelet coherence.

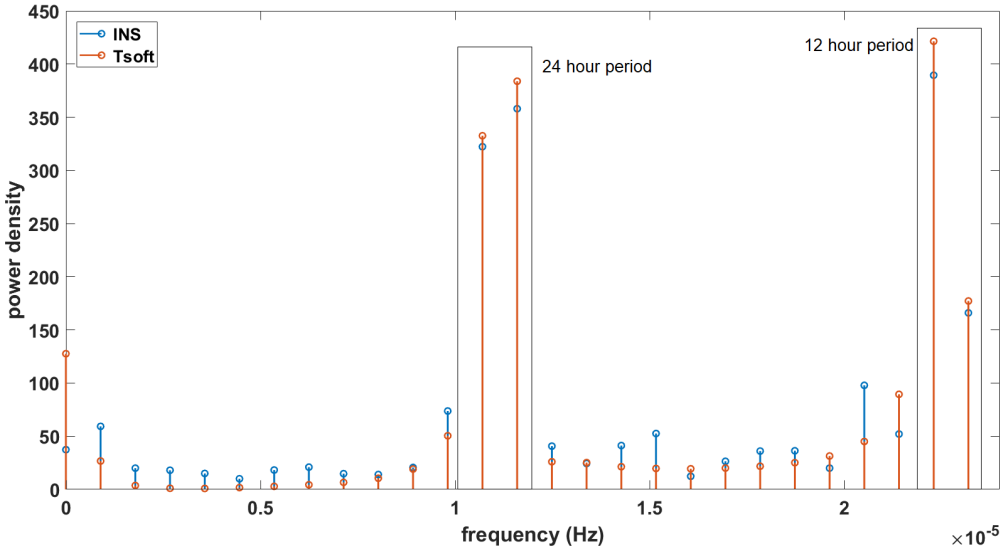

Fig. 4.7 Frequency domain of INS/GNSS and Tsoft data for the periods of 12 hours and higher

If I only consider the two peaks in the middle corresponding to the frequencies for the periods of ~24 hours and reconstruct them, I obtain the signals presented on figure 4.8. Because of the high correlation at those frequencies, the constructed signals will of course also be correlated, however since no other frequencies besides those two are considered, the signals will now be almost perfectly in phase. I can also see now that the INS has a lower amplitude than the signals obtained from Tsoft. This is either because of the previously mentioned ocean load which can dampen the amplitudes of the solid Earth tides, the atmospheric pressure or simply because the INS/GNSS is not accurate enough to measure the full amplitudes.

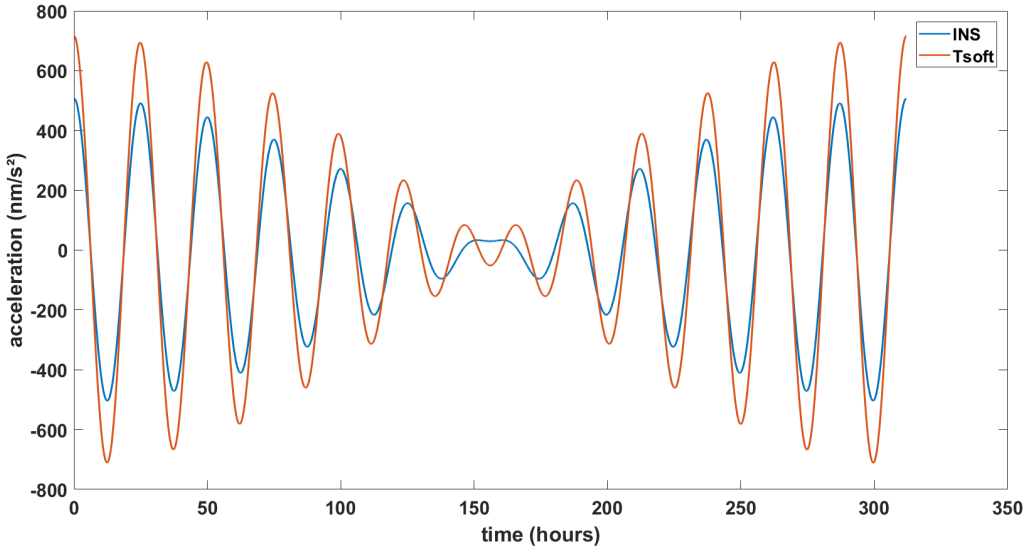

Fig. 4.8 Reconstructed signals of INS/GNSS and Tsoft data when only keep the periods of ~24 hours

Similarly if I only consider the peaks on the left (~12 hour periods) I obtain the semidiurnal signal seen on figure 4.9, where the INS signal also has a lower amplitude than the Tsoft data.

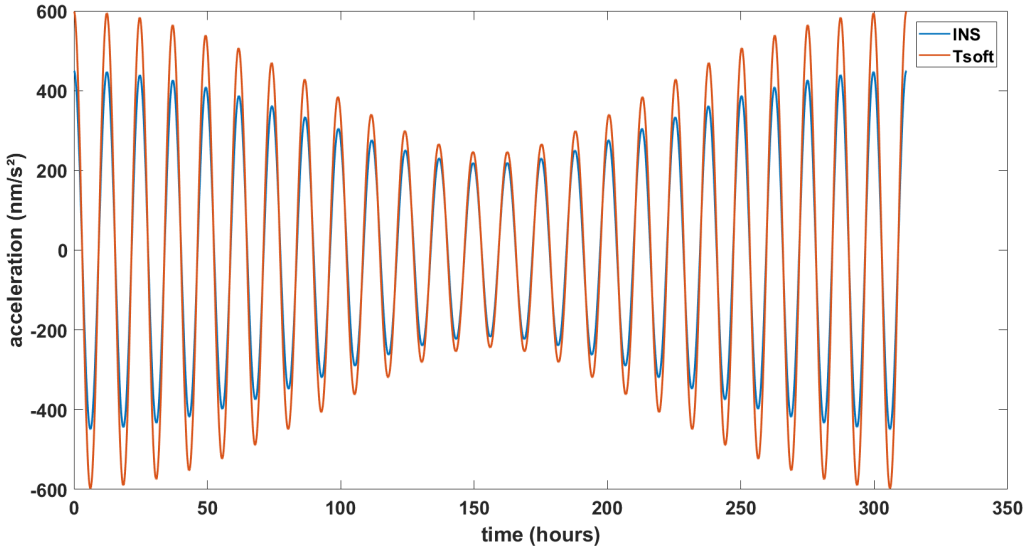

Fig. 4.9 Reconstructed signals of INS/GNSS and Tsoft data when only keep the periods of ~12 hours

While the detection of the effect of solid Earth tides has been done using a MEMS gravimeter, this is the first scenario of a MEMS INS achieving a similar result. While the precision is definitely less good than a MEMS gravimeter, the conclusion remains that the instrument we used was able to detect them as well. For future studies, unless the budget of the project is a big constraint, I do not recommend using this

instrument if the goal is only to detect the solid Earth tides, in which case I would always recommend a gravimeter. For my PhD the main goal was to test the precision of the instrument and possible ways to filter and correct the data.

CHAPTER 5 Study case: Using the INS/GNSS for mobile gravimetry

5.1 Scientific context

Because I had shown the capability of this INS/GNSS model by observing the same periodic signal as that of the solid tides, the next step was to bring this instrument out in a moving platform.

For our first moving experiment and before trying to see solid tides as in the last static experiment, I need to see if I am capable of seeing more significant effects such as topography. Because in the mobile case, in addition to the measurement noise specific to the instrument, I am adding vibrations specific to the vehicle itself, which is a new noise that most certainly modifies the accuracy of the gravity measurement.

The altitudes presented are the elevations, also called orthometric height. In general the altitude recorded by the Advanced Navigations instruments is the height referenced to the WSG84 ellipsoid, the ellipsoid height. The geoid height at Toulouse is 49 meters so using the previously mentioned formula, the orthometric height can be calculated.

5.2 Methodology of the experiment

The following steps were done every time the INS/GNSS (and IMU) were used for mobile gravimetry with a vehicle.
The INS/GNSS would be securely attached inside the vehicle as close to its inertial center as possible, with the x-axis pointing to the front of the vehicle and the z-axis pointing down (Fig. 5.1). It would be attached to a rubber support to try and absorb vibrations. In the van the system was also placed in a box for protection purposes

and to prevent dust from entering. I make sure not to obstruct the vents to prevent overheating. The GNSS receiver, with a magnetic base, would also be attached to the outside of the van and connected to the instrument and the offset between them measured. The instrument would be connected to a computer using the provided USB cables and the Spatial Manager software launched. Using the software I enter the packets I want to receive, the packet rates, the offset I measured and the vehicle type (for possible filtering options). Once this is done I close this software and open the program I modified in order to record to text files.

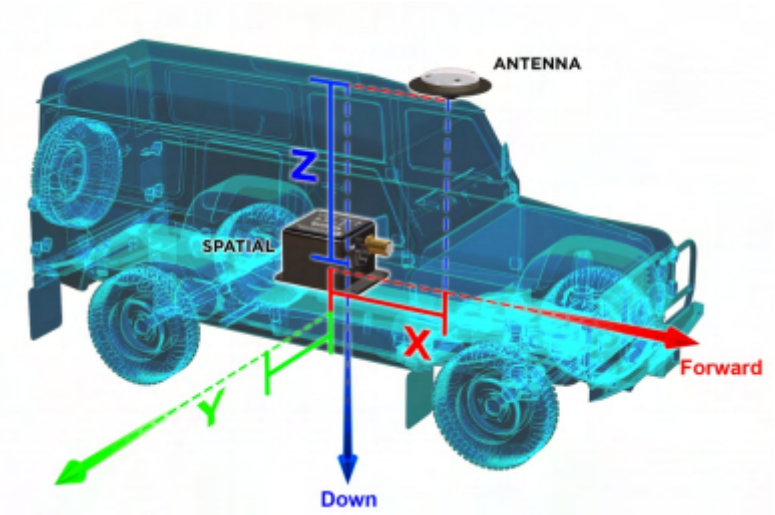

Fig. 5.1 Visual representation of the INS/GNSS attached inside a vehicle

We then proceeded to drive from the GET laboratory to the Cammazes dam, while making multiple stops to measure the gravity using a CG-5 gravimeter and the INS/GNSS. We stopped off at an IGN reference point where the IGN has established an absolute gravity measurement base, at Puylaurens (Fig. 5.2). Between the GET laboratory and the Cammazes dam (Fig. 5.2) there is an altitude difference of 400 meters (Fig. 5.3). The goal of this experiment would be to see if I can plot the accelerometric data of the INS/GNSS and see this change in gravimetric response due to the altitude. The CG-5 would be used as our reference, which would be calibrated at the IGN's absolute gravity reference point.

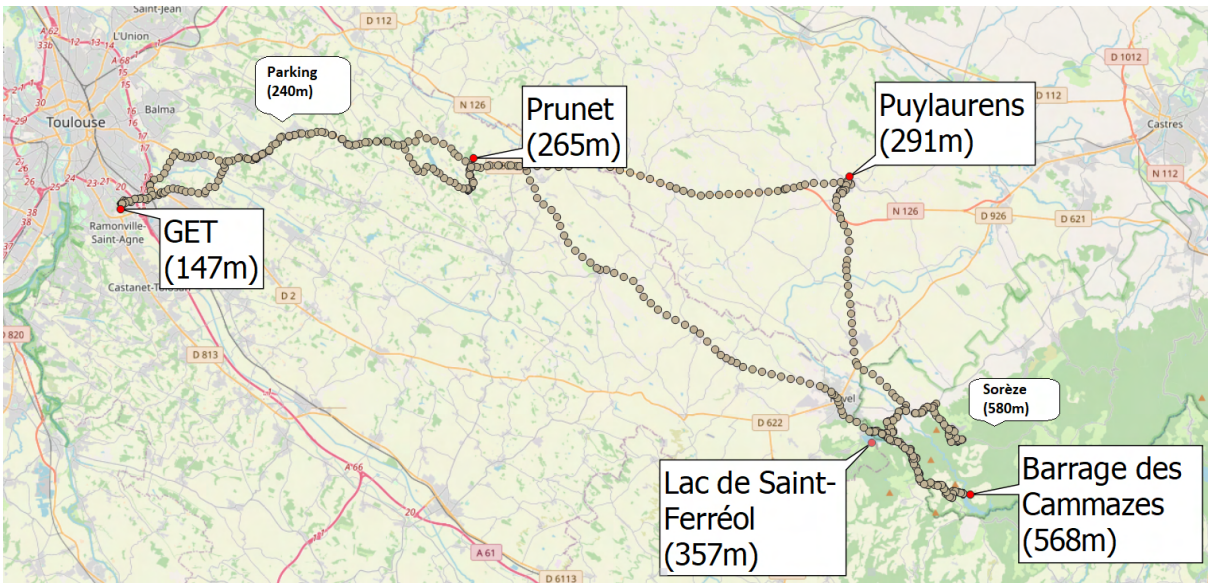

Fig. 5.2 Itinerary on the 18th of November 2020 from the GET laboratory to the Cammazes Dam and back with multiple stops on the way and the corresponding orthometric height.

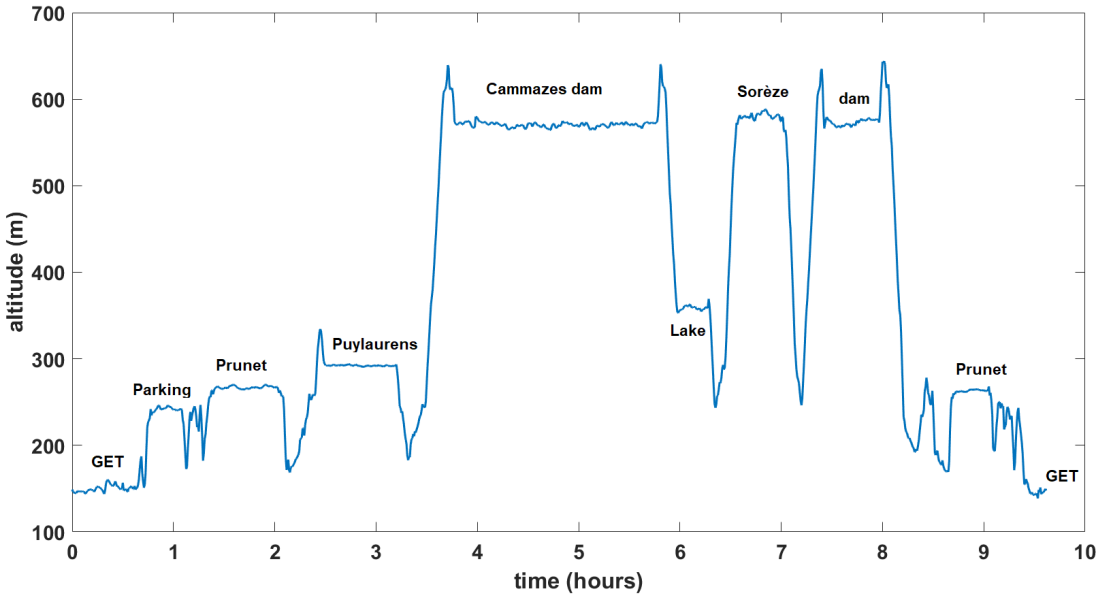

Fig. 5.3 Altitude throughout the day with the different locations obtained when the vehicle stopped and the INS and the CG-5 are stabilized

Our route was as followed; installation of the material at 7:30am and departure from the GET laboratory at 8:30am. From this point, the INS/GNSS was turned on and recorded continuously with a frequency of 0.033Hz for the duration of the experiment. A first stop was done after an altitude difference of ~100 meters. At every stop the CG-5 was turned on and positioned horizontally and away from as many disturbances as possible. Only the person that would turn on the gravimeter

remained next to it and avoided any movements while the others stayed away, as just walking close to a gravimeter would alter the results. When the measurement is complete, the CG-5 is stopped.

5.3 Gravimetric measurements from the relative gravimeter

At every stop three measurements were done by the gravimeter (1 measurement every 60 seconds) and only if the results did not deviate more than ±0.05mGal the results were kept, else I started over and made three new measurements.

Table 5.1 corresponds to the data obtained from the CG5-gravimeter, the number corresponding to the location of the measurement (8 different locations, of which 3 were repeated when looping back; GET, Prunet Cammazes), the relative value obtained in mGal, the standard deviation, the duration of the recording (in seconds), the time when the measurement was started, the date and the name of the location, which is entered manually. Just as explained previously, the values of the gravimeter (~5130 mGal) are relative and are the difference (anomaly) with the value it's calibrated to of 975300 mGal. For a local gravity of 975300 this relative gravimeter would record a gravity anomaly of 0 mGal.

loc #	g (mgal)	STD	ΔT	hh:mm:ss	yyyy/mm/dd	loc name
1	5131.010	0.024	60	07:00:03	2020/11/18	GET
1	5131.013	0.046	60	07:01:12	2020/11/18	GET
1	5131.014	0.027	60	07:02:18	2020/11/18	GET
2	5111.196	0.025	60	08:11:01	2020/11/18	PRK
2	5111.199	0.055	60	08:12:10	2020/11/18	PRK
2	5111.198	0.036	60	08:13:16	2020/11/18	PRK
4	5104.024	0.049	60	09:10:57	2020/11/18	PRU
4	5104.031	0.063	60	09:12:06	2020/11/18	PRU
4	5104.032	0.047	60	09:13:12	2020/11/18	PRU
5	5096.383	0.039	60	10:17:55	2020/11/18	PUY
5	5096.383	0.050	60	10:19:04	2020/11/18	PUY
5	5096.384	0.052	60	10:20:10	2020/11/18	PUY
6	5019.251	0.041	60	11:40:43	2020/11/18	BAR
6	5019.253	0.028	60	11:41:52	2020/11/18	BAR
6	5019.251	0.033	60	11:42:58	2020/11/18	BAR
7	5060.689	0.037	60	14:04:16	2020/11/18	LAC
7	5060.689	0.033	60	14:05:25	2020/11/18	LAC

7	5060.686	0.038	60	14:06:31	2020/11/18	LAC
8	5018.796	0.031	60	14:48:35	2020/11/18	PTH
8	5018.796	0.027	60	14:49:44	2020/11/18	PTH
8	5018.794	0.026	60	14:50:50	2020/11/18	PTH
6	5019.320	0.036	60	15:35:18	2020/11/18	BAR
6	5019.320	0.036	60	15:36:27	2020/11/18	BAR
6	5019.320	0.035	60	15:37:33	2020/11/18	BAR
4	5104.148	0.057	60	16:45:38	2020/11/18	PRU
4	5104.147	0.058	60	16:46:47	2020/11/18	PRU
4	5104.150	0.028	60	16:47:53	2020/11/18	PRU
1	5131.060	0.074	60	17:52:29	2020/11/18	GET
1	5131.061	0.041	60	17:53:38	2020/11/18	GET
1	5131.062	0.032	60	17:54:44	2020/11/18	GET

Table 5.1- Recorded .csv file by CG-5 gravimeter at different stops

Our 2nd stop was at Prunet at an altitude of 265 meters. This would be one of three locations we revisited the same day in order to have measurements at the exact same coordinates at different times during the day. Our 3rd stop is Puylaurens which is the location of an IGN absolute gravity reference point (Fig. 5.4).

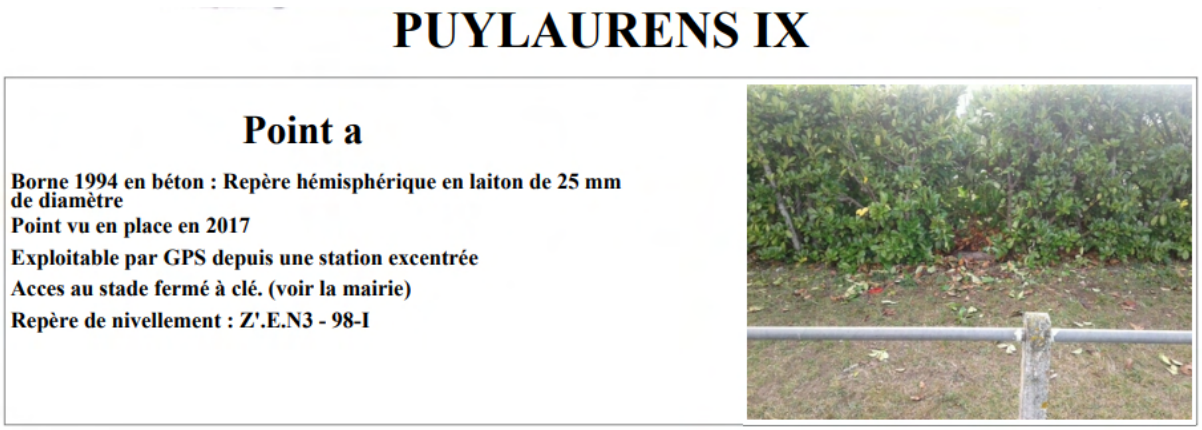

Fig. 5.4 Puylaurens reference point information (modified from IGN notice)

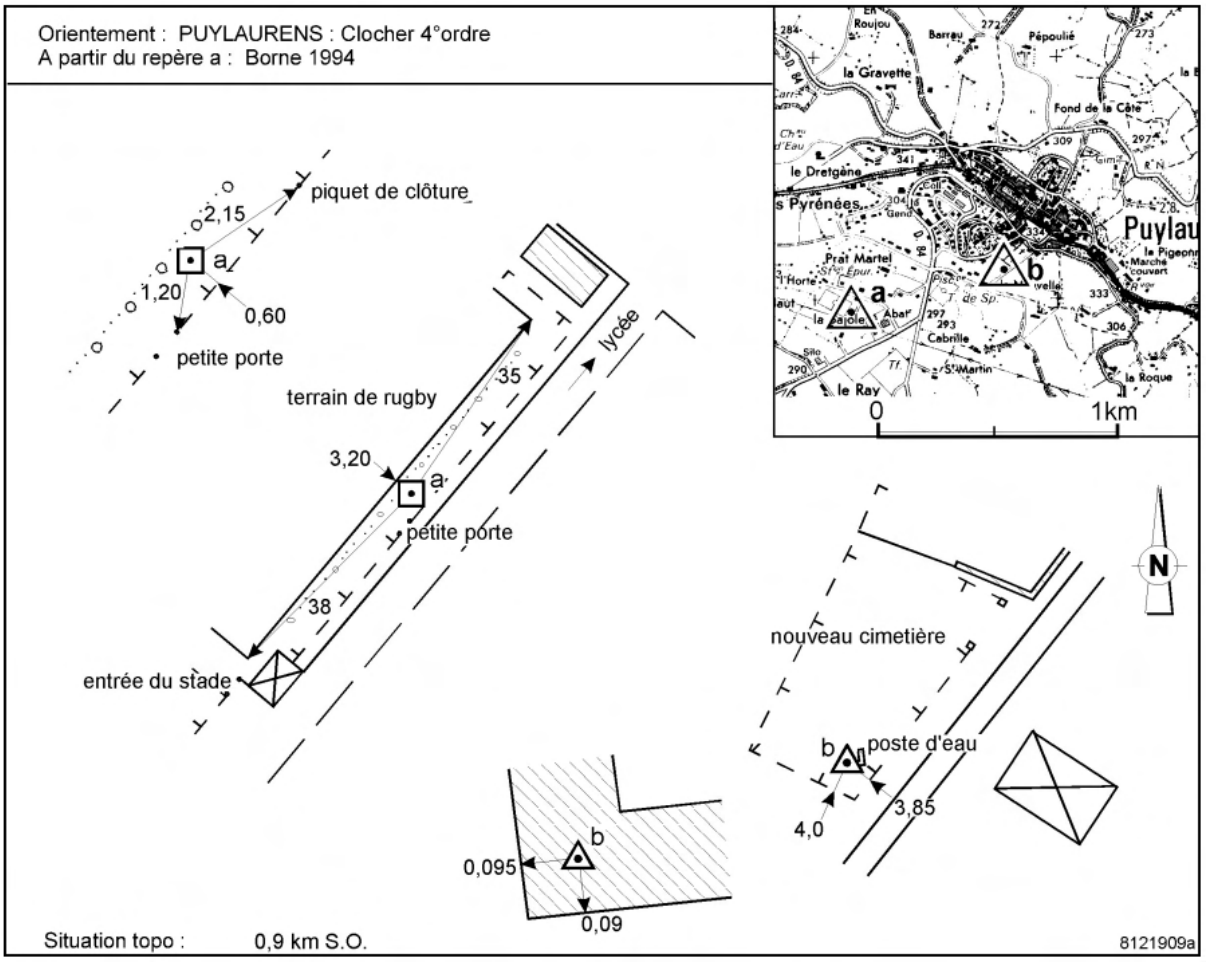

Fig. 5.5 Map of the location of IGN reference point at Puylaurens

Système : RGF93 v2b (ETRS89) - Ellipsoïde : IAG GRS 1980

Point	Longitude (dms)	Latitude (dms)	Hauteur (m)	Précision
a	2° 00' 14.86086" E	43° 34' 04.63230" N	340.293	< 1 cm

Système : RGF93 v2b (ETRS89) - Projection : LAMBERT-93
Système altimétrique : NGF-IGN 1969

Point	e (m)	n (m)	Précision plani	Altitude (m)	Précision alti
a	619521.507	6274828.605	< 1 cm	291.113	< 5 mm

Réseau de référence gravimétrique : France métropolitaine 2017

Point	g (mGal)	Précision (µGal)	g (m.s $^{-2}$)	Précision	Année
a	980396.906	20	9.80396906	2.10 $^{-7}$	2019

Table 5.2 - Coordinates and absolute value for gravity at IGN reference point in Puylaurens

The IGN value at this reference point (Fig. 5.5) was 980396.906mGal (Table 5.2). I took the difference between this value and that given by the CG-5 gravimeter and subtract this difference from our results for the other locations. I obtained a gravity difference of 5096.383 mGal at this location (with this calibration, at a location with a local gravity of 975300 mGal, our relative gravimeter would record a value of 0

mGal). At Prunet I had an average value of 5104.029 mGal, so thanks to the reference point I know the absolute gravity value at that time. I do the same for all the recorded points e.g. at Prunet the absolute value was:

(5104.029-5096.383)+980396.906 = 980404.552 mGal.

At noon we arrived at the Cammazes dam (‘Barrage des Cammazes’) and had a break for lunch. This was the location where I obtained the most data points. At this point we had climbed over 400 meters since our starting point. In the afternoon we had driven down again to the lake of Saint-Ferréol (‘Lac de Saint-Ferréol’) which is less than an hour drive but a large altitude difference of 100 meters. From there we went to Sorèze, driving in a mountainous area until we reached the highest point possible within a reasonable time, at 580 meters. This point was the highest altitude reached and measured during the field trip. We turned back and picked up our colleagues at the Cammazes Dam who were performing their own GNSS-R experiment. I also used this opportunity to retake new measurements for comparison as this would be 2,5 hours later in the same day.
On the way back to the laboratory I went to Prunet, which I had planned to do in order to have a set of measurements for this location taken during the morning and during the evening. The main reason for this was to help quantify the daily drift the CG-5 gravimeter would present. The return at the laboratory would be 12 hours after departure.

The difference in gravity given by the gravimeter for Prunet in the morning and evening is 0.12mGal with the time between both measurements being 7,5 hours, this gave us a drift of 0.0159 mGal/h. For the Barrages dam this difference is 0.068mGal with a time difference of 4,5 hours, giving us a drift of 0.0151 mGal/h which is coherent with the drift obtained for Prunet and in the error margin of the CG-5. I took the average value of the hourly drifts, 0.0155mGal/h, and for each set of data I took the difference in time since the departure at the laboratory (in hours) and multiplied by the hourly drift. This corrected data is presented on figure 5.6 (blue circles). The violet dot corresponds to the measurement at Puylaurens, the IGN reference point. I quickly noticed the influence of the altitude on the gravimetric data. The higher the altitude, i.e. the further we are from the center of the Earth, the less gravitational pull

we are subjected to. As seen before, the gravitational pull decreases by a factor of $1/r^2$ (Eq. 11). For altitudes that are still close to Earth, relative to its size, I can use Eq. 1.11.
Eq. 1.10 defines that for every meter above the model of the Earth ellipsoid, the gravitational pull decreases by 0.3085 mGal. This is the Free-Air correction that is calculated from Newton's law.

Important to note, this free-air correction for different altitudes assumes there is only air between the altitude considered and the ellipsoid, hence the term "free-air anomaly". Because the altitude change is due to the local topography that we are driving on, this Δg between our stops will not be equal to 0.3085 mGal times the altitude difference (in meters) but it will be slightly lower. For a theoretical calculation the topography needs to be considered, for which one would need to use a digital terrain model (DTM) of the region. But for the purpose of just explaining the gravity variation due to altitude the above formula is good enough. For example the difference in elevation between the GET laboratory and Cammazes dam is 420 meters, using the free-air correction there would be a gravity difference of 129.57mGal. Looking at the measurements made by the gravimeter I obtained $g_{GET} = 9.804315350$ and $g_{DAM} = 9.803198426$, so a difference of 111.69 mGal. This means a difference of 0.2659 mGal for every meter of altitude difference, as expected a lower change in gravity because this is not a free-air anomaly, the topography needs to be accounted for as well.

5.4 Gravimetric measurements from the INS/GNSS

Regarding the accelerometric data from the INS/GNSS, the advantage was the continuous measurements throughout the day. This meant that if a stop took longer than usual, it would also result in more data points from the INS/GNSS.

Throughout the day I would note down when we'd arrive at our location and when we'd leave but by analyzing the velocity and acceleration data along the x and y axis it is also easy to find the exact time where we came to a halt and when we left. Using this I would isolate the data points corresponding to each location. From here I would remove the outliers that are caused by opening the back of the van, moving the

CG-5 gravimeter, closing the doors, etc. While the gravimeter is placed on an adjustable tripod, this was not the case for the INS/GNSS that was attached to the inside of a box inside the van, connected to a pc. Because of this the van would never be parked in an exact horizontal position. For this reason I would take the norm of the acceleration data along the x-,y- and z-axes. This would give me the radial value of gravity towards the center of Earth.

Once I obtained the radial value of gravity I would take the average value for each set of data points corresponding to a different location. The first value obtained from the INS/GNSS, at the GET laboratory, would be calibrated to the value obtained from the CG-5 gravimeter, as there was a difference of 0.03m/s² in its calibration.
This data is presented on figure 5.6 with red crosses and is why for the first set of data at the laboratory, the INS/GNSS value is the same as the one from the gravimeter. Immediately I notice that for 5 of the 10 data sets the value from the INS/GNSS does not closely match the correct value, the value obtained with the CG-5 gravimeter.

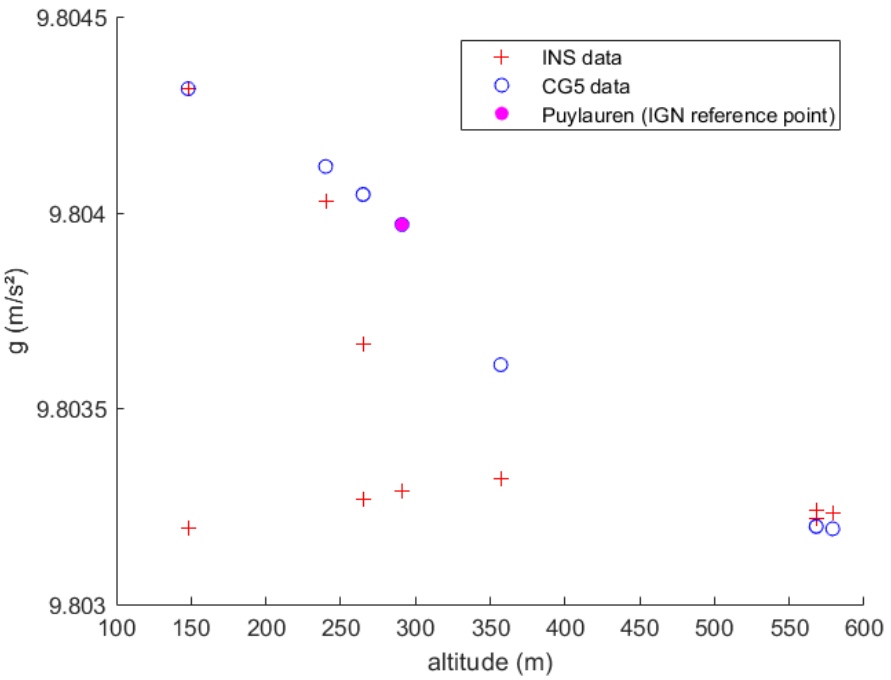

Fig. 5.6 Uncorrected INS/GNSS data and drift corrected CG-5 data for different altitudes

The important difference between the red crosses that do closely match the measurements of the gravimeter is the duration of the stop and thus the amount of data points the INS/GNSS recorded for those locations. Every measurement that does not closely match the gravimeter corresponds to less than 50 collected data points, meaning the stop was shorter than 25 minutes, while the other locations, for example Cammazes dam where we took a break for lunch, would have more than that (>100 points). What I hadn't done yet for those data sets, was apply a temperature correction.

Because the value of g at the GET laboratory, Prunet and the Cammazes dam should be almost exactly the same for the first and second recording (even considering the solid tides for that date), I can look at the difference of g measured by the INS/GNSS and plot it against the temperature difference between the first and second data set for those locations. The difference in temperature (ΔT) will be lowest between the first and second recording at the Cammazes Dam, because those sets of data were only recorded a few hours apart. On the other hand the difference in temperature for the first and second set of data at the GET laboratory will be highest because they were recorded at the start and finish, 12 hours apart. I will then use the linear law of figure 5.7 to find the thermal drift of this INS/GNSS used. This temperature bias will not necessarily follow the same law as the INS/GNSS used for the first experiment (same SPATIAL model but two different INS/GNSS).

Even though only three locations could be used to plot the INS/GNSS accelerometric data against the temperature differences, I still see the thermal drift follows a linear trend, just like the first experiment. For this INS/GNSS every increase in temperature of 1°C will decrease the measured gravitational acceleration by $2.1 * 10^{-4}$ m/s² (thermal drift of the first INS/GNSS used was a decrease of $6.2 * 10^{-3}$ m/s² for every increase in temperature by 1°C).

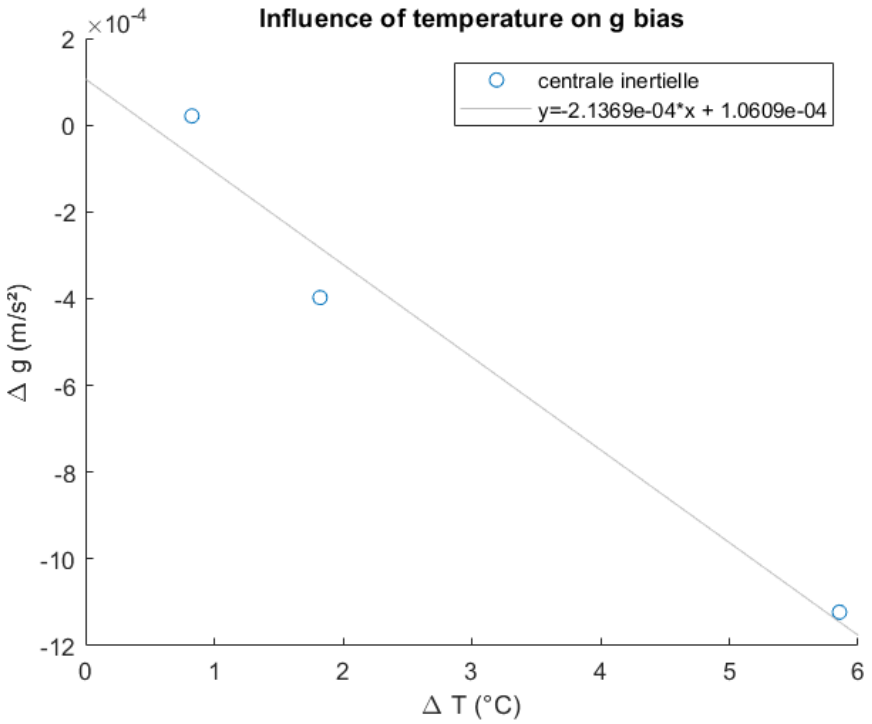

Fig. 5.7 Difference in g measured by the INS for the three locations we looped at (Dam, Prunet and the laboratory, in that order) against the difference in temperature between both passings

From here I calculated the temperature difference between the first measurement (startup at laboratory) and each measurement at a different location with insufficient data and corrected the temperature bias with the linear law previously mentioned.

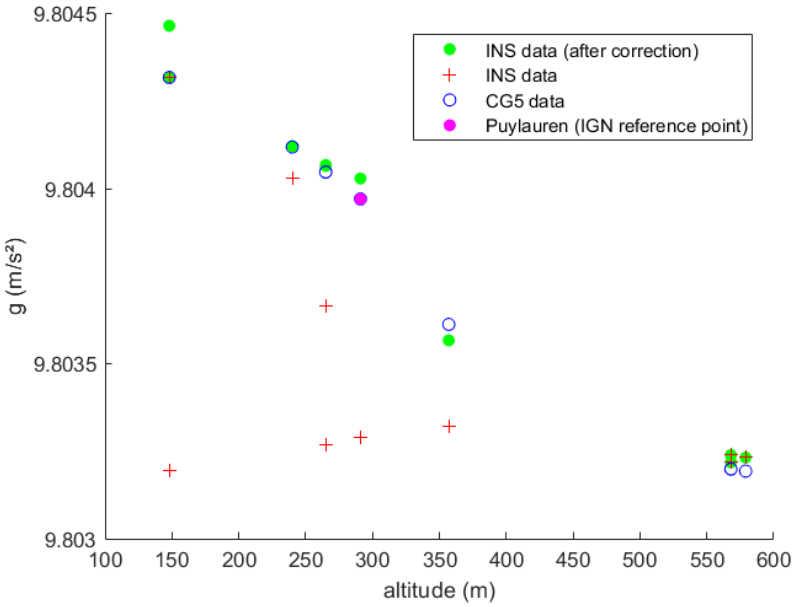

Fig. 5.8 Measurements of g by the INS/GNSS (before and after correction) and the gravimeter for the different altitudes

Now that the data for the locations with few measurements is corrected, I can see that for the locations where previously the red crosses would not match up well, the green circles (corrected data) are closer to the measurements made by the CG-5 gravimeter. Figure 5.8 shows that the INS/GNSS gives values close to those measured with a relative gravimeter and a correlation between the altitude and gravity values obtained.

These results were presented at the IGARSS 2021 - 2021 IEEE International Geoscience and Remote Sensing conference (Beirens et al., 2021). (10.1109/IGARSS47720.2021.9554499)

5.5 Effect of latitude on gravity

When deciding on the exact route from the laboratory to the Cammazes dam, another factor was also taken into account. I wanted to see if I could possibly observe the effect of not just altitude, but also latitude on the gravitational measurements.

As can be seen on figure 5.2 which maps our trajectory using the GPS coordinates, when driving from the GET laboratory to Puylaurens, we maintain approximately the same latitude, as much as the roads allow us, and only change our longitude. From Puylaurens we drove to the Cammazes dam maintaining the same longitude and only changing the latitude. (Latitude φ GET: 43.56139, Puylaurens: 43.56794, Dam: 43.40774)

I mentioned earlier the change in gravity for every meter by comparing the measurements between the laboratory and the dam, and why it differs slightly from the free-air anomaly of 0.3085mGal/m. For this part we'll compare the measurements done between the starting point and Puylaurens (same latitude) and then between Puylaurens and the dam (same longitude, different latitude).

$$g_{GET} - g_{Puylauren} = 9.804315350 - 9.803969060 = 3.4629 * 10^{-4}\, m/s^2$$

$$\frac{g_{GET}-g_{Puylaurens}}{\left|h_{GET}-h_{Puylaurens}\right|}=\frac{3.4629*10^{-4}}{|147-291|}=0.24048\,mGal/m$$

Between Puylaurens and the GET I observed a change of 0.2405mGal for every meter (when I looked at the difference between GET and the dam I obtained 0.2659 mGal/m), and the difference in latitude between these two points was 0° 0.2078'.

$$g_{Puylaurens}-g_{Dam}=9.803969060-9.803198426=7.70634*10^{-4}\,m/s^2$$

$$\frac{g_{Puylaurens}-g_{Dam}}{\left|h_{Puylaurens}-h_{Dam}\right|}=\frac{7.70634*10^{-4}}{|291-568|}=0.2782\,mGal/m$$

From Puylaurens to the Cammazes dam I observed a bigger change in gravity with every meter of altitude, which is why the average value for the whole day was higher than just from GET to Puylaurens. The biggest contributor to this difference is the latitude variation between those points (the other, smaller component being the topography). Between the observation point at the dam and Puylaurens there is a latitude difference of 0° 9.612'. As I mentioned before, because of the rotation on Earth, the Earth 'bulges' more at the equator than at the poles (radius of Earth at the poles 6357 km, at the equator 6378 km), and from the formula of gravity we know an increase in distance, means a decrease in gravity (factor of $\frac{1}{r^2}$).

Using the WELMEC formula (Eq. 1.11) and the latitude and altitude of the GET laboratory (φ = 43° 33.68', h = 147 m), I obtain a theoretical value for the local gravity of 9.80444966 m/s² and for Puylaurenss (φ = 43° 34.08', h = 291 m) this value is 9.80400664 m/s² (both these theoretical values match closely to the values obtained with the gravimeter). The difference in value is almost exclusively coming from the altitude difference, because the latitudes are almost the same. If I use the hypothesis that the topography between Puylaurenss and the Cammazes dam is similar, I can calculate the change in gravity that is due to the latitude variation and see if it matches closely to the theoretical influence of latitude.

For this I take the difference in altitude between the observation point at the dam and Puylaurenss, which is 277 meters, multiply this by the value for the change in gravity due to the altitude, calculated between Puylaurens and GET (0.24048 mGal/m)

which gives a value of 9.8033405104 m/s², compared to the value obtained using the gravimeter of 9.80319826 m/s², a difference of 0.00014225 m/s² (14.225 mGal).

The theoretical value for a point with a latitude of 43°24.46’ (Cammazes dam) and an altitude of 291 meters (Puylaurens) would be 9.80386188 m/s², the difference with the theoretical value at Puylaurens is 0.00014476 m/s² (14.476 mGal), which is the theoretical change in gravity due to the latitude, which is close to the value obtained with the gravimeter above.

CHAPTER 6 Study case:
Using the INS/GNSS for airborne gravimetry

6.1 Methodology of the experiment

After multiple static experiments to study the instrument's capabilities and limitations, I then moved on to an experiment to test it in a mobile environment, as the main advantage of using this instrument compared to a gravimeter, is the possibility of using it for mobile gravimetry.

From the 27th to the 30th of March 2021, multiple flights were done using the Boreal LAB drone over fields in the commune of Saint-Hilaire-de-Chaléons, which is located in Western France. A total of five flights were done during these four days. Multiple flights were done because some of these flights encountered technical issues, for example cables disconnecting during take-off as the drone and the material inside would be subjected to multiple G-force (close to 10g), data being corrupted due to a computer memory problem or meteorological reasons cutting the flights short. From the corrections made to the payload, the best data was obtained from the 5th flight. The goal of this experiment was to use the SPATIAL and MOTUS for airborne gravimetry using a fixed wing drone. Unlike in situ experiments, for mobile gravimetry I will need to use the GPS data in order to derive it to obtain the accelerations that are coming from the movement of the drone, and not part of the gravity signal.

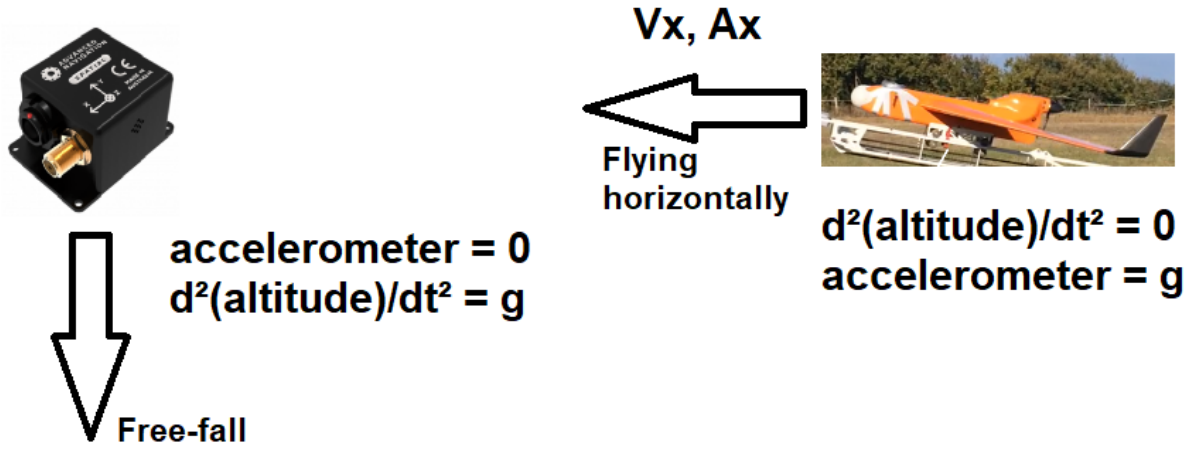

Fig. 6.1 Visual representation of the extreme (unrealistic) cases (free-fall & perfect horizontal flight) and how I obtain the value for gravity in those situations.

Figure 6.1 is a visual representation of the principle, in which both extreme (unrealistic) cases are presented. The INS/GNSS and IMU are attached to the inside of the drone, so they share the same inertial frame. In a hypothetical case, if the drone were to be falling in free-fall, which is unrealistic because of the air resistance on the wings, the accelerometer would be recording an acceleration of 0 m/s², as I explained before. But thanks to the recorded altitude from the GPS data, taking the second derivative would give us the acceleration along the z-axis (down) which would be equal to the local value of gravity.

On the other hand, if the drone was flying in a perfect straight line, with no changes to it's altitude, the second derivative along the z-axis would be 0 m/s², but the accelerometer, supported by the drone platform just as it would be positioned on a table at rest, would give an acceleration along the z-axis (down) equal to the value of the gravity, even if the drone was accelerating along it's x-axis (pointing to the nose of the drone).

Fig. 6.2 Satellite image of flight area

This is a satellite image (Fig. 6.2) of the zone where this flight took place. This region is covered with fields and very little traffic on the roads. The flight locations have to be chosen carefully as multiple regulations need to be followed in France when flying a drone in the 'open' category.

Some of the regulations that need to be followed are:

-The drone needs to weigh less than 25 kg at take-off.

-The drone needs to be kept at a safe distance from civilians.

-The drone will not fly directly over people.

-The drone will not fly at an altitude over 120m.

-The pilot must keep a visual line of sight with the drone.

-The drone cannot carry dangerous materials.

Because of the locations chosen, the pilot can follow these regulations. Thanks to the many fields in this area there will be no civilians nearby and won't fly directly above people. The flat nature of this region and lack of objects allow the pilot to maintain a visual line of sight with the drone and stay under an altitude of 120m.

6.2 Digital terrain model of the region

I obtained the DTM (Digital Terrain Model) data of this region (Fig. 6.3) from IGN (Institut national de l'information géographique et forestière) from their RGE ALTI data, which was obtained by LIDAR (LIght Detection And Ranging of Laser Imaging Detection And Ranging). The DTM gives information on the elevation of the topography of a region, not to be confused with a DEM (Digital Elevation Model) which includes data on objects that are present, like buildings and trees. Downloading this data will give text files with three columns; longitude, latitude and altitude. This data is separated into multiple grids, the region I considered consisted of 9 different grids. These text files will start with the point in the top left point corner of the grid, move right (changing longitude but not latitude) until reaching the top right corner before jumping to the next line starting on the left side again (changing the latitude and longitude). Because of this it's important to correctly go through the different files in the correct order. Another process that needed to be done is to transform the DTM data from the Lambert-93 coordinate reference system to WSG84, because the Spatial INS/GNSS uses WSG84. Lambert-93 is the conic projection used for Metropolitan France. With the data correctly transformed and sorted I can represent the topography. (Note for visual reasons this is presented looking from the top right corner, as this is where the altitude is lowest.)

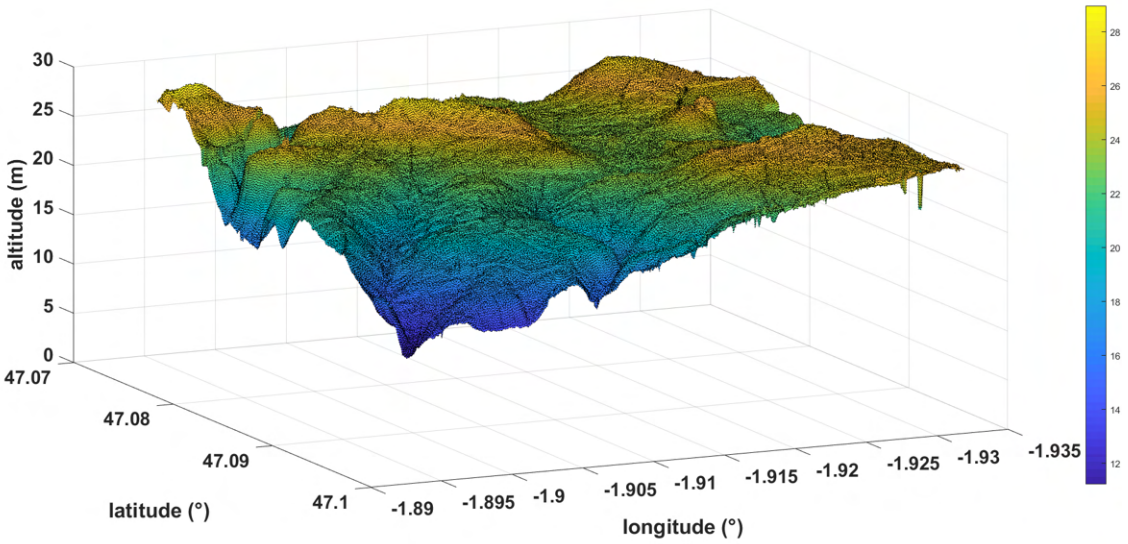

Fig. 6.3 3D representation of the digital terrain model for the region of the flight

The width and length is approximately 3.5km and shows this region has very little topography changes.

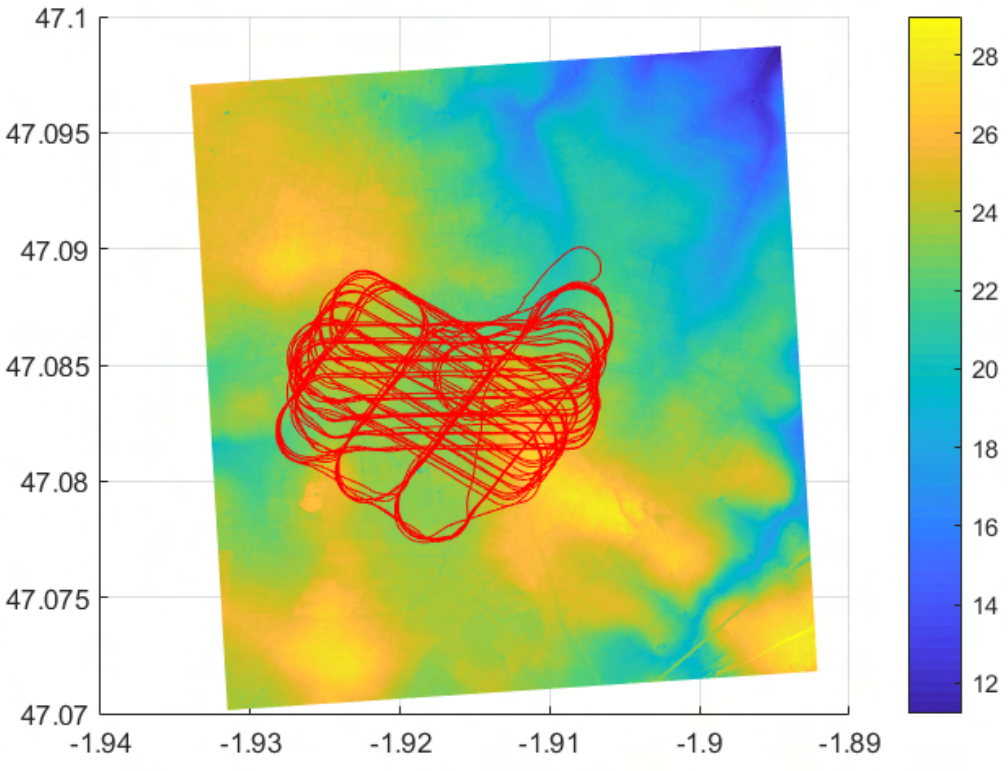

Fig. 6.4 Longitude, latitude and altitude of the region where the flight took place with the trajectory of the flight (red) plotted on top of it.

From here I represent all the recorded points during the drone flight on top of the DTM (Fig. 6.4). The total amount of recorded data points is 680924 for the SPATIAL

INS/GNSS, but this includes many repeated points because the on-board computer was recording at a rate of 100Hz but the INS/GNSS was only sending data at 16.67Hz. This is because some of the other instruments included in the payload required a higher sampling frequency than what I used for the INS/GNSS. This means every recorded point of the INS/GNSS would be repeated 6 or 7 times. I removed all these duplicates by only keeping the data when the associated time would change, which left me with 110990 points, each one separated by a period of 0.06s for a total of 1000 recorded points every minute. The total length of the recording is 110 minutes, with the first 15 minutes being during preparation of the payload and drone.

The INS/GNSS was now set to a much higher sampling frequency compared to the previous studies, because those were static experiments. If the sampling frequency was set too low, for example 1 measurement every minute, then I would have no data during certain turns or straight lines.

6.3 Topography influence on gravity for this region

The DEM data I used had 502681 data points (709x709 grid) and by calculating the difference in longitude and latitude between points I obtained the surface associated with each data point and by multiplying this surface with the corresponding elevation and the density of the Earth's crust (ϱ = 2600 kg/m^3) gives me the mass of each column that makes up this grid (I assume each column has a uniform distribution of its mass). Using Newton's law of gravitation I can then find the attraction from each column on the drone depending on the distance, *r,* between the center of mass of the column and the angle θ, if we're only interested in the radial component. This is visualized Fig. 6.5. To calculate *r,* I used Pythagoras' law with the altitude from the drone (H) and half of the height (h/2, center of mass) of the cuboid obtained from the DTM together with the distance d, obtained from the coordinates of the drone (GNSS) and the cuboid (DTM).

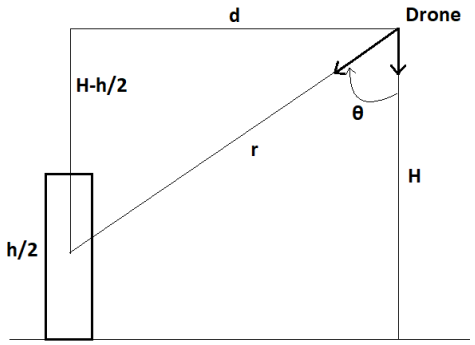

Fig. 6.5 Visual representation for the calculation of the gravity anomaly from one column of the digital terrain model

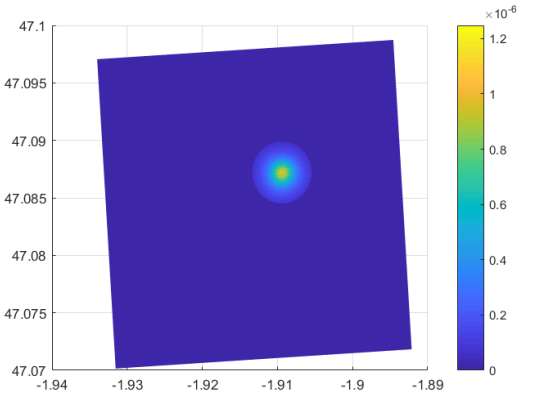

Fig. 6.6 Gravity influence of different columns for one point (highest value for columns just below separated by the lowest distance)

Seeing how there are 502681 columns on this grid and the attraction of each one needs to be calculated for each recorded data point of the drone, since the distance to each column will change, these calculations would take a lot of time, even for just a straight line which is ~500-600 points. Because of this I would only consider the columns within a certain distance of the drone, as the attraction quickly drops with a factor of $cos(\theta)/r^2$. Figure 6.6 shows the result for the first point on a straight line, with the biggest component being from the columns just below the drone where $cos\theta = 1$ and r is lowest.

Taking the sum of all the values and applying this to a complete straight line gives us the result on figure 6.7.

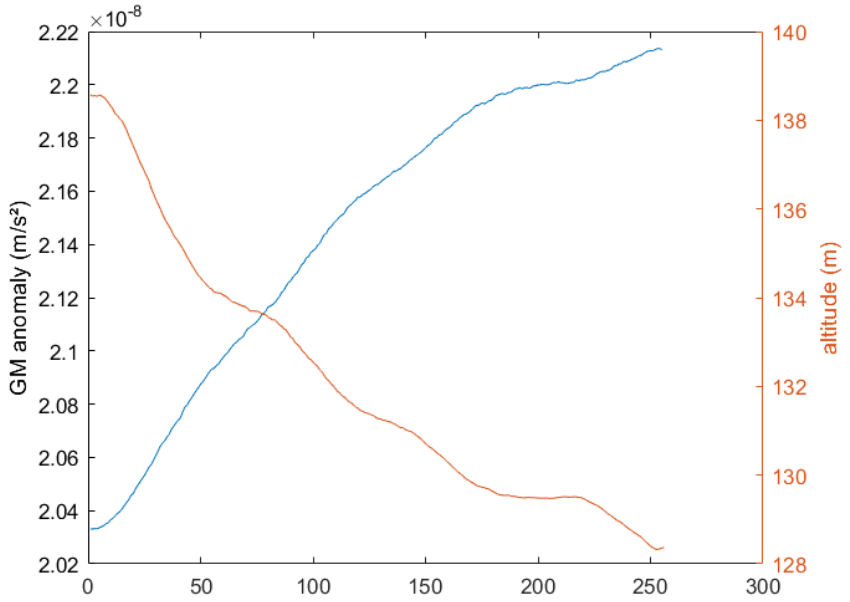

Fig. 6.7 Theoretical gravity anomaly (blue) calculated for each point on a straight line (250 points considered for this straight line) depending on the topography and distance to the topography for each point (does not include the free-air anomaly)

Due to the rather low topography changes, the main factor of the topography is the decrease or increase in altitude of the drone which changes the distance *r* to the considered cuboids. Nonetheless I learn from this that the attraction due to topography variations (at most 20 meters) will be negligible and with the precision of this INS/GNSS and noise caused by the vibrations would be impossible to detect in this region.

6.4 Trajectory and altitude of the drone

The drone is usually flying along a hippodrome trajectory when on auto-pilot. The drone will fly along multiple parallel hippodromes before changing direction. Figure 6.8 shows the altitude for the complete flight. The altitude is given by the INS/GNSS and is the altitude above the reference ellipsoid plus the orthometric height, which is why at the ground level gives an altitude of 70 meters and not 20 meters (which is the altitude above the reference ellipsoid).

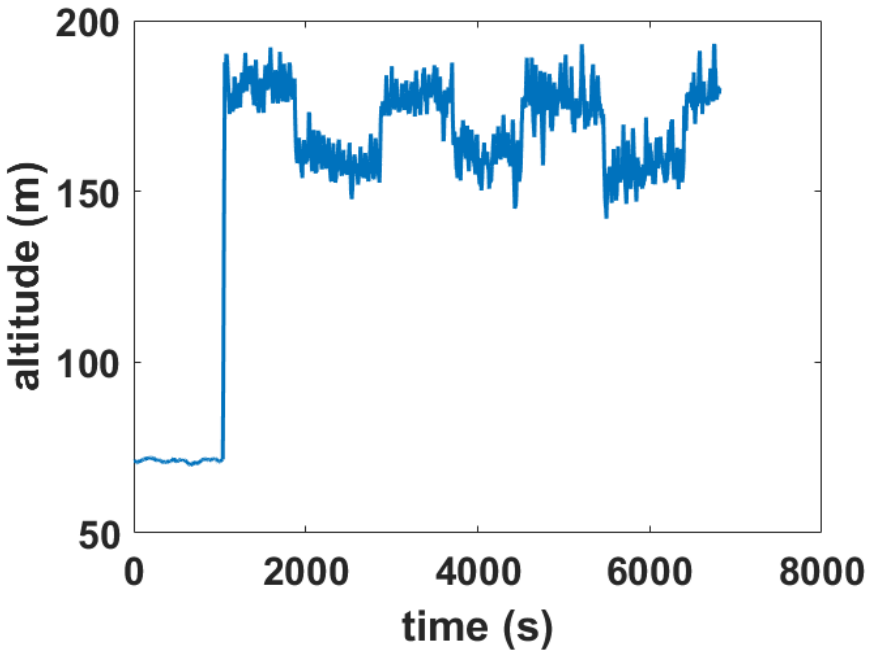

Fig. 6.8 Altitude for the complete flight, including preparations and the duration (in seconds)

Part of the payload was for a different study regarding air resistance, for which equipment was installed on the outside of the drone to measure airflow, which would also cause air to come inside the drone. It is also for this study that the drone would fly at different altitudes (180 meters and 160 meters) at different periods of time. The drone would swap between these two altitudes approximately every 15 minutes.

As we've shown during the previous studies, it's important that the temperature bias of the SPATIAL models are corrected. On figure 6.9 I present the temperature throughout the whole flight together with the altitude. I can see that while the drone is at rest but the equipment on board is turned on, the temperature rises quickly until the drone is launched. When the instruments are turned on their electrical heating will cause the temperature to rise, on top of that all the equipment is enclosed inside the drone with no airflow when it's at rest, which causes the temperature to rise so fast. Once the drone is mid-flight the airflow, caused by the previously mentioned study, will cool down the inside of the drone which can be seen on the graph.

The SPATIAL used here is the same one as the very first study, so I know the law and how to correct the temperature bias. Luckily as well the temperature doesn't change more than 2°C, which is thanks to the constant airflow and the short duration of the flight.

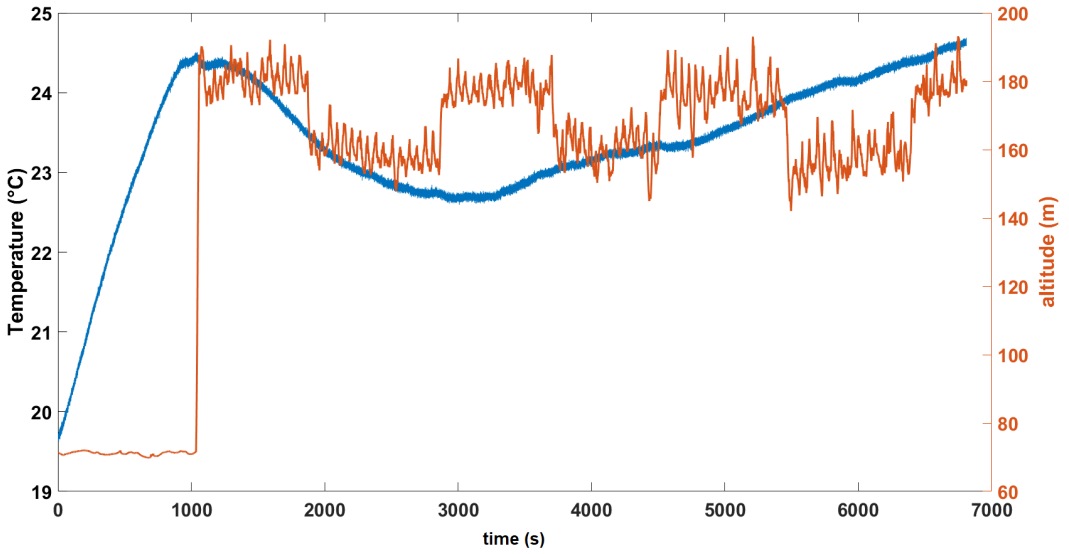

Fig. 6.9 Altitude (red) and temperature (blue) for the complete flight (including preparation on the ground)

The small altitude changes at each of these two altitudes happen between the straight lines and the turns. During a straight line the drone will slowly descend, before regaining altitude during the turn. This is shown in figure 6.10 and 6.11, with the red dot showing the first point of the considered data of a straight line.

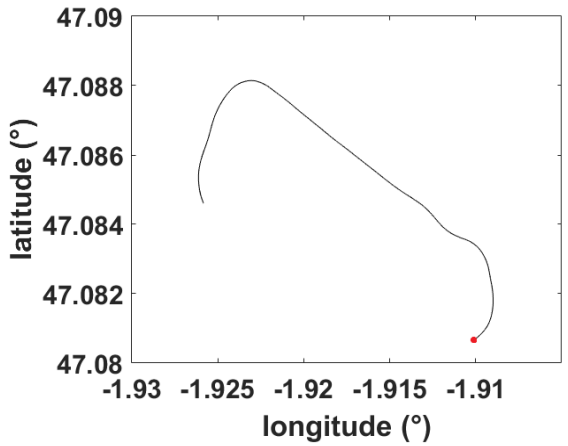

Fig. 6.10 Latitude and longitude of a straight line including the turn just before and after

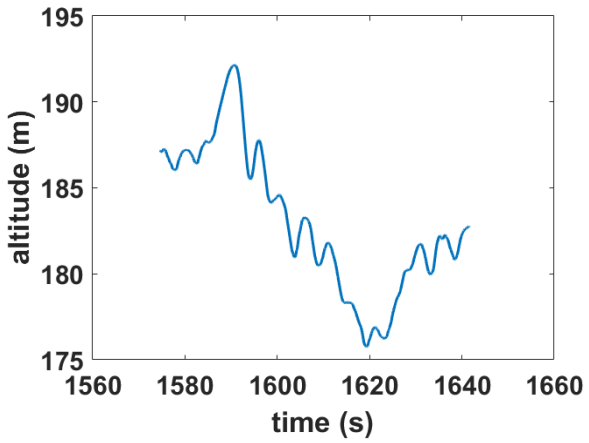

Fig. 6.11 Altitude of a straight line including the ascension during the turns before and after

6.5 Analysis of singular straight lines

For the first method I would isolate the data of just a few straight lines. The reason is that in those cases the drone would naturally be more horizontal than when it's turning. This means the inertial frame of the INS/GNSS will already be closer to that of the NED-frame and even though a rotation matrix still needs to be applied, as the drone will never be perfectly horizontal for a long period of time, the possible error induced using the pitch, roll and yaw recorded by the gyroscopes, will be smaller. The straight lines chosen would be selected by me among some of the longest ones that were flown by the drone, as some of the hippodromes were much smaller, meaning a shorter straight line. The duration of a straight line is approximately 30 seconds, with a sampling frequency of 16.6 Hz (period of 0.06s) a straight line would consist of roughly 500 data points. From these data points I would extract the GPS coordinates (longitude, latitude and altitude) and transform them to cartesian coordinates (x, y and z, with the launch location defined as origin) and take the first and second time derivative to obtain the acceleration along the down axis. Because the altitude coordinates are in a terrestrial reference frame, a sudden increase in altitude, means an upwards velocity change resulting in an upwards acceleration change. Because the z-axis of the INS/GNSS is pointing down in its own inertial reference frame, this would be recorded as a negative acceleration (a down acceleration would be recorded as a positive acceleration), so when I subtract the kinematic and measured acceleration from one another it will be important to keep in mind this sign difference.
From this straight line I would then also use the accelerations measured along the x-, y- and z-axis along with the recorded roll, pitch and yaw. Using a rotation matrix I would correct the accelerations measured along the three axes at each point in order to work in a NED-frame, before subtracting the kinematic accelerations from the accelerations measured by the INS/GNSS (specific force).

Figure 6.12 is an example of one of the straight lines with the first image showing the altitude changes during one straight line and the velocity in the down direction derived from this GPS data. When the drone is gaining altitude this velocity will be negative and when the drone is descending this down velocity will be positive. When the velocity is 0 m/s the drone's altitude reaches a local maximum or minimum because it changes direction between going up or down.

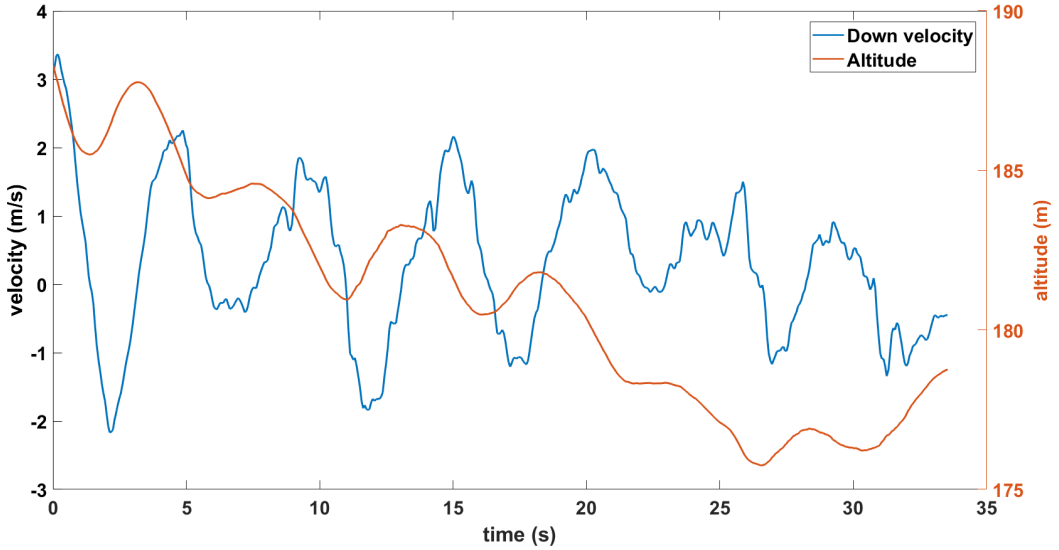

Fig. 6.12 Velocity (down) derived from the GPS data for a straight line (30 seconds)

Figure 6.13 shows the acceleration along the down direction which is derived from the velocity. In this image I can also see that the velocity is decreasing when the acceleration is negative, increasing when the acceleration is positive and reaches a local maximum or minimum when the acceleration is 0 m/s².

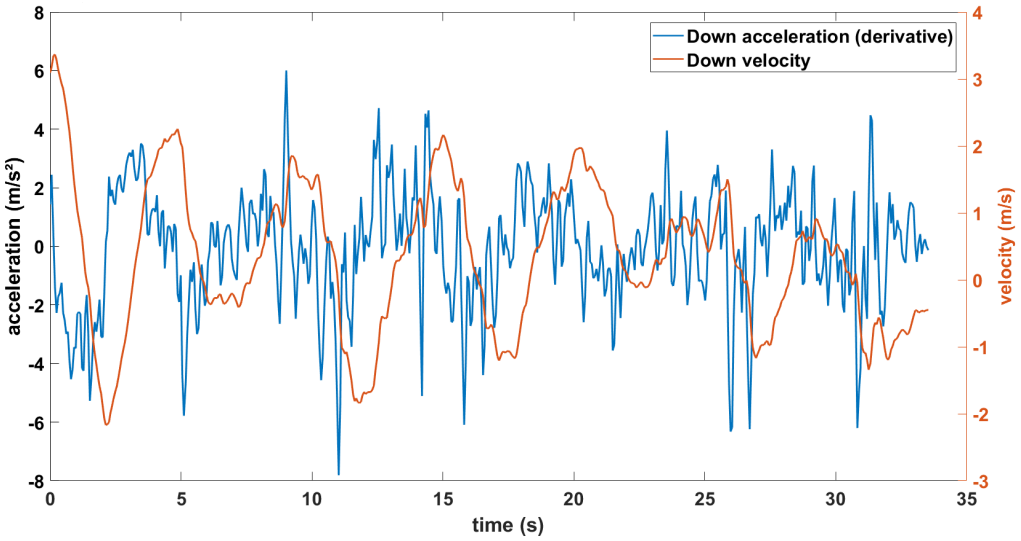

Fig. 6.13 Velocity (derived from GPS) and acceleration (derived from the velocity) for the same straight line

With each consecutive time derivative I notice the noise increasing but if I look at the raw data from the accelerometer (down direction) below, I see a high noise amplitude as well. This does not come as a surprise because this INS/GNSS is strapped down to the drone meaning there is no stabilization platform to remove or

correct the vibrations and small rotational movements from the drone or the vibrations caused by the motor. Figure 6.14 shows this derived acceleration from figure 6.13 and the specific force recorded along the DOWN axis. The yellow signal is the residual when both are subtracted.

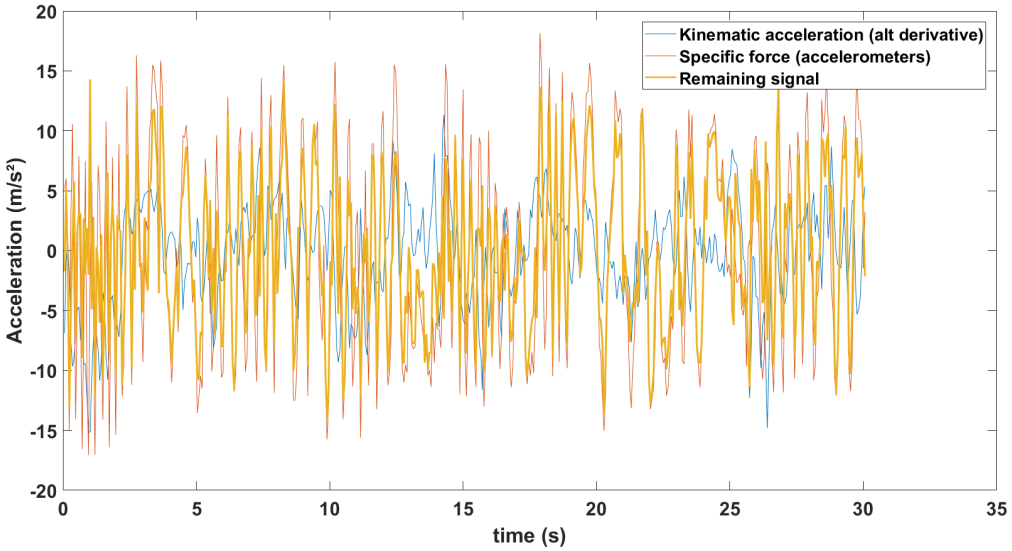

Fig. 6.14 Remaining acceleration signal for a straight line after removing the kinematic acceleration from the specific force recorded by the accelerometers

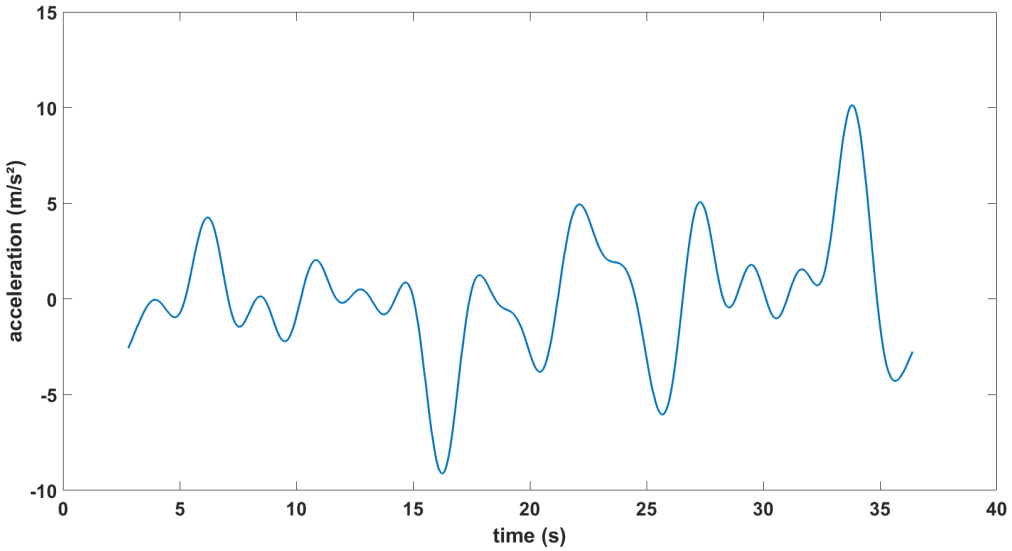

Fig. 6.15 Reconstructed acceleration (down) signal for one straight line after filtering

By applying a filter I obtain a result that is centered around 0 m/s² (fig. 6.15) which is what I would expect, however there are still large peaks present of +- 10 m/s². One of the problems is that I'm trying to look at singular lines, just like the studies before did, but with the main difference being the length of these lines. Those studies used

large planes and drones that were able to fly much longer and further, which our drone could do but wasn't allowed to do due to regulations. Because of the difference in length of their considered data they were able to use low-pass filters of 120-160s allowing them to remove much more noise.

6.6 Vibrations caused by the motor

Looking at the raw data from the accelerometer along the down axis I can see an amplitude of similar order when the drone is being prepared. Figure 6.16 (and 6.17 for the North and East directions) below shows the different steps up until the launch of the drone using a slingshot catapult. First the onboard instruments and computer are turned on, the small accelerations recorded are due to people touching the drone or the payload inside. Next I can see exactly when the motor of the drone is turned on while still at rest. I can see just how much these vibrations will hide the gravitational signal.

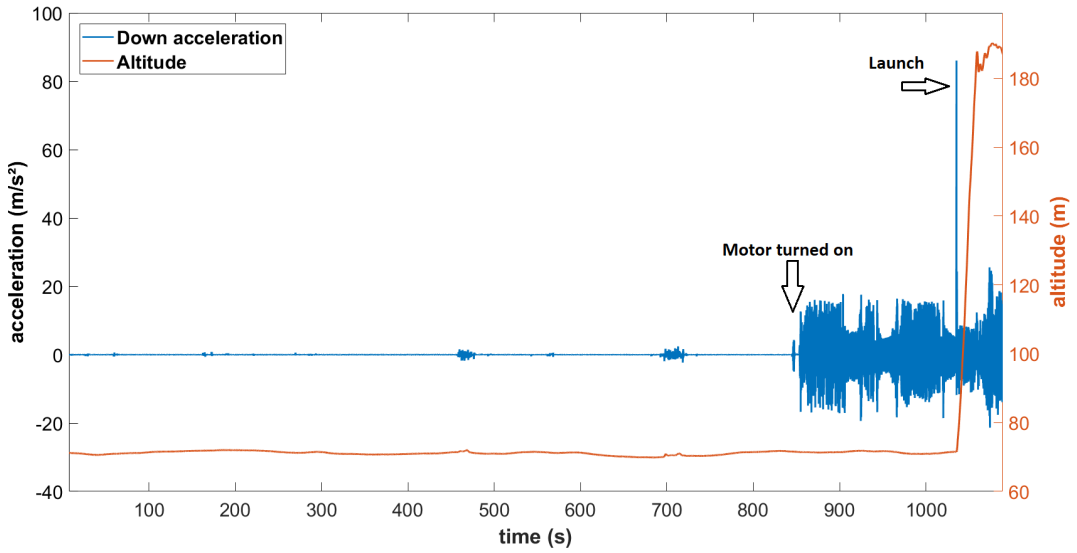

Fig. 6.16 Down acceleration starting from the on-board computer being turned on until launch, presenting the vibrations caused just by the drone's motor

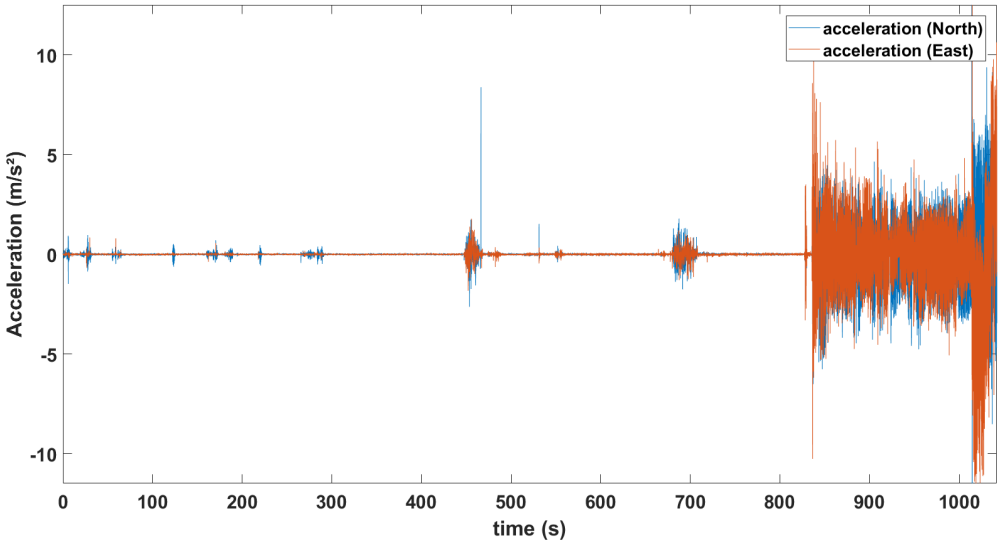

Fig. 6.17 North and East accelerations for the same period

With the amplitude of the vibrations from the motor being so high I will also need to remove as much of the signal that is caused by it. The frequency spectrum of that signal is included below (figure 6.18). Unfortunately because the drone, with its motor turned on, was only at rest for a couple of minutes, I will be limited with the amount of frequencies that I can analyze from this signal.

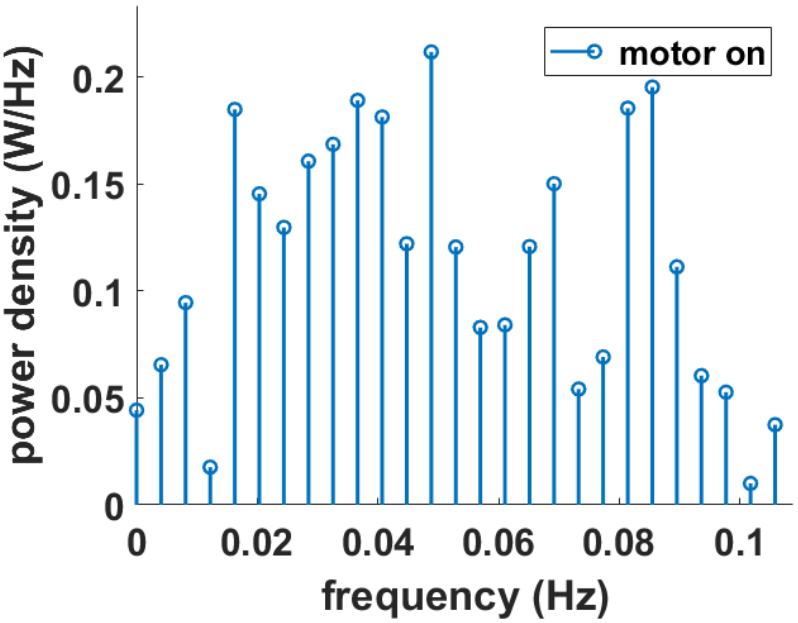

Fig. 6.18 Low frequencies and amplitudes of the acceleration signal (down) when the drone is at rest but with motor turned on

Also note that with the drone at rest and no vibrations, the recorded down value is ~0 m/s² instead of ~-9.8 m/s², which is just a matter of calibration in order to only show the specific force. I can still find out what the value of g is that the INS/GNSS is calibrated to by looking at the data of 'g' recorded by this instrument while the drone is at rest. On figure 6.19 I've plotted the down acceleration against the value of g and I can see the INS/GNSS is calibrated with g = 9.8035 m/s². Using the WELMEC formula I find a value of g ~ 9.78 m/s² for this latitude and altitude so this value is not correctly calibrated, however since we're only interested in the gravity anomalies and not the absolute value of gravity, this default calibration is not an issue.

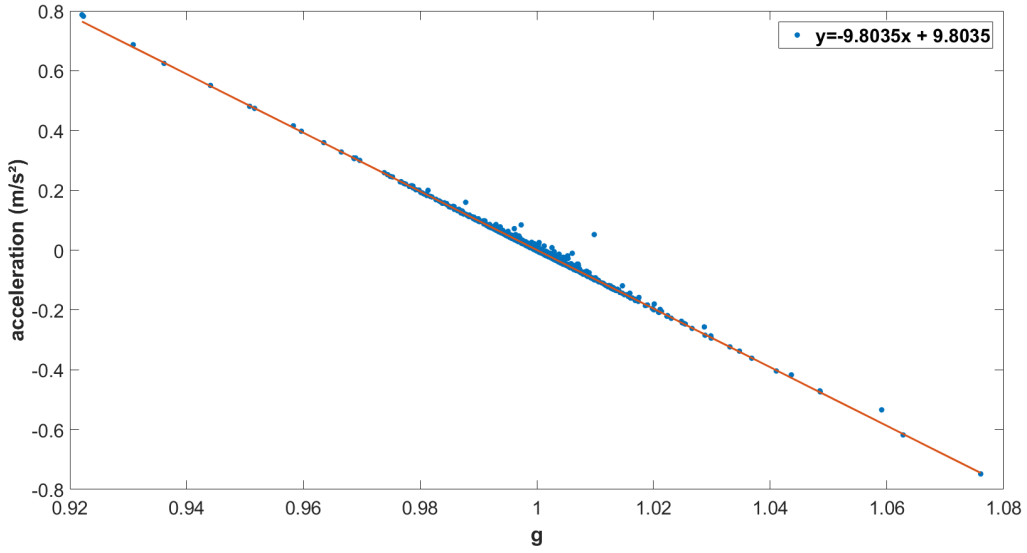

Fig. 6.19 The values of the acceleration (z-axis) recorded when the drone is at rest plotted against the values of g recorded for that period, with the best linear fit included

Seeing the influence of the vibrations of the motor on our accelerometers and the fact that accelerometers will always record high amounts of noise, the raw data will need to be filtered extensively.

6.7 Analysis of complete flight

Next I would not just consider singular straight lines, but the complete flight data. Because the complete flight was contained in a grid of 2x2 km and with an average flying speed of 30 m/s if I filter at 120s, my spatial resolution would be 1,8 km, approximately the height and width of the grid. This is where I would use the DEM

data that I presented earlier to confirm that the topography variations in this region would have almost no weight on the data from the accelerometers.

As mentioned before I have a total of 110990 recorded points, with the first 15 minutes being when the drone was being prepared and the last few minutes preparing for landing. Because of this when talking about the complete flight data I'll be using the points recorded from number 20000 to 90000.
Figure 6.20 shows the velocity and acceleration along the down axis obtained through derivation of the GPS data for these 70000 points of flight data that are considered.

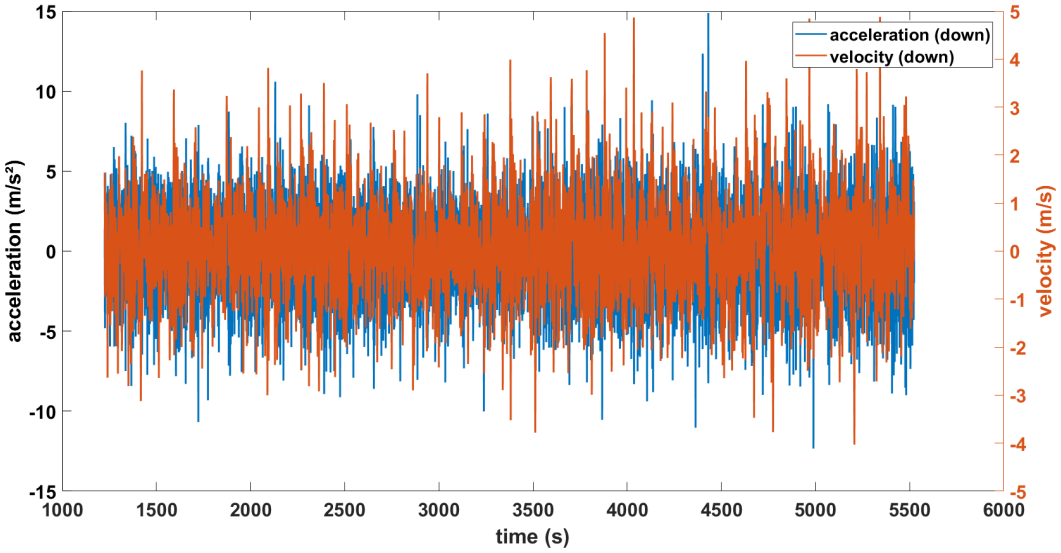

Fig. 6.20 Velocity and acceleration data obtained for the complete flight by taking the first and second derivative of the GPS data

6.8 Correction of rotations

Now that I take into consideration the complete flight data, which includes the turns, and the kinematic accelerations that are calculated in the NED-frame, it's important to apply the correction for the changes in roll, pitch and yaw using a rotation matrix in order to work in the same frame for both accelerations.

An aircraft can rotate around three axes, the roll-, pitch- and yaw-axis. Because the INS/GNSS is attached to the drone, with its x-axis pointing towards the nose of the drone, its y-axis pointing towards the right wing of the drone and the z-axis pointing towards the undercarriage of the drone, the roll, pitch and yaw are the rotation

around the x-, y- and z-axis respectively. The values of these angles go from 0° to 360° when rotating clockwise.

By default the roll, pitch and yaw will give a value of 0° when the x-axis points towards the true North and the z-axis towards the center of the Earth. I can verify that these settings are correct by looking at two consecutive lines that took place in the middle of our flight that are almost perfectly horizontal (Fig. 6.21), meaning parallel to the equator. On the first line the drone is flying from right to left, so the yaw is at an angle of 270° (90° rotated counter-clockwise), with the sinus of this angle being -1. On the second line the drone is flying from left to right, the yaw is at an angle of 90° (90° rotated clockwise), so the sinus of the yaw is 1 (Fig. 6.22).

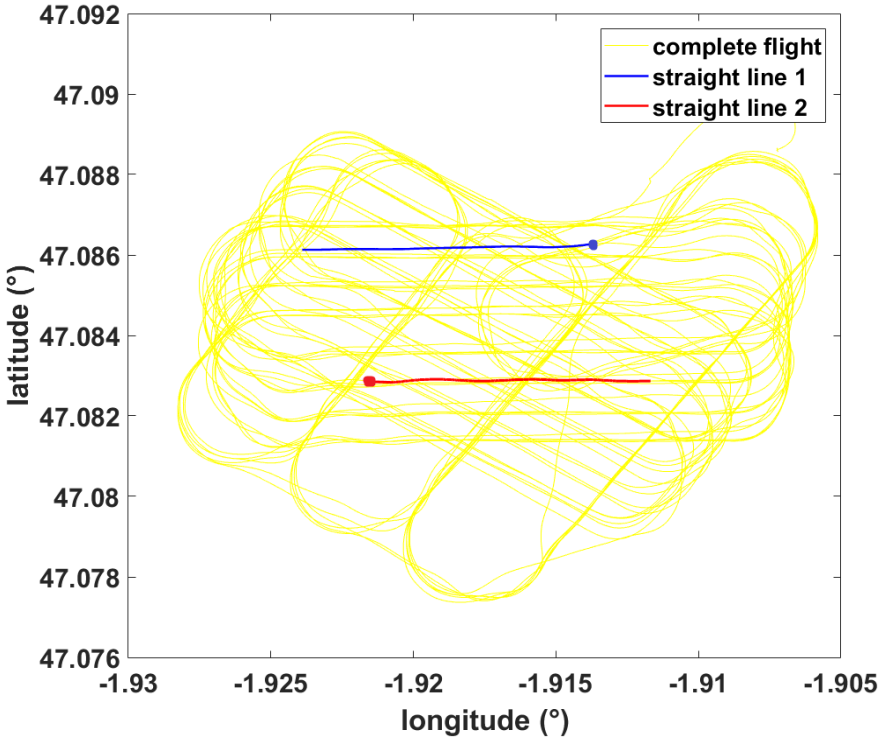

Fig. 6.21 Two consecutive straight lines, one from East to West (blue) followed by West to East

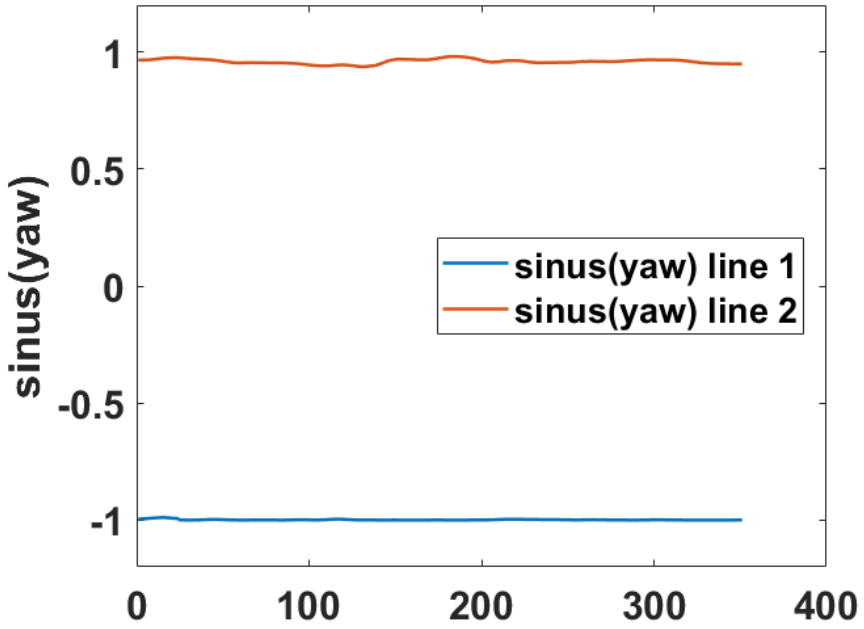

Fig. 6.22 The sine of the value of the yaw during the straight lines presented above

This can also be shown using the magnetic flux density measured by the 3-axis magnetometer, in the case below along the y-axis. The graph below presents (Fig. 6.23) the absolute value of the recorded data, as the data would be negative for a sine(yaw) that is 1 (INS/GNSS going from left to right, meaning y-axis pointing towards the south pole). The values of the magnetic flux density are higher than expected, which could be caused by interference of magnetic material in the payload, for example the magnet under the GPS antenna or the need of a magnetic calibration.

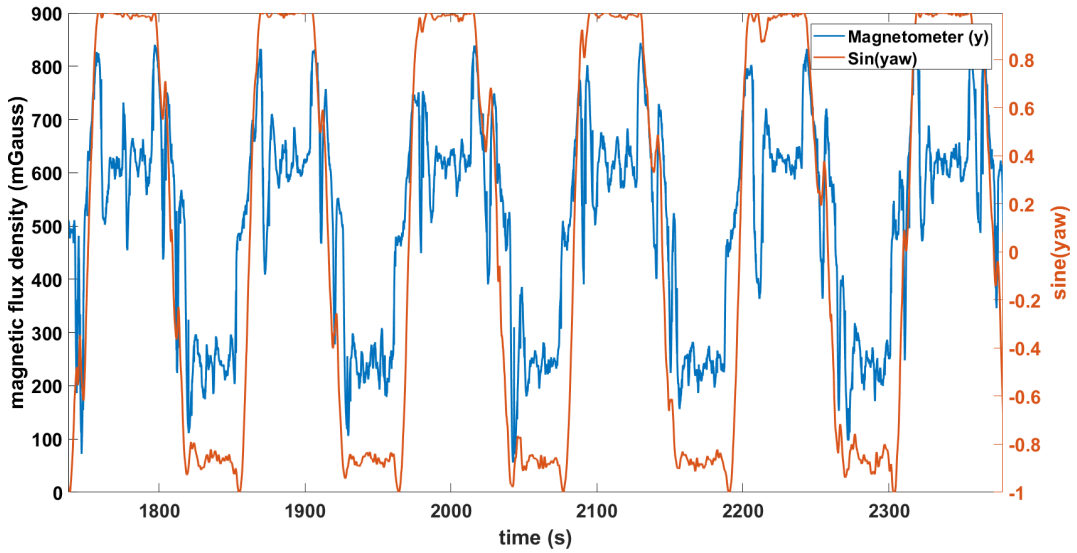

Fig. 6.23 Magnetic flux density (mGauss) and the sine of the yaw during part of the flight

If a rotation takes place around only one axis, called a basic rotation, a basic rotation matrix can be used to describe the rotation of the vector along the angle θ. The following matrices (Fig. 6.24) are used to describe a basic rotation of roll (x-axis), pitch (y-axis) and yaw (z-axis), respectively.

$$R_z(\gamma) = \begin{bmatrix} cos\,\gamma & sin\,\gamma & 0 \\ -sin\,\gamma & cos\,\gamma & 0 \\ 0 & 0 & 1 \end{bmatrix}$$

$$R_y(\beta) = \begin{bmatrix} cos\,\beta & 0 & -sin\,\beta \\ 0 & 1 & 0 \\ sin\,\beta & 0 & cos\,\beta \end{bmatrix}$$

$$R_x(\alpha) = \begin{bmatrix} 1 & 0 & 0 \\ 0 & cos\,\alpha & sin\,\alpha \\ 0 & -sin\,\alpha & cos\,\alpha \end{bmatrix}$$

Fig. 6.24 Rotation matrices for singular axis (elemental rotations)

If I take for example a vector that is aligned with the z-axis and rotate 90° around the x-axis (roll), that vector will now be aligned in the opposite direction of the y-axis of the INS/GNSS, which I also see using the basic matrix associated with the roll.

$$R_x(90°)\begin{bmatrix} 0 \\ 0 \\ 9.8 \end{bmatrix} = \begin{bmatrix} 1 & 0 & 0 \\ 0 & cos\,90° & sin\,90° \\ 0 & -sin\,90° & cos\,90° \end{bmatrix}\begin{bmatrix} 0 \\ 0 \\ 9.8 \end{bmatrix} = \begin{bmatrix} 0 \\ 9.8 \\ 0 \end{bmatrix}$$

During an actual flight the drone won't rotate along one axis at a time, but all three at once, even when not turning due to vibrations or wind. To correct for those rotations I will multiply by the rotation matrix obtained by multiplying those three basic rotation matrices. (Ch. 2.2.1)

6.9 Low-pass filter on complete flight data

When these accelerations are rotated to be in the same frame as the kinematic accelerations I apply a low-pass filter (120s) to both these sets of data. I will also use the data of the drone at rest but with the motor turned on, to decompose that signal in its frequency domain, however in order to compare its frequencies with those of the other two signals, which are much longer, I need to apply an interpolation to the data.

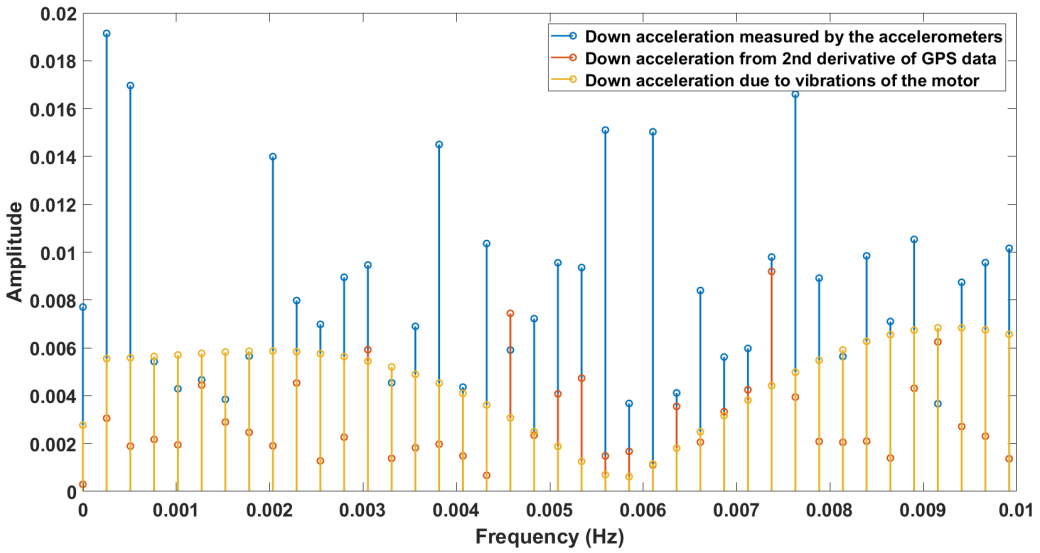

Fig. 6.25 Frequency domain for the low frequencies of the down accelerations (measured and calculated) during the flight and the accelerations caused by the motor (interpolated data)

Figure 6.25 is the single-side amplitude spectrum for all three signals. This spectrum allows us to compare the signals' frequencies and find what signal is responsible for a frequency of our signal obtained by the accelerometers. I see that the amplitude of the frequencies from the signal measured by the accelerometers is higher than each frequency of the signal that was obtained through derivation. This is to be expected since this graph presents the absolute values of the amplitudes and the signal from the accelerometer encompasses everything that has an influence on the total acceleration, while the acceleration obtained from the GPS data is only one part of it. This should also be the case for the acceleration due to the motor, but isn't the case. This is because the data was interpolated, so some of the amplitudes of those frequencies are only an estimate. If I had a signal with the drone at rest and the motor turned on with the same duration as the actual flight, I would see that the amplitude of each frequency would be lower than that measured by the accelerometers.

From here I will subtract the amplitudes of the acceleration measured by the accelerometers with that of the derived acceleration and the acceleration from the motor, while also still filtering with a low-pass filter of 120s. For the frequencies where the amplitude from the motor is higher than the accelerometers I will set them

to 0, because those frequencies are from the vibrations caused by the motor. Then I will perform an Inverse Fast Fourier Transform to reconstruct the reduced signal to obtain figure 6.26.

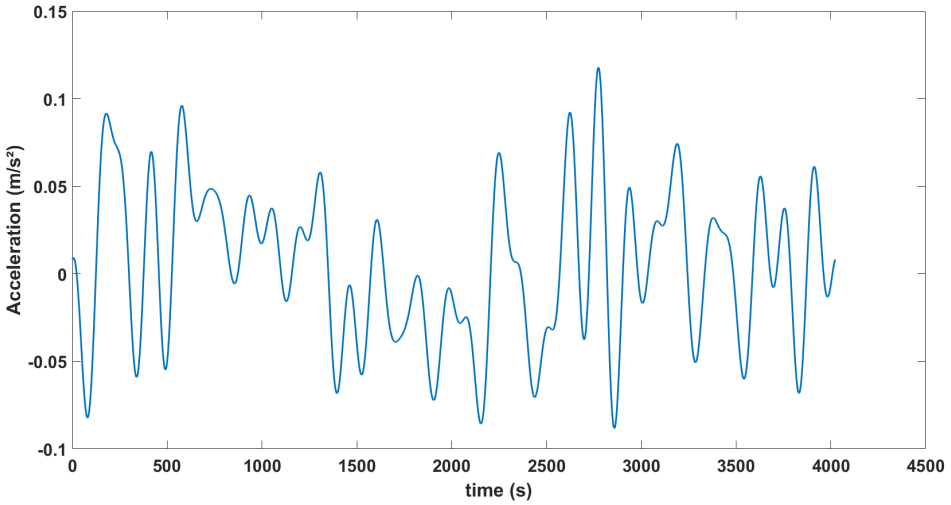

Fig. 6.26 Remaining acceleration signal after removal of the kinematic acceleration and the vibration signal caused by the motor for the flight data

I still have 54 local minimum/maximum values, with a maximum amplitude of +- 0.1 m/s². If I plot only the sinus of the yaw during the drone flight (Fig. 6.27), which will indicate when the drone turns, I can count 67 turns. Because these values are close to one another, this made me think that maybe the signals remaining could be due to the gyroscopes not being precise enough, since gyroscopes do suffer from high drift, which means when the rotation matrix used to correct the data during the turns isn't precise enough either.

In the annex an image is included to explain more clearly the different types of data obtained and what treatment was applied to each, before being combined together to obtain the remaining signal.

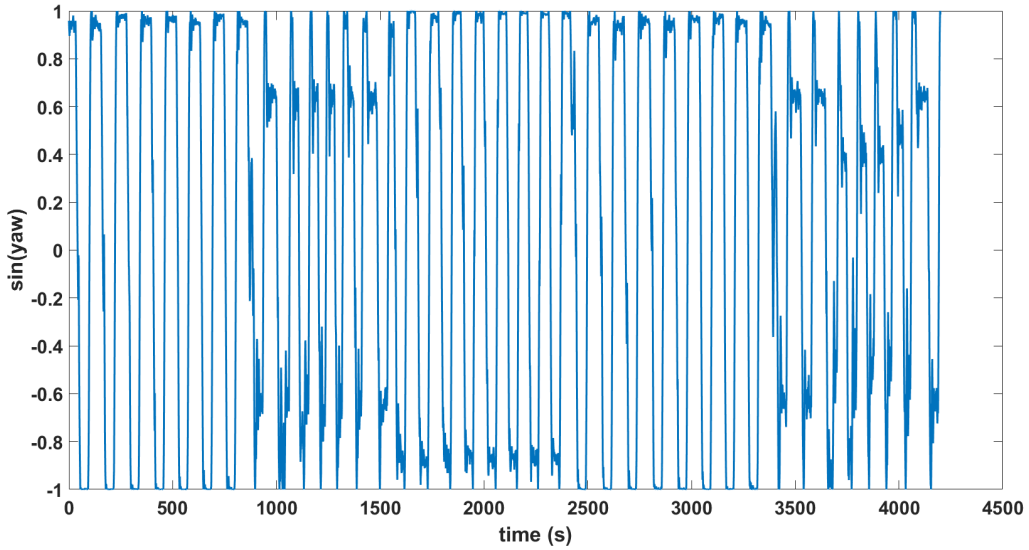

Fig. 6.27 Sine of the yaw values for the complete flight, showing how many times the drone changed direction

6.10 Analysis and filtering of only straight lines

To test this I decided to only consider the data when the drone is flying in a straight line. I would look at the variations in yaw and roll to apply a filter that removes the data where certain limits are passed. The values I decided on were obtained through trial and error because even on a relatively straight line, small changes in yaw, roll and pitch will occur.

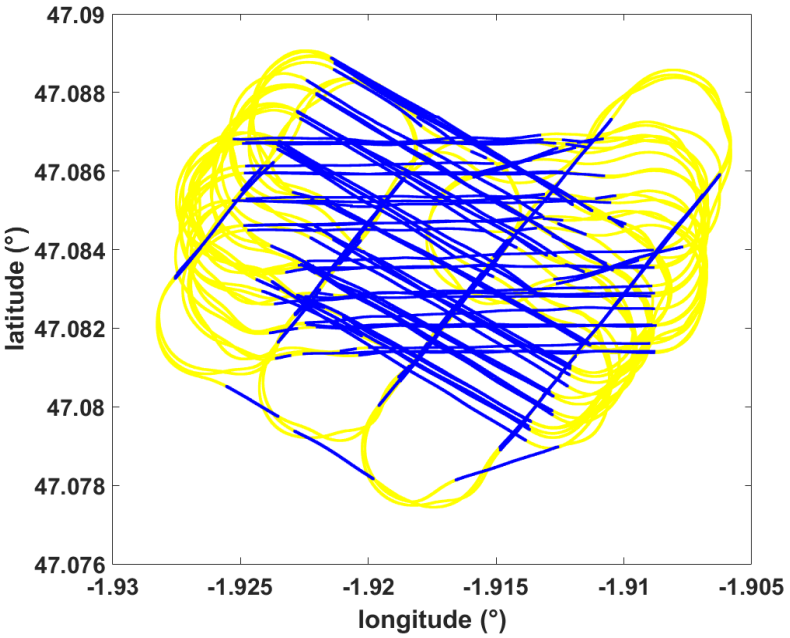

Fig. 6.28 Presentation of the complete flight (yellow) and the straight lines during the flight data (blue)

In figure 6.28 I present the data that is kept (blue) compared to the complete flight (yellow). On straight lines there would be a few consecutive data points that would be ignored due to slightly passing the imposed limits, if the amount of consecutive points was less than 25 (1,5 seconds) The points would still be considered.

Similarly during certain turns there would be a few points that would be included because the yaw/roll would be just below the limits, in which case they would be eliminated if the amount of consecutive points was less than 25. I can see that the parameters I used are effective and accurate because the blue points are almost exclusively the long straight lines.

By creating an array of the index points of the data points from the INS/GNSS that I keep, I can filter the data that I had calculated as well so the corresponding data is being kept, like the velocity and acceleration derived from the GPS data. This way I can apply the same method as before, using the acceleration measured by the INS/GNSS and that derived from GPS data to obtain a reduced signal. The result is shown below together with the altitude data that was kept (Fig. 6.29).

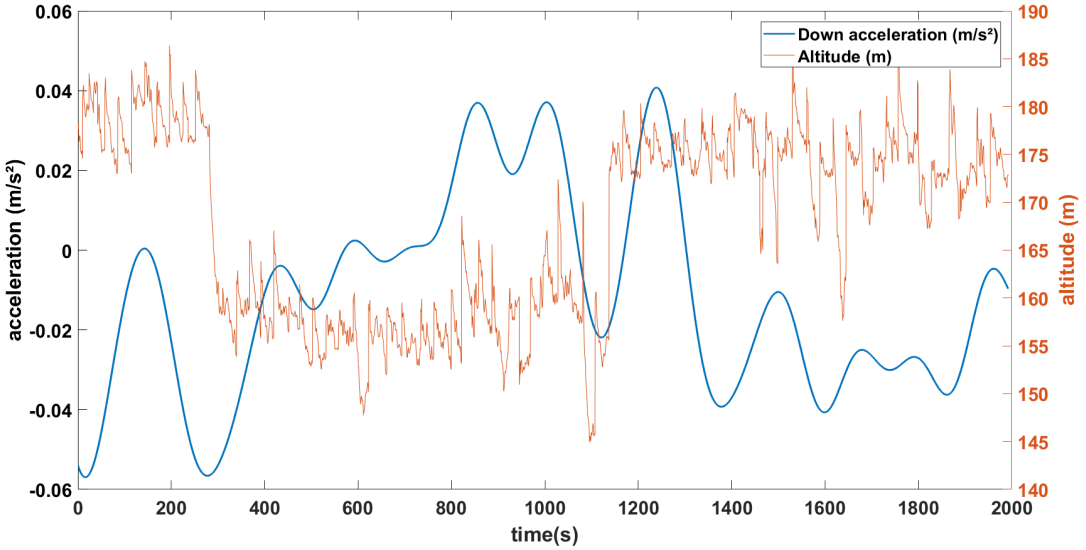

Fig. 6.29 Remaining acceleration signal (blue) after removal of the kinematic accelerations and those from the vibrations caused by the motor, when only considering the straight lines and the altitude (red) for the considered data

The length of the data is only half of the complete flight I considered before, so the drone was actually only flying straight half of the time. Compared to the signal of the complete flight, proportionally there are much less high amplitude changes in this remaining signal. This does confirm that the turns are a big source of the remaining signal because of the lack of precision of the rotation matrix over time because of the drift of the gyroscopes.

The actual amplitude variations are also lower, the highest change being only 0.08 m/s² versus 0.2 m/s² before. I can also see the acceleration being lower when the drone is flying at a higher altitude and higher when flying at a lower altitude. This is to be expected because of the free-air anomaly because the further away from Earth, the lower the gravitational pull will be. However this change is only $0.3085\ mGal$ for every meter of altitude above Earth's surface. At an altitude of 175 meters (average altitude of the last part on the graph above) the theoretical free-air anomaly is $52.4\ mGal$ or $52.4 * 10^{-4} m/s^2$ and the difference in free-air anomaly when flying at 157 meters (average value of the middle part) versus 175 meters is $5.553\ mGal$. The difference in average value for the acceleration during the first part at 157 meters and second part at 175 meters that I obtained is $31 * 10^{-4} m/s^2$ or $31\ mGal$. This value is still 6 times higher than the expected theoretical value.

These high amplitude changes are mostly aligned with the high altitude changes (passing between the 160 and 180 m altitude), so the origin of this remaining noisy signal is from the high acceleration change that happens when the drone quickly ascends or descends and the INS/GNSS not measuring this change accurately enough and this change induces a drift. Another source of the remaining signal is that even on straight lines there will be high changes in the pitch of the drone, which was not one of the parameters to filter out the turns and due to the gyroscopes' drift are not corrected completely with the rotation matrix.

Figure 6.30 shows just how much the pitch also changes on a straight line. On this graph when the pitch drops below 0°, the altitude decreases, when the pitch is higher than 0°, the drone ascends (it is possible for an aircraft to have a positive pitch but still descend, if it's speed is low enough eg. a plane that's landing).

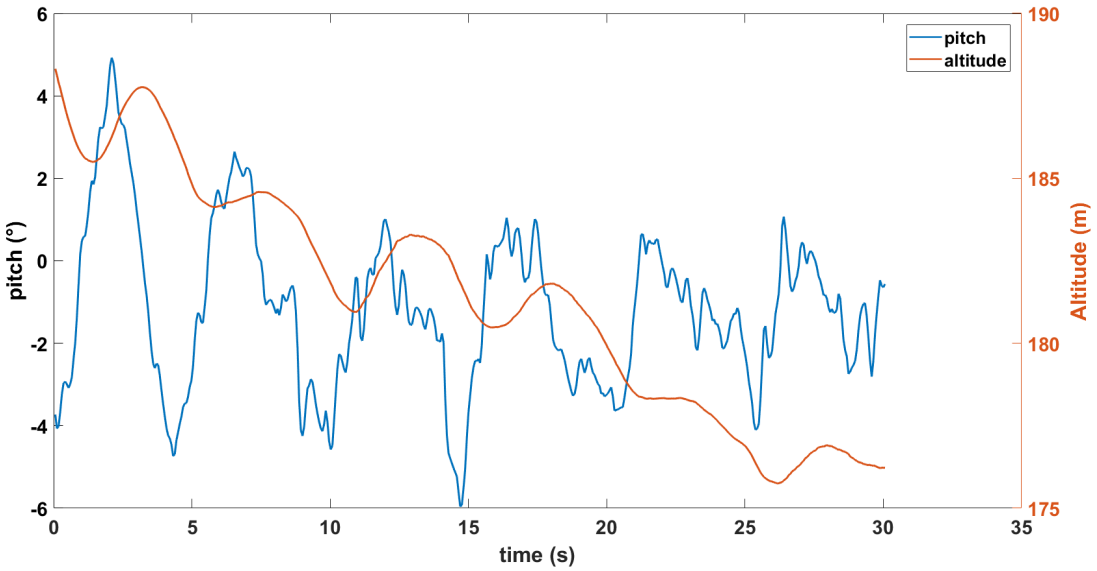

Fig. 6.30 Pitch (blue) and altitude (red) for one straight line

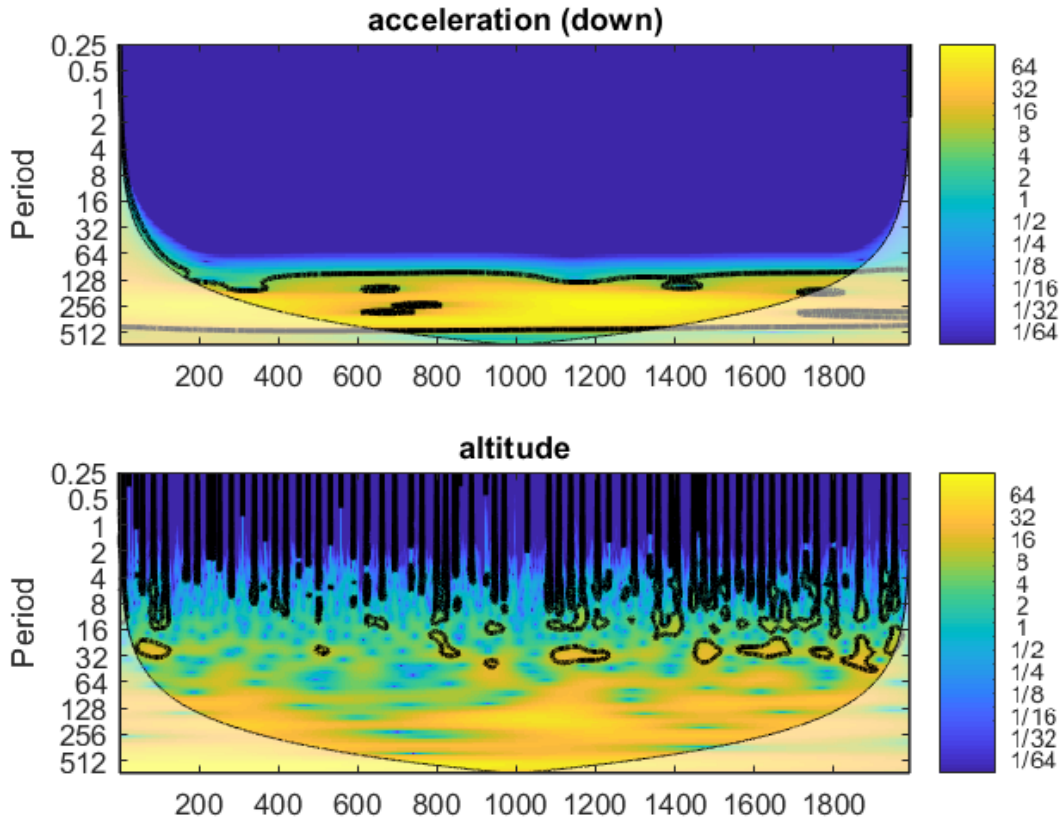

Fig. 6.31 CWT of the down acceleration and altitude. The CWT of the acceleration shows no signal for periods lower than 120 seconds as the data was filtered at 0.0083Hz (120s).

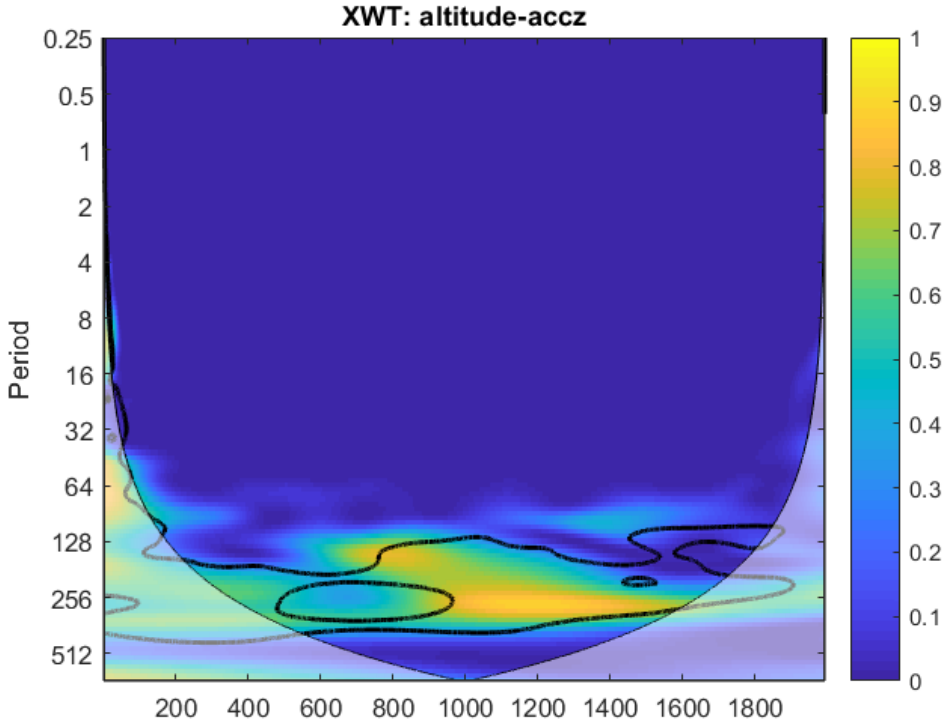

Fig. 6.32 XWT of the altitude and remaining (down) acceleration signal

The CWT (Fig. 6.31) and XWT (Fig. 6.32) show a correlation between the altitude and the remaining signal of the acceleration (down) for the periods at 120 seconds and higher. There is no correlation for the periods lower than 120 seconds as the acceleration was filtered with a low-pass filter of 120s.

6.11 MOTUS IMU on the drone

One of the MOTUS IMU was also included in the drone's payload. I can use its data to look at the recorded accelerations for comparison with the SPATIAL data, but the disadvantage is that the MOTUS does not record GPS data, which is necessary for the kinematic updates.

By simply plotting both down accelerations I barely distinguish the difference between both signals (Fig. 6.33) so I will select more precise windows, which are randomly selected throughout the fight, to see if there is any increase in drift later on.

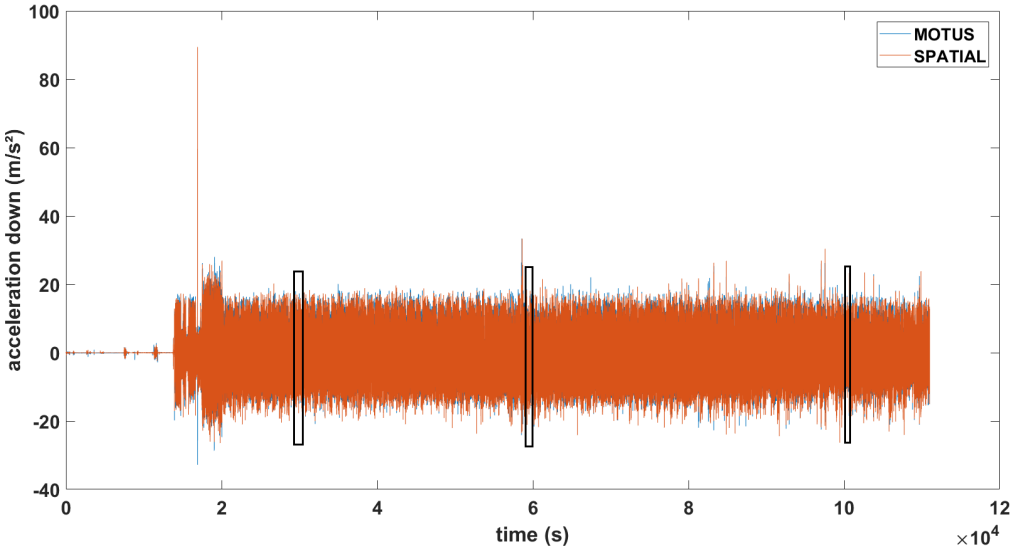

Fig. 6.33 SPATIAL (red) and MOTUS (blue) down acceleration for the complete flight, black rectangular represent the windows for the graphs below (in that order)

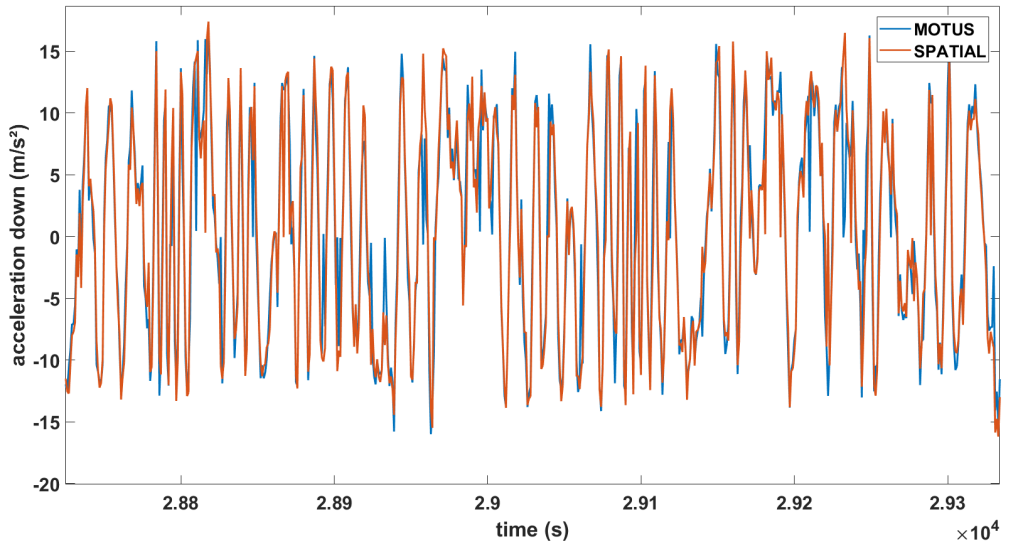

Fig. 6.34 Zoom of the (down) acceleration recorded in window 1 on Fig. 6.33

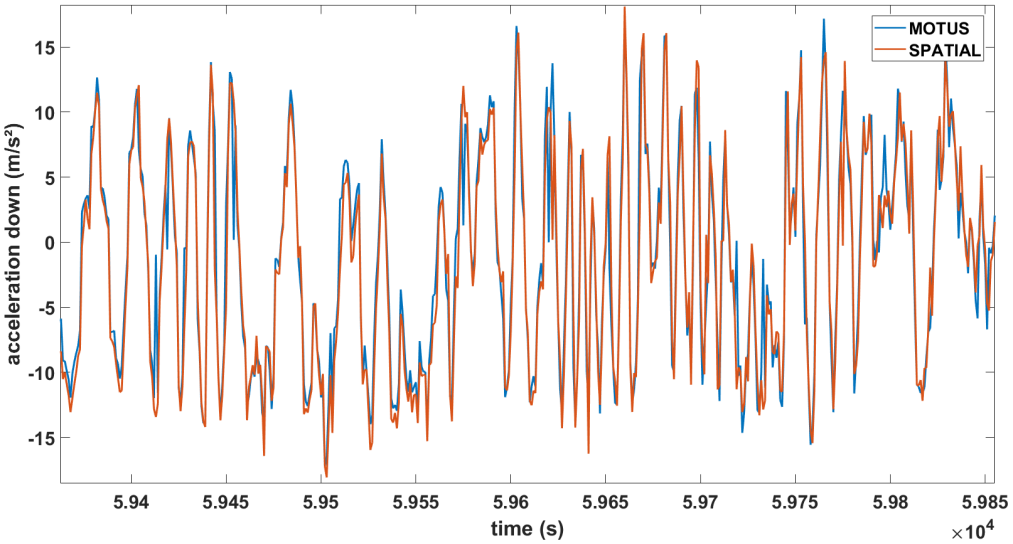

Fig. 6.35 Zoom of the (down) acceleration recorded in window 2 on Fig. 6.33

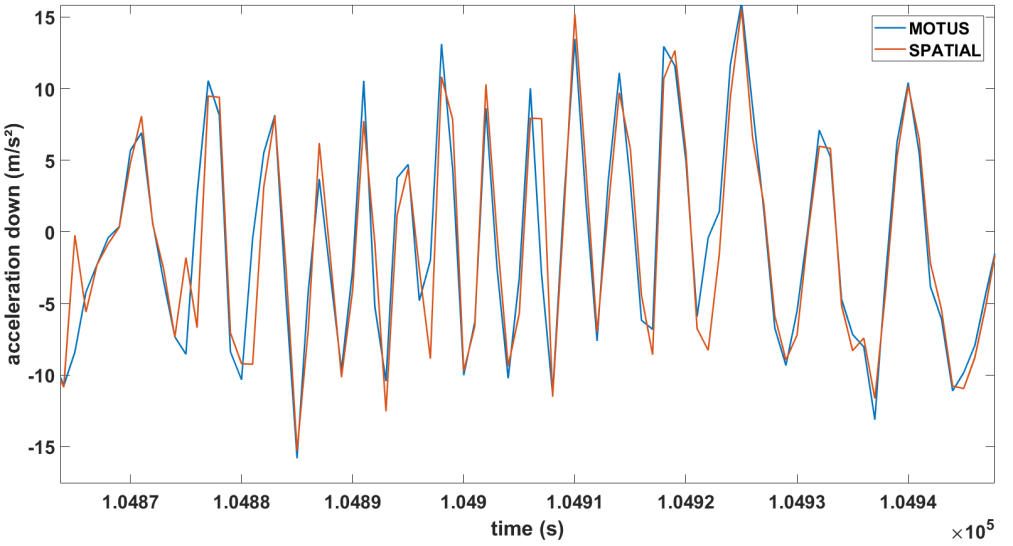

Fig. 6.36 Zoom of the (down) acceleration recorded in window 3 on Fig. 6.33

From these three windows (Fig. 6.34, 6.35, 6.36) I learned two important things. Firstly, the temperature bias correction of the SPATIAL data was correctly performed as both the SPATIAL and MOTUS accelerations line up very close to in both amplitude and time and I know the MOTUS has little to no distinguishable temperature bias, this also shows they have a very similar accuracy. Secondly there appears to be no drift in the data as both signals are still synchronized in the last window which is near the end of the flight.

When I break down both the MOTUS and SPATIAL acceleration (along their z-axis) signals into their frequency domain (Fig. 6.37), I obtain similar amplitudes for all frequencies, and most importantly for the low frequencies that are kept with the low-pass filter of 120s.

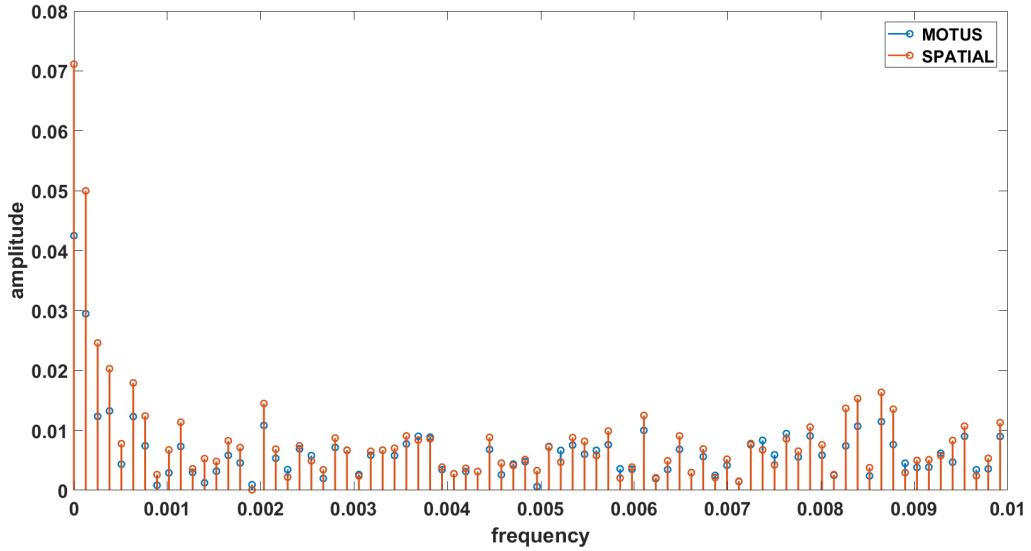

Fig. 6.37 Low frequencies and corresponding amplitudes for the acceleration (z-axis) signals of the MOTUS and SPATIAL

The same can be done for the angular velocity (x, y and z) for both SPATIAL and MOTUS and shows the same results; no drift between both signals, the same recorded amplitudes that are synchronized. Examples of this will be included in the annex.

The correlation between the acceleration signal of the MOTUS and SPATIAL is 90.1%, but even with such a high correlation, when I subtract both signals from one another I would expect a signal centered around 0 m/s² with very low amplitude changes. In reality when I only watch a small window of that signal I can see it is centered around 0 m/s² but still shows large amplitudes. When I try to look for gravimetric signals, even with such a high correlation, these amplitudes are still too high and are why these signals obtained during this airborne gravimetry experiment are not precise enough yet for gravimetric purposes.

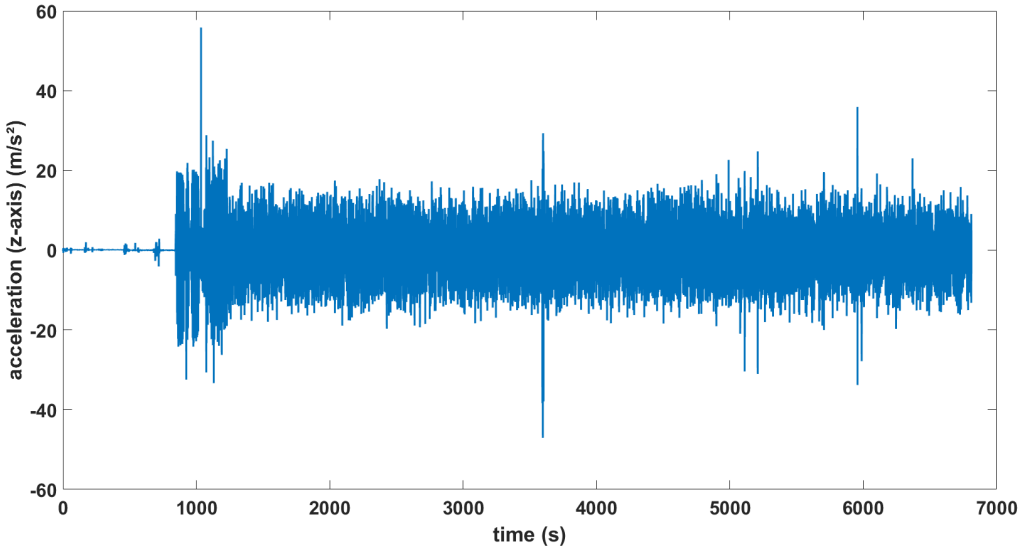

Fig. 6.38 Acceleration signal when subtracting the SPATIAL and MOTUS signal from one another

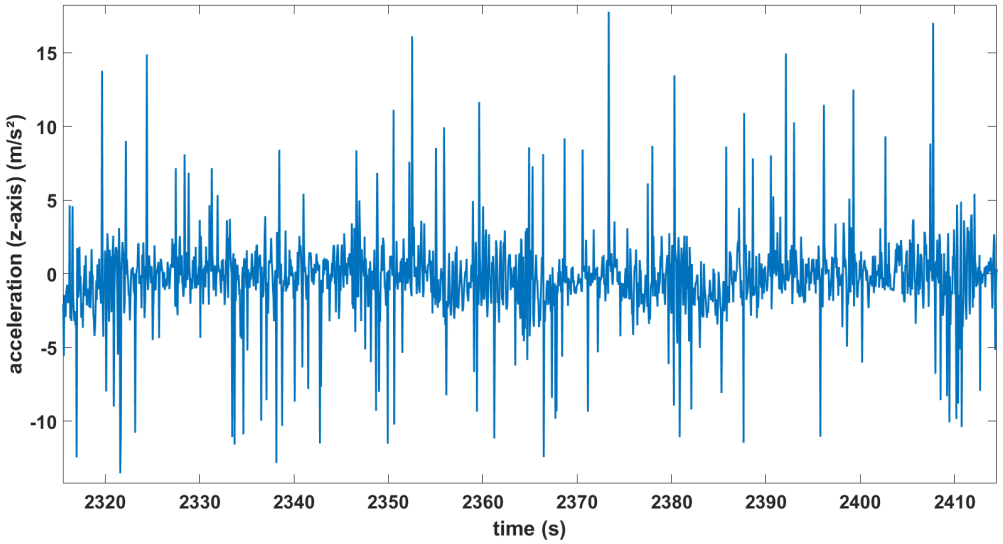

Fig. 6.39 Zoom of the previous signal

A second MOTUS IMU was included in the payload, except this one was set to a different sampling frequency of 1000Hz. As I saw with previous experiments where the sampling frequency was set much higher, there is an increase in noise levels, which I also see this time (Fig. 6.40). But even more importantly I see the presence of a drift that becomes bigger as the flight goes on. During testing I had noticed as well that if a computer/USB-port is used that is not optimized for high sampling frequencies, there would be a buffering that causes an ever increasing drift in the samples. After a 1000 seconds since startup there is a drift of 20 seconds (Fig. 6.41), in the middle of the flight this drift has increased to 80 seconds (Fig. 6.42) and

at the end the drift reaches 150 seconds (Fig. 6.43), this corresponds to roughly 20 seconds of drift for every 1000 seconds of recording. Even though the IMU has a higher sampling frequency and does not record GPS data, I could have used the GPS data of the SPATIAL and a moving average of the MOTUS accelerations to correct the kinematic accelerations, however because of this drift that becomes impossible.

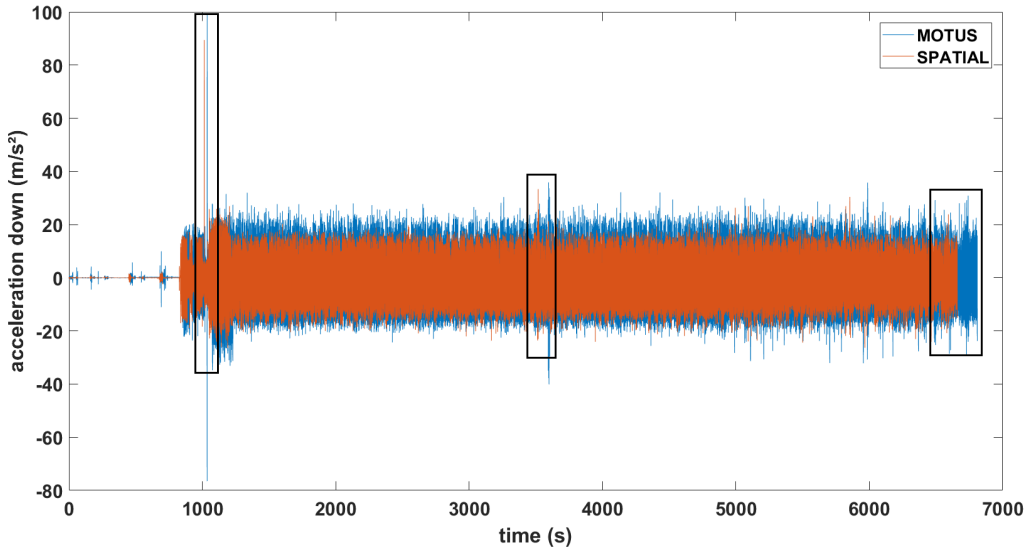

Fig. 6.40 Acceleration (down) of the MOTUS (blue) and SPATIAL (red) with a visual presentation of the three selected windows to display the ever increasing drift.

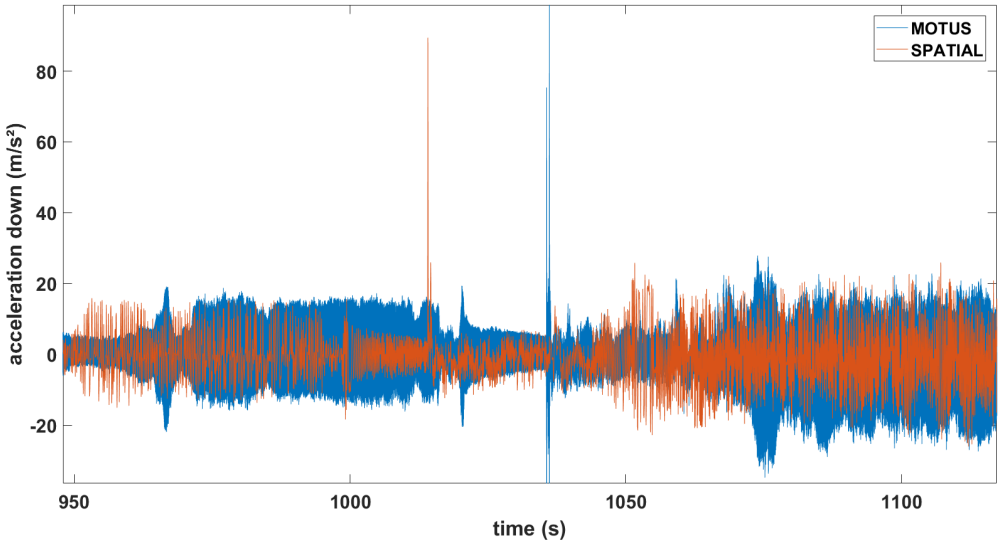

Fig. 6.41 Zoom of the (down) acceleration recorded in window 1 on Fig. 6.40

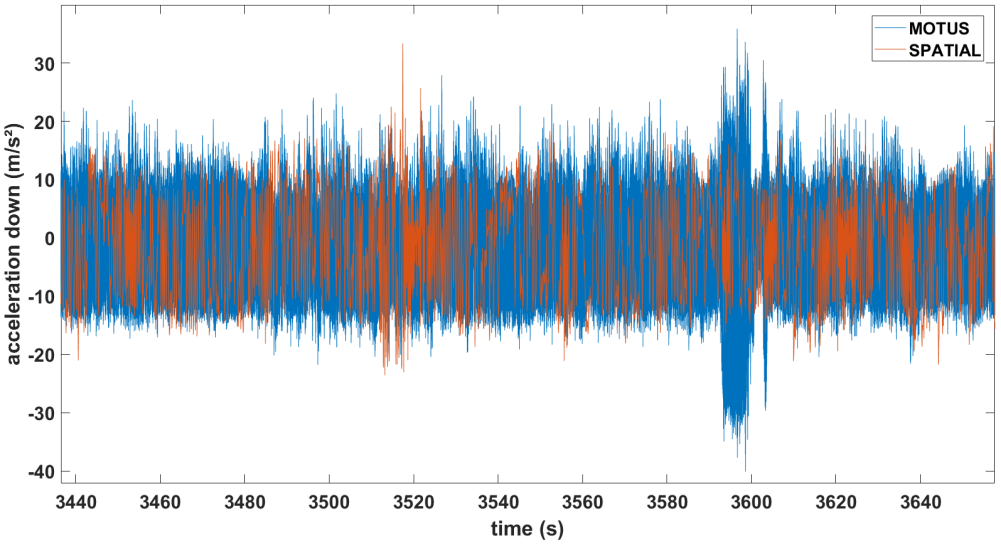

Fig. 6.42 Zoom of the (down) acceleration recorded in window 2 on Fig. 6.40

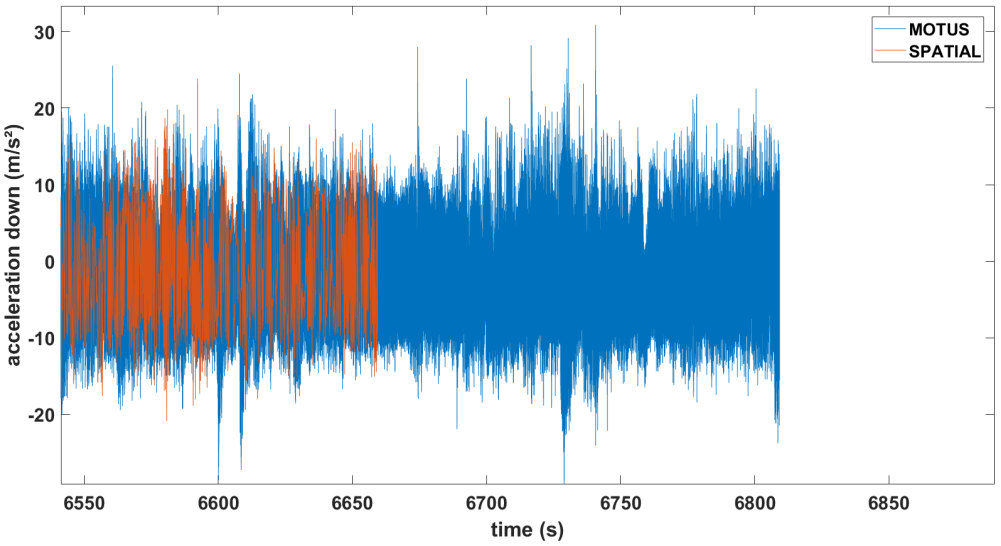

Fig. 6.43 Zoom of the (down) acceleration recorded in window 3 on Fig. 6.40

Airborne gravimetry being the ultimate goal using this system, proved to be tricky as the platforms subjected, but also responsible for a lot of vibrations with the presence of onboard instruments, generator and motor. This is much less of a problem in static land gravimetry. In the final chapter multiple propositions will be given to reduce the noise and improve precision. The results already obtained prove that using this system for geodetic applications, like detection of groundwater, will be possible in the future. Some of the regulations mentioned earlier to fly a drone also limit this study, for example the limitations on the altitude and distance that can be flown. To validate

the use of this system to detect aquifers, a study can be done near an area (for example river) that changes greatly in volume between different seasons. If these changes can be detected by the INS, it should validate the use in the field for the detection on the presence of groundwater.

CHAPTER 7 Discussion of the innovative aspects of this thesis work

Firstly, for static experiments a gravimeter would normally be used to study gravity variations on the surface of the Earth. They will give precise readings but the instruments are heavy and expensive. On the other hand an INS/GNSS is normally used for positioning, its accelerometric data is used to increase the precision of the GNSS positioning with the use of a sensor fusion algorithm (usually based on a Kalman filter), but during my thesis work an INS/GNSS was used for the opportunistic method of considering the measured accelerations for gravity applications. This is not a new concept as mobile gravimetry has used INS/GNSS in the past (either strapdown or on a stabilization platform) but what has not been explored much before is using a MEMS INS/GNSS for this, which will be much lighter, low-cost and easier to install than a traditional INS. This type of INS/GNSS, installed on a mobile platform, will come with more noise, caused by different factors (MEMS INS/GNSS error, wind and turbulence, thermal drift, motor residual vibrations, etc.) but by recording enough data in static mode and applying the empirical corrections to remove for example the thermal drift (Ch. 3.2), I was able to obtain precise results. The thermal drifts obtained for the two different SPATIAL, with the temperatures ranging from 32 to 38°C during those experiments (laboratory and Cammazes dam experiment), were $-6.2 * 10^{-3} m/s^2/°C$ and $-2.14 * 10^{-4} m/s^2/°C$, which is a much stronger thermal drift than that of a gravimeter, underlying even more so the importance of studying the thermal influence of these instruments. For a CG-5 gravimeter this thermal drift is $-5\, nm/s^2/°C$, much lower than that of the INS/GNSS, which is to be expected since the spring is placed in a vacuum chamber so it is in a controlled environment which protects it from external temperature variations. If we want to reduce the effects of external temperature variations on the INS/GNSS recordings we need to place it in a controlled environment. One such environment would be in a cave where naturally the temperature varies less (12-14°C). This gravimeter thermal drift is not to be confused with the daily drift of the gravimeter, which was ~1 mGal/day for our experiments.

Correcting the data from the Cammazes dam experiment I showed that the INS/GNSS, just like the CG-5 gravimeter, shows the variation in gravity when the altitude changes (~400 m altitude difference) (Ch. 5.4). This was also shown with the MOTUS IMU, which unlike the SPATIAL did not present a high thermal drift at those temperature ranges (28-36°C), for much smaller altitude variations (<10 m) at the laboratory (Ch 3.4).

Which brings me to the second innovative part of this work. I was able to attain a high enough precision to present the influence of the altitude variations on the gravitational acceleration (<5 mGal). Even more, I attained sufficient precision to obtain the acceleration signal caused by the solid Earth tides (< 1 mGal).

From the XWT of the corrected INS/GNSS and Tsoft data and thanks to a low-pass filter I obtained a good correlation (0.84) between both the theoretical and INS/GNSS signal (Ch. 4.4). Although the amplitudes did not fit completely with that of the theoretical model (RMSE 405 nm/s²), which is due to different factors of lesser amplitude (ocean loading, atmospheric pressure, etc.) the result was still extraordinary because we recorded for the first time the solid tides with such an instrument and we even noticed the effects of atmospheric pressure changes on our data.

The third innovative part of this work is the drone that was used for airborne gravimetry. Because of the small size of this MEMS INS/GNSS (4.1 x 3.0 x 2.5 cm), it was easily installed in a fixed-wing single rotor drone and not a plane or military grade drone as some of the previous studies used (Lin et al., Luo et al.). The drone, “Boreal LAB”, made by Boreal was adapted specifically for scientific measurements. It can fly continuously for as long as 8 hours, even though a duration that long is not needed or even beneficial for our INS/GNSS, because we wish to limit the temperature variation because of the previously discussed thermal drift.

Our results (25 mGal precision) are not at the desired precision (<5 mGal) yet for airborne gravimetry, Lin et al. & Luo et al. obtained a 4 mGal and 0.35 mGal precision respectively during their airborne gravimetry. Even though those studies used different equipment and bigger platforms, from the results obtained during our

static experiments I believe a higher precision can be obtained for mobile experiments with this INS/GNSS. Through extensive low-pass filtering and only considering the data from straight lines I did obtain a result that presents a correlation between the change in residual acceleration and the change in altitude. However the difference in average value of the acceleration (31 mGal) between both altitudes (18 meter difference) is still five to six times higher than the theoretical value (5.5 mGal). The precision can definitely be greatly improved, for example using a gimbal for INS/GNS stabilization. By placing the INS/GNSS on a gimbal, part of the imprecision of the gyroscopes can be reduced drastically. Temperature variations throughout the flight were also a factor to take into account. Although the temperature variation is lower than the static experiments, mainly because of the duration of the experiment, a possible solution would be for a controlled airflow during the flight to reduce heating of the INS/GNSS.

The ultimate innovative idea of using this system, and why the desired precision is <5 mGal, involves the installation of such a MEMS INS/GNSS on a small drone and use the acceleration data for the detection of the presence of aquifers or study the evolution of the phreatic zones. A drone, with similar size to the one used for my studies, can be swiftly deployed across various regions, allowing for efficient data collection. By utilizing the acceleration data, we can detect the presence of aquifers or study the evolution of phreatic zones.

To validate the feasibility of this innovative idea, an initial step would involve gathering data from a region that experiences extreme droughts as well as periods of heavy rainfall. Such a region offers a stark contrast in soil density, presenting the ideal conditions for detecting alterations in gravitational acceleration. By comparing the recorded data from different time periods, it becomes possible to identify any significant changes indicative of variations in the phreatic zone.

Overall, the innovative utilization of a MEMS INS/GNSS system on a small drone holds immense potential for revolutionizing the study and management of aquifers. By leveraging acceleration data and conducting extensive field investigations, scientists can uncover valuable information about the phreatic zones and water

availability in different regions, ultimately leading to more sustainable and efficient water resource utilization.

CHAPTER 8 Conclusion et perspectives (français)

Tout au long de ce travail de thèse, de nombreuses expériences différentes ont été réalisées et celles qui ont donné les résultats les plus fructueux ont été présentées.

La première étape de mon travail de thèse a été de modifier un logiciel permettant de sélectionner les données à tracer par l'INS avant de les acquérir et de les sauvegarder dans deux fichiers texte distincts. J'ai ensuite pu tester le programme d'acquisition en conditions réelles lors de la première expérience. La première expérience, en conditions protégées au laboratoire GET, où l'objectif était de se familiariser avec les logiciels et le matériel du SPATIAL, a donné des résultats clairs sur le biais de température à prendre en compte pour toutes les expériences futures et l'influence des différentes fréquences d'échantillonnage. Du fait de la durée de cette expérience j'ai pu ensuite utiliser ces données et celles enregistrées par un gravimètre relatif et les comparer au signal théorique des marées terrestres pour cette période aux coordonnées du laboratoire Géosciences et Environnement Toulouse. En regardant la périodicité des signaux à travers une cohérence inter-ondelettes, j'ai pu montrer que le SPATIAL INS/GNSS avait une périodicité cohérente avec les périodes semi-diurnes et diurnes des marées terrestres solides. J'ai obtenu les mêmes résultats avec le gravimètre CG-5, qui avait des données continues plus longues à la même fréquence d'échantillonnage où je pouvais même voir la périodicité du cycle lunaire bimensuel. En appliquant un filtre passe-bas au modèle théorique et aux données de l'INS/GNSS pour supprimer toutes les périodes inférieures à 10 heures (pour lesquelles le XWT n'a montré aucune corrélation), j'ai obtenu deux signaux hautement cohérents. Seule l'amplitude du signal INS/GNSS est inférieure à certaines périodes à celle du modèle théorique. Cela peut être causé par différents phénomènes comme la charge océanique ou les changements de pression atmosphérique. Quand j'ai regardé la pression enregistrée par l'INS/GNSS, il y a une diminution de la pression lorsque l'amplitude est plus faible. Bien qu'il soit

peu probable que le changement de pression atmosphérique soit à lui seul responsable de la différence d'amplitude complète, il en fera partie.

Quelques mois plus tard, pour poursuivre l'étude du biais de température, le matériau a été placé dans une étuve de séchage pour étudier le comportement à des températures plus élevées. La principale observation était que la dérive thermique du SPATIAL ne suit pas nécessairement la même loi linéaire à des températures plus élevées, mais à une valeur seuil, l'augmentation de la température peut avoir un effet inverse sur les accélérations enregistrées. Le MOTUS IMU n'a pas montré de biais de température clair par rapport au SPATIAL INS/GNSS. Ce qui signifie qu'il peut être utilisé comme référence pour les accélérations SPATIAL. Le MOTUS seul ne serait pas suffisant pour la gravimétrie mobile parce qu'il n'enregistre pas les coordonnées GPS car c'est une IMU.

L'expérience du barrage de Cammazes a eu lieu entre la période des première et deuxième expériences de biais de température, de sorte que l'IMU MOTUS n'était pas encore disponible à ce moment-là. Tout au long de cette expérience, nous sommes passés d'une altitude de 147 mètres au-dessus du niveau de la mer (GET) à une altitude de 580 mètres, avant de retourner au laboratoire, en montant et en descendant environ 430 mètres. Plusieurs arrêts ont été effectués pour acquérir des mesures avec le gravimètre CG5, qui a été utilisé comme instrument de référence. Un arrêt a été effectué à un point de référence IGN afin de transformer les mesures gravimétriques relatives du gravimètre en valeurs absolues. Une fois les mesures de tous les arrêts transformées en valeurs absolues et la dérive du CG5 corrigée, je vois bien l'influence de l'altitude sur les valeurs de gravité ; plus on est haut, plus on est éloigné du centre de la Terre, plus la gravité est faible car elle diminue d'un facteur $1/r^2$. Pour chaque mètre au-dessus de la surface de la Terre, l'attraction gravitationnelle diminue de 0,3085 mGal/m, mais cela suppose qu'il n'y a que de l'air entre vous et la surface, appelée à juste titre l'anomalie de l'air libre. Parce que ce n'est pas le cas lors de cette expérience car nous roulons sur la surface, l'anomalie que j'ai observée pour chaque mètre était plus faible.
En prenant les données d'accélération de l'INS/GNSS aux arrêts que nous avons effectués, et en appliquant une matrice de rotation pour corriger la position de l'INS/GNSS puisque nous ne serions jamais garés parfaitement horizontaux, je peux

la comparer aux données du gravimètre. J'ai dû étalonner la première valeur, au laboratoire GET, à la valeur absolue obtenue, car l'étalonnage était légèrement décalé. Lors du traçage de ces données, je vois plusieurs points où les valeurs de l'INS/GNSS ne correspondent pas étroitement au gravimètre, les points où cela ne se trouve pas également être les points où j'ai eu le moins de mesures. L'instrument avait une fréquence d'échantillonnage de 1/30 s, donc selon la rapidité avec laquelle je terminerais les mesures avec le gravimètre CG5, j'aurais plus ou moins de données. Lorsque je corrige le biais de température de ces données, les valeurs correspondent beaucoup plus à celles du CG5 et montrent également la loi linéaire entre l'altitude et la gravité.

Outre l'influence de l'altitude sur la gravité, l'itinéraire sélectionné a également été choisi afin de déterminer si je peux remarquer l'effet des changements de latitude sur la valeur de la gravité. En comparant l'anomalie de gravité lorsqu'il n'y a pas de changement de latitude, et les valeurs théoriques de la gravité à l'aide de la formule de WELMEC, j'ai montré que la différence d'anomalie de gravité lorsque la latitude change, correspond à la valeur théorique du changement de gravité pour une changement de la latitude d'environ 0° 1'.
C'est un très petit changement de gravité car le changement de latitude est si petit, donc je n'ai pu le détecter que pendant cette expérience en utilisant le gravimètre et non l'INS/GNSS.

Bien que l'INS/GNSS effectuait des mesures en continu tout au long de la journée et était utilisé pour la gravimétrie mobile, le gravimètre CG5 qui servait de référence ne pouvait pas le faire et des arrêts ont dû être effectués pour ses mesures. Pour cette raison, la prochaine expérience que je vais aborder est celle où les mesures continues de l'INS/GNSS ont été utilisées au lieu des seules périodes où le véhicule était au repos.

Pendant une période de 6 semaines, une expérience différente au laboratoire a été réalisée pour étudier à nouveau l'influence des changements d'altitude, mais cette fois des variations d'altitude beaucoup plus petites. Plusieurs instruments seraient utilisés et échangés entre un emplacement au rez-de-chaussée et le toit. Le gravimètre était à nouveau une bonne référence des changements de gravité

attendus et le MOTUS IMU, dont les résultats n'étaient pas influencés par les changements de température élevés entre les deux emplacements, a présenté des résultats qui étaient de la même ampleur que le gravimètre. Les seuls résultats qui n'avaient pas la précision souhaitée provenaient des périodes de perte de données ou de l'IMU qui était réglée sur une fréquence d'échantillonnage beaucoup plus élevée, augmentant trop son bruit.

Pour finir, une expérience mobile de gravimétrie aéroportée a été réalisée. Un drone à voilure fixe a été utilisé dont la charge utile maximale n'est que de quelques kilogrammes. Il s'agit d'un véhicule considérablement plus petit et plus léger que certaines des études précédentes répertoriées, l'objectif étant une solution plus accessible pour les régions difficiles d'accès tout en restant bon marché qui peut être rapidement déployé et couvrir une région.
L'INS/GNSS enregistre à la fois l'accélération sur trois axes et les coordonnées GPS, y compris l'altitude. En convertissant la longitude, la latitude et l'altitude en coordonnées cartésiennes, les dérivées première et seconde peuvent être calculées pour obtenir la vitesse et l'accélération le long des axes Nord, Est et Bas (le noyau de la Terre étant le centre). L'INS/GNSS étant fixé à l'intérieur du drone, cela signifie que son référentiel sera celui du drone et puisqu'il serait impossible pour le drone de voler parfaitement horizontal, en utilisant une matrice de rotation avec le tangage, le roulis et le lacet enregistrés par les gyroscopes, je peux convertir les accélérations le long des trois axes pour être également dans le même cadre de référence NED. L'accélération le long de l'axe descendant m'intéresse le plus car c'est aussi l'axe le long duquel la gravité tire. Avec les accélérations calculées et enregistrées dans le même référentiel, elles peuvent être soustraites l'une de l'autre pour ne conserver que l'accélération de la pesanteur.
En pratique, cependant, la quantité de vibrations du drone, causées par le vent mais aussi le moteur, ajoute trop de bruit aux données enregistrées par l'INS/GNSS, qui est attaché au drone. En raison de ce bruit élevé, les données doivent être filtrées en profondeur à l'aide d'un filtre passe-bas. Avec la vitesse du drone de 30 m/s, un filtre passe-bas de 120 secondes, similaire aux études précédentes, me donnerait une résolution spatiale de 1,8 kilomètres, la longueur et la largeur approximatives de la région. Grâce au modèle numérique de terrain, j'ai pu montrer le faible effet de la topographie de cette région sur le signal gravitationnel.

Dès la première analyse des données de vol complètes, j'ai suspecté la dérive des gyroscopes d'être trop élevée pour des corrections précises du cap du drone à l'aide d'une matrice de rotation, c'est pourquoi j'ai filtré les données complètes afin de ne garder que les parties où le drone volait en ligne droite, pour minimiser les imprécisions ajoutées par les gyroscopes du drone. Appliquer la même méthode que précédemment me donne un signal plus clair, où j'obtiens une corrélation entre l'accélération le long de l'axe descendant et les changements d'altitude tout au long du vol. Cependant, ce changement d'accélération est encore trop élevé pour les petites variations d'altitude et est plus susceptible d'être un résidu de l'accélération vers le bas lorsque ces changements d'altitude ont lieu. Néanmoins, compte tenu de la forte amplitude du bruit, que j'ai pu éliminer en partie en supprimant la densité de puissance des fréquences du signal lorsque le moteur était allumé mais que le drone était encore au repos, le signal restant a très peu changements d'amplitude et avec les améliorations futures, cette précision du signal pourrait être encore améliorée. Certains de ces changements et améliorations seront expliqués ci-dessous

Bien que la durée d'une heure pour le vol total soit bonne, puisqu'une grande distance peut être parcourue pendant ce temps et qu'elle limite le changement de température total, la trajectoire du vol devrait être différente. Au lieu de beaucoup de petits hippodromes à différents angles, le drone devrait voler plus loin pour augmenter la taille des hippodromes et minimiser les changements d'altitude à la fois sur la ligne droite et pour différents hippodromes. Bien qu'il y ait eu des raisons scientifiques pour que l'expérience de flux d'air utilise ces trajectoires, notre expérience aurait bénéficié d'avoir moins de facteurs différents qui pourraient influencer le signal gravitationnel.

L'INS/GNSS devrait également enregistrer pendant une période plus longue (30 à 60 minutes) avec le moteur allumé au repos, ce qui se traduirait par plus de données pour filtrer les amplitudes des fréquences dont il est responsable. Pour aider à réduire encore plus les niveaux de bruit des vibrations, une couche de caoutchouc plus épaisse pourrait être utilisée pour fixer les instruments.

Afin d'améliorer les données des accélérations dynamiques, une station au sol pourrait être utilisée pour le GPS différentiel (DGPS). Cela se traduirait par des données de longitude, de latitude et d'altitude plus précises, ce qui à son tour améliore le signal restant lorsqu'il est soustrait.

Pour les futures expériences statiques, l'INS/GNSS pourrait être installé dans un endroit isolé du bruit causé par la présence humaine et avec une plage de température plus constante. Par exemple, à l'intérieur d'une grotte, peut-être même à quelques mètres sous la surface du sol, où la température serait plus froide et moins variable (plage de température annuelle 12-14 °C) qu'à l'intérieur d'une pièce du laboratoire. L'absence d'activité humaine réduira également les vibrations enregistrées causées par la conduite des voitures, l'ouverture et la fermeture des portes, des personnes marchant à proximité ou le déplacement d'équipement, etc.

L'INS/GNSS pourrait également être testé à des températures plus basses (< 0°C) pour étudier l'effet sur l'accélération enregistrée. Bien qu'une plage de température inférieure à 0 °C ne soit pas réalisable lors d'expériences mobiles, cela pourrait être possible dans un laboratoire pour des expériences statiques si les températures froides ont un effet bénéfique sur les données.

Une expérience plus longue pourrait également être réalisée (30-60 jours), avec l'INS/GNSS et le gravimètre CG-5 enregistrant tous les deux en laboratoire à 1 mesure/minute, afin de voir si l'INS/GNSS peut détecter la périodicité des marées terrestres solides causées par le cycle lunaire bimensuel (comme observé sur les données CG-5 dans ce travail). Les amplitudes seraient plus faibles que celles causées par les cycles (semi-)diurnes, mais accentueraient encore plus les capacités de l'INS/GNSS, ou présenteraient ses limites.

En installant l'INS/GNSS près d'un lac, d'une rivière ou d'un canal qui présente de fortes variations de volume au fil des saisons. Si l’instrument peut détecter les petits changements de gravité causés par l'augmentation ou la diminution des niveaux d'eau, l'expérience pourrait prouver la possibilité de l'utiliser pour l'hydrologie, par exemple pour la détection d'aquifères.

Une expérience mobile pourrait également être réalisée avec l'INS/GNSS installé sur un cardan. Par exemple, une répétition de l'expérience du barrage de Cammazes, où l’INS/GNSS est fixé sur un cardan. Le cardan maintiendra l'instrument à niveau tout au long de la journée. En calculant les accélérations à partir des données de

navigation et en les soustrayant des données enregistrées par les accéléromètres, on obtient les accélérations résiduelles. Ces accélérations pourront être utilisées pour la détection des variations altimétriques et on ne sera pas seulement limité aux données lorsque la camionnette est à l'arrêt.

8.b Conclusion and perspectives

Throughout this thesis work a lot of different experiments were done and the ones that gave the most fruitful results were presented.

The first step in my thesis work was to modify a software that lets you select the data to be tracked by the INS before acquiring it and saving it in two separate text files. I was then able to test the acquisition program in real-life conditions during the first experiment. The first experiment, in protected conditions at the GET laboratory, where the goal was to familiarize with the SPATIAL's software and hardware, gave clear results on the temperature bias that should be taken into account for all future experiments and the influence of different sampling frequencies. Because of the length of this experiment I was then able to use this data and that recorded by a relative gravimeter and compare it to the theoretical signal of the Earth tides for that period at the coordinates of the *Géosciences et Environnement Toulouse* laboratory. By looking at the periodicity of the signals through a cross-wavelet coherence I was able to show that the SPATIAL INS/GNSS had a coherent periodicity with the semidiurnal and diurnal periods of the solid Earth tides. I obtained the same results with the CG-5 gravimeter, which had longer continuous data at the same sampling frequency where I could even see the periodicity of the fortnightly lunar cycle. By applying a low-pass filter to the theoretical model and the data from the INS/GNSS to remove all periods below 10 hours (which the XWT showed no correlation for) I obtained two signals that are highly coherent. Only the amplitude of the INS/GNSS signal is lower at some periods than that of the theoretical model. This can be caused by different phenomena like the ocean loading or changes in atmospheric pressure. When I looked at the pressure recorded by the INS/GNSS, there is a

decrease in pressure when the amplitude is lower. Although it is unlikely that the change in atmospheric pressure alone is responsible for the complete amplitude difference, it will be part of it.

A few months later, to continue the study of the temperature bias, the material was put in a drying oven to study the behavior at higher temperatures. The main observation was that the thermal drift of the SPATIAL doesn't necessarily follow the same linear law at higher temperatures, but at a threshold value, the increase in temperature can have an opposite effect on the recorded accelerations. The MOTUS IMU did not show any clear temperature bias compared to the SPATIAL INS/GNSS. Which means it can be used as a reference for the SPATIAL accelerations. The MOTUS alone would not be enough for mobile gravimetry as it does not record GPS coordinates because it's an IMU.

The Cammazes dam experiment took place between the period of the first and second temperature bias experiments so the MOTUS IMU was not yet available at this time. Throughout this experiment we drove from an altitude of 147 meters above sea level (GET), to an altitude of 580, before driving back to the laboratory, climbing and descending approximately 430 meters. Multiple stops were made to acquire measurements with the CG5-gravimeter, which was used as our reference instrument. One stop was made at an IGN reference point in order to transform the relative gravimetric measurements of the gravimeter to absolute values. Once the measurements for all stops are transformed to absolute values and the drift of the CG5 is corrected, I clearly see the influence of the altitude on the gravity values; the higher we are, the further from the center of Earth we are, the lower gravity is as it reduces with a factor of $\frac{1}{r^2}$. For every meter above the surface on Earth, the gravitational pull reduces with 0.3085 mGal/m, but this assumes there is only air between you and the surface, appropriately named the free-air anomaly. Because this isn't the case during this experiment as we're driving on the surface, the anomaly I observed for every meter was lower.
By taking the acceleration data from the INS/GNSS at the stops we made, and applying a rotation matrix to correct the position of the INS/GNSS since we would never be parked perfectly horizontal, I can compare it to the data of the gravimeter. I

had to calibrate the first value, at the GET laboratory, to the absolute value obtained, as the calibration was slightly off. When plotting this data I see multiple points where the values of the INS/GNSS does not match closely to the gravimeter, the points where it doesn't also happen to be the points where I had the least amount of measurements. The instrument had a sampling frequency of 1/30s, so depending on how quickly I would complete the measurements with the CG5-gravimeter, I would have more or less data. When I correct the temperature bias of this data, the values match much closer to that of the CG5, and also show the linear law between altitude and gravity.

Beside the influence of the altitude on gravity, the selected route was also chosen in order to determine if I can notice the effect of latitude changes on the value of gravity. By comparing the gravity anomaly when there was no change in latitude, and the theoretical values of gravity using the WELMEC formula, I showed that the difference in gravity anomaly when the latitude does change, corresponds to the theoretical value of the gravity change for the latitude change of approximately 0° 1'. This is a very small change in gravity because the latitude change is so small, so I was only able to detect it during this experiment using the gravimeter and not the INS/GNSS.

Although the INS/GNSS was continuously taking measurements throughout the day and being used for mobile gravimetry, the CG5-gravimeter that was used as a reference could not do this, and stops had to be made for its measurements. For this reason the next experiment that I'll go over is one where the continuous measurements of the INS/GNSS were used instead of only the periods when the vehicle was at rest.

During a period of 6 weeks a different experiment at the laboratory was performed to again study the influence of altitude changes, but this time much smaller variations of altitude. Multiple instruments would be used and swapped between a location on the ground floor and the roof. The gravimeter was again a good reference of the expected gravity changes and the MOTUS IMU, whose results were not influenced by the high temperature changes between both locations, presented results that were of the same magnitude as the gravimeter. The only results that did not have the

desired precision were from the periods when data was lost or from the IMU that was set to a much higher sampling frequency, increasing its noise too much.

To finish a mobile, airborne gravimetry experiment was performed. A fixed-wing drone was used whose maximum payload is only a few kilograms. This is a considerably smaller and lighter vehicle than some of the previous studies listed, with the goal being a more accessible solution for hard-to-reach regions while also remaining cheap that can be quickly deployed and cover a region.
The INS/GNSS are recording both the acceleration along three axes and the GPS coordinates, including the altitude. By converting the longitude, latitude and altitude to Cartesian coordinates the first and second derivative can be calculated to obtain the velocity and acceleration along the North-, East- and Down-axis (Earth's core being the center). The INS/GNSS being attached to the inside of the drone, means it's reference frame will be that of the drone and since it would be impossible for the drone to fly perfectly horizontal, using a rotation matrix with the pitch, roll and yaw recorded by the gyroscopes, I can convert the accelerations along the three axes to also be in the same NED-reference frame. The acceleration along the down-axis is of most interest to me because this is also the axis along which gravity is pulling. With the calculated and recorded accelerations in the same reference frame, they can be subtracted from one another in order to only have the acceleration of gravity remaining.
In practice though the amount of vibrations of the drone, caused by wind but also the motor, add too much noise to the data recorded by the INS/GNSS, which is strapped down to the drone. Because of this high noise the data needs to be filtered extensively using a low-pass filter. With the drone's velocity of 30 m/s, a low-pass filter of 120 seconds, similar to previous studies, would give me a spatial resolution of 1.8 kilometers, the approximate length and width of the region. Using the digital terrain model I was able to show the low effect of this region's topography on the gravitational signal.
From the first analysis of the complete flight data, I suspected the drift of the gyroscopes to be too high for accurate corrections of the drone's heading using a rotation matrix, which is why I filtered the complete data in order to only keep the parts where the drone was flying in a straight line, to minimize the inaccuracies added by the drone's gyroscopes. Applying the same method as before gives me a

clearer signal, where I obtain a correlation between the acceleration along the down axis and the changes in altitude throughout the flight. However this change in acceleration is still too high for the small altitude variations and are more likely to be a residual of the down acceleration when these altitude changes take place. Nonetheless, considering the high amplitude of the noise, which I was able to eliminate in some part by removing the power density of the frequencies of the signal when the motor was turned on but the drone was still at rest, the remaining signal has very small amplitude changes and with future improvements this precision of the signal could be improved on even more. Some of those changes and improvements will be explained next.

For future studies, while the duration of one hour for the total flight is good, since a large distance can be covered in that time and it limits the total temperature change, the trajectory of the flight should be different. Instead of a lot of small hippodromes at different angles, the drone should fly straight for a longer period of time to increase the size of the hippodromes and minimize the changes in altitude both on the straight line and for different hippodromes. While there were scientific reasons for the airflow experiment to use those trajectories, our experiment would have benefitted from having less different factors that could influence the gravitational signal.

The INS/GNSS should also record for a longer period (30-60 minutes) with the motor turned on while the drone is at rest, which would result in more data to filter the amplitudes of the frequencies caused by it. To help decrease the noise levels from the vibrations even more a thicker layer of rubber could be used to attach the instruments onto.
In order to improve the data of the kinematic accelerations, a ground station could be used for differential GPS (DGPS). This would result in more accurate data of the longitude, latitude and altitude data, which in turn improves the remaining signal when subtracted.

For future static experiments, the INS/GNSS should be installed somewhere isolated from noise caused by the presence of humans and with a more consistent temperature range. An example of this would be deep inside a cave, possibly even a few meters below the ground surface, where the temperature will be colder and vary

less (annual temperature range 12-14 °C) than inside a room at the laboratory. The absence of human activity will also reduce the recorded vibrations caused by cars driving, doors being opened and shut, people walking nearby or moving equipment etc.

The INS/GNSS should also be tested at lower temperatures (< 0°C) to study the effect on the acceleration recorded. Although a temperature range below 0°C would not be feasible during mobile experiments, it could be possible at a laboratory for static experiments if cold temperatures have a beneficial effect on the data.

A longer experiment should also be performed (30-60 days), with the INS/GNSS and CG-5 gravimeter both recording in the laboratory at 1 measurement/minute, in order to see if the INS/GNSS can even detect the periodicity of the solid Earth tides caused by the fortnightly lunar cycle (which was seen on the CG-5 data in this work). The amplitudes would be smaller than those caused by the (semi-)diurnal cycles, but would accentuate the INS/GNSS' capabilities even more, or present its limitations.

By installing the INS/GNSS near a lake, river or canal that presents high changes in volume throughout the seasons, if it can detect the small gravity changes caused by the increase, or decrease, in water levels, the experiment could prove the possibility of using it for hydrology, for example the detection of aquifers.

A mobile experiment can also be performed with the INS/GNSS installed on a gimbal. For example a repeat of the Cammazes dam experiment but instead of the INS/GNSS being strapdown inside, it is fixed on a gimbal which will keep the instrument at level throughout the day. By calculating accelerations from the navigational data and subtracting it from the data recorded by the accelerometers, the accelerations recorded while moving can be used and we're not just limited to the data when the van was at a stop.

Future technological advancements that will make these MEMS sensors more precise and less influenced by temperature variations will also improve this system.

Annex

$$
\begin{aligned}
&\mathrm{R}=\mathrm{R}_x(\alpha)R_y(\beta)R_z(\gamma)\\
&=\begin{bmatrix} cos\,\beta\,cos\,\gamma & cos\,\beta\,sin\,\gamma & -sin\,\beta \\ sin\,\alpha\,sin\,\beta\,cos\,\gamma-cos\,\alpha\,sin\,\gamma & sin\,\alpha\,sin\,\beta\,sin\,\gamma+cos\,\alpha\,cos\,\gamma & sin\,\alpha\,cos\,\beta \\ cos\,\alpha\,sin\,\beta\,cos\,\gamma+sin\,\alpha\,sin\,\gamma & cos\,\alpha\,sin\,\beta\,sin\,\gamma-sin\,\alpha\,cos\,\gamma & cos\,\alpha\,cos\,\beta \end{bmatrix}\begin{bmatrix}0\\0\\1\end{bmatrix}\\
&=\begin{bmatrix} -sin\,\beta \\ cos\,\beta\ sin\,\alpha \\ cos\,\beta\ cos\,\alpha \end{bmatrix}
\end{aligned}
$$

$$
\begin{aligned}
&\mathrm{R}=\mathrm{R}_y(\beta)R_x(\alpha)R_z(\gamma)\\
&=\begin{bmatrix} cos\,\beta\,cos\,\gamma-sin\,\alpha\,sin\,\beta\,sin\,\gamma & sin\,\gamma\,cos\,\beta+sin\,\beta\,sin\,\alpha\,cos\,\gamma & -sin\,\beta\ cos\,\alpha \\ -sin\,\gamma\,cos\,\alpha & cos\,\alpha\,cos\,\gamma & sin\,\alpha \\ cos\,\beta\,sin\,\alpha\,sin\,\gamma+sin\,\beta\,cos\,\gamma & -cos\,\gamma\,cos\,\beta\,sin\,\alpha+sin\,\gamma\,sin\,\beta & cos\,\beta\,cos\,\alpha \end{bmatrix}\begin{bmatrix}0\\0\\1\end{bmatrix}\\
&=\begin{bmatrix} -sin\,\beta\,cos\,\alpha \\ sin\,\alpha \\ cos\,\beta\ cos\,\alpha \end{bmatrix}
\end{aligned}
$$

$$
\begin{aligned}
&\mathrm{R}=\mathrm{R}_x(\alpha)R_z(\gamma)R_y(\beta)\\
&=\begin{bmatrix} cos\,\beta\,cos\,\gamma & sin\,\gamma & -cos\,\gamma\ sin\,\beta \\ sin\,\alpha\,sin\,\beta-cos\,\alpha\ cos\,\beta\ sin\,\gamma & cos\,\alpha\,cos\,\gamma & sin\,\alpha\ cos\,\beta+cos\,\alpha\ sin\,\beta\ sin\,\gamma \\ cos\,\beta\,sin\,\alpha\,sin\,\gamma+sin\,\beta\,cos\,\alpha & -cos\,\gamma\,sin\,\alpha & cos\,\beta\,cos\,\alpha-sin\,\alpha\ sin\,\beta\ sin\,\gamma \end{bmatrix}\begin{bmatrix}0\\0\\1\end{bmatrix}\\
&=\begin{bmatrix} -sin\,\beta\,cos\,\gamma \\ sin\,\alpha\ cos\,\beta+\ cos\,\alpha\ sin\,\beta\ sin\,\gamma \\ cos\,\alpha\ cos\,\beta-sin\,\alpha\ sin\,\beta\ sin\,\gamma \end{bmatrix}
\end{aligned}
$$

$$
\begin{aligned}
&\mathrm{R}=\mathrm{R}_y(\beta)R_z(\gamma)R_x(\alpha)\\
&=\begin{bmatrix} cos\,\beta\,cos\,\gamma & sin\,\gamma\ cos\,\alpha\ cos\,\beta+sin\,\alpha\ sin\,\beta & cos\,\beta\ sin\,\alpha\ sin\,\gamma-sin\,\beta\ cos\,\alpha \\ -sin\,\gamma & cos\,\alpha\,cos\,\gamma & sin\,\alpha\ cos\,\gamma \\ cos\,\gamma\,sin\,\beta & cos\,\alpha\ sin\,\beta\ sin\,\gamma-cos\,\beta\,sin\,\alpha & cos\,\alpha\,cos\,\beta+sin\,\alpha\ sin\,\beta\ sin\,\gamma \end{bmatrix}\begin{bmatrix}0\\0\\1\end{bmatrix}\\
&=\begin{bmatrix} cos\,\beta\ sin\,\alpha\ sin\,\gamma \\ sin\,\alpha\ cos\,\gamma \\ cos\,\alpha\ cos\,\beta+sin\,\alpha\ sin\,\beta\ sin\,\gamma \end{bmatrix}
\end{aligned}
$$

$$
\begin{aligned}
&\mathrm{R}=\mathrm{R}_z(\gamma)R_x(\alpha)R_y(\beta)\\
&=\begin{bmatrix} cos\,\beta\,cos\,\gamma+sin\,\alpha\ sin\,\beta\ sin\,\gamma & sin\,\gamma\ cos\,\alpha & cos\,\beta\ sin\,\alpha\ sin\,\gamma-sin\,\beta\ cos\,\alpha \\ sin\,\alpha\ sin\,\beta\ cos\,\gamma-cos\,\beta\ sin\,\gamma & cos\,\alpha\,cos\,\gamma & sin\,\alpha\ cos\,\beta\ cos\,\gamma+sin\,\beta\ sin\,\gamma \\ cos\,\alpha\,sin\,\beta & -sin\,\alpha & cos\,\alpha\,cos\,\beta \end{bmatrix}\begin{bmatrix}0\\0\\1\end{bmatrix}\\
&=\begin{bmatrix} cos\,\beta\ sin\,\alpha\ sin\,\gamma-sin\,\beta\ cos\,\gamma \\ sin\,\alpha\ cos\,\beta\ cos\,\gamma+sin\,\beta\ sin\,\gamma \\ cos\,\alpha\ cos\,\beta \end{bmatrix}
\end{aligned}
$$

$$
\begin{aligned}
&\mathrm{R}=\mathrm{R}_z(\gamma)R_y(\beta)R_x(\alpha)\\
&=\begin{bmatrix} cos\,\beta\,cos\,\gamma & sin\,\gamma\,cos\,\alpha+sin\,\alpha\ sin\,\beta\ cos\,\gamma & sin\,\alpha\ sin\,\gamma-cos\,\alpha\ cos\,\gamma\ sin\,\beta \\ -sin\,\gamma\ cos\,\beta & cos\,\alpha\,cos\,\gamma-sin\,\alpha\ sin\,\beta\ sin\,\gamma & sin\,\alpha\ cos\,\gamma+cos\,\alpha\ sin\,\beta\ sin\,\gamma \\ sin\,\beta & -sin\,\alpha\ cos\,\beta & cos\,\alpha\,cos\,\beta \end{bmatrix}\begin{bmatrix}0\\0\\1\end{bmatrix}\\
&=\begin{bmatrix} sin\,\alpha\ sin\,\gamma-sin\,\beta\ cos\,\alpha\ cos\,\gamma \\ sin\,\alpha\ cos\,\gamma+sin\,\beta\ sin\,\gamma\ cos\,\alpha \\ cos\,\alpha\ cos\,\beta \end{bmatrix}
\end{aligned}
$$

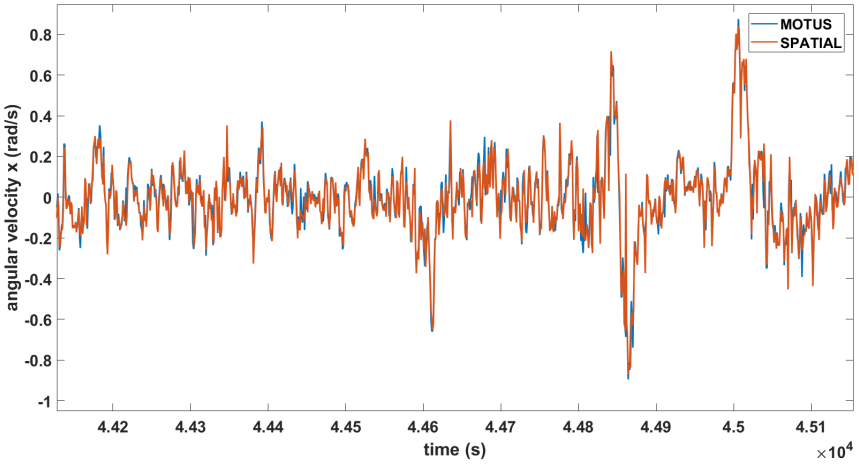

Angular velocity (rad/s) along the x-axis for both MOTUS and SPATIAL

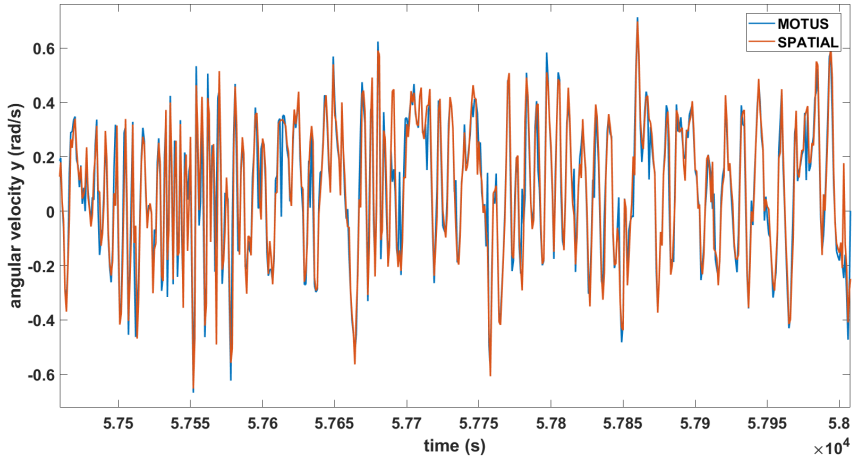

Angular velocity (rad/s) along the y-axis for both MOTUS and SPATIAL

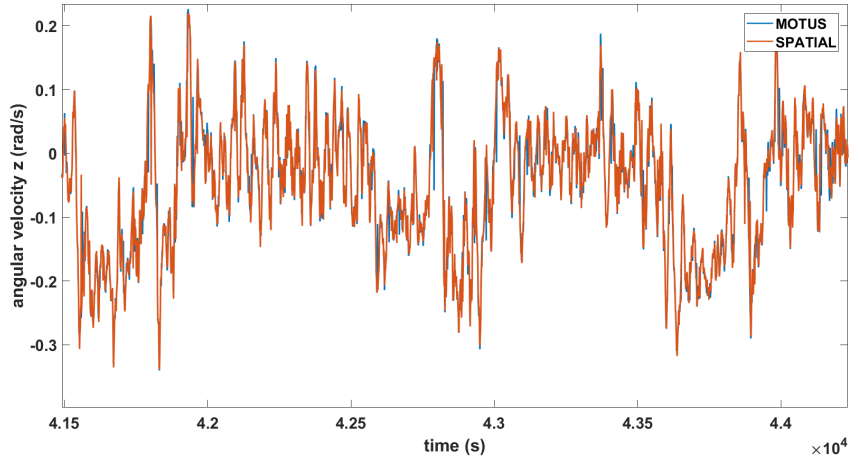

Angular velocity (rad/s) along the z-axis for both MOTUS and SPATIAL

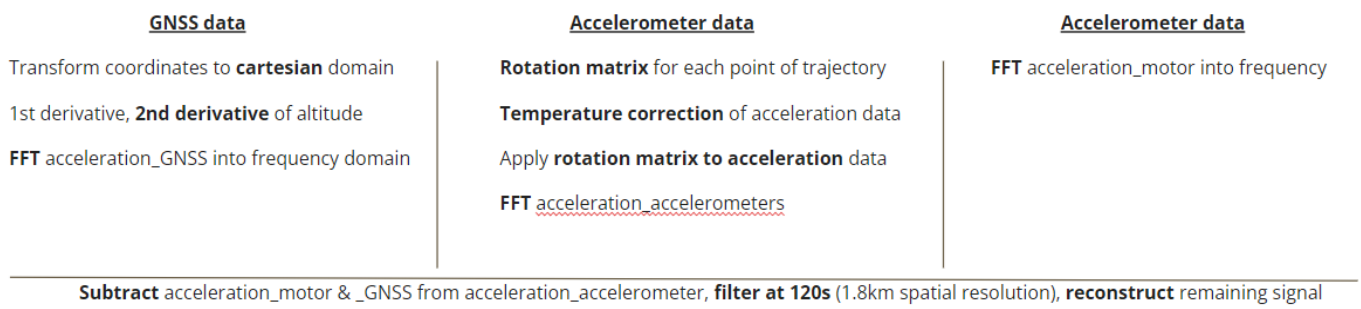

Breakdown of the different types of data obtained during the drone experiment and the breakdown of each type before being combined together to obtain the remaining signal

Bibliography

-Albarbar A., A. Badri, Jyoti K. Sinha, A. Starr, "Performance evaluation of MEMS accelerometers", Measurement, Volume 42, Issue 5, 2009, Pages 790-795, ISSN 0263-2241, https://doi.org/10.1016/j.measurement.2008.12.002.

-Andersen, O. B. (1995), Global ocean tides from ERS 1 and TOPEX/POSEIDON altimetry, J. Geophys. Res., 100(C12), 25249– 25259, doi:10.1029/95JC01389.

-Amalvict, M., J. Hinderer, J. Mäkinen, S. Rosat, and Y. Rogister. 2004. "Long-Term and Seasonal Gravity Changes at the Strasbourg Station and Their Relation to Crustal Deformation and Hydrology." Journal of Geodynamics 38 (3-5). Elsevier BV: 343–53.

-Ayres-Sampaio, D., Deurloo, R., Bos, M. *et al.* A Comparison Between Three IMUs for Strapdown Airborne Gravimetry. *Surv Geophys* **36**, 571–586 (2015). https://doi.org/10.1007/s10712-015-9323-5

-Barnes, Daniel, et al. "Earth gravitational model 2020." *AGU Fall Meeting Abstracts*. Vol. 2015. 2015

-Bassner, H., Killinger, R., Marx, M., Kukies, R., Aguirre, M., Edwards, C., & Harmann, H. P. (2000). Ion propulsion for drag compensation of GOCE. In *36th AIAA/ASME/SAE/ASEE Joint Propulsion Conference and Exhibit* (p. 3417).

-Becker, A., Kalman Filter, 2023 [*https://www.kalmanfilter.net*]

-Beirens B., Darrozes J., Ramillien G. and Seoane L., "Using an Inertial Navigation System for Gravimetric Applications. A Comparative Study Between an INS, a Microgravity Meter and a Seismometer," *2021 IEEE International Geoscience and Remote Sensing Symposium IGARSS*, Brussels, Belgium, 2021, pp. 7971-7973, doi: 10.1109/IGARSS47720.2021.9554499.

-Binley, A., S. S. Hubbard, J. A. Huisman,A. Revil, D. A. Robinson, K. Singha, andL. D. Slater (2015), The emergence of hydrogeophysics for improved understanding of subsurface processes over multiple scales,Water Resour. Res.,51, 3837–3866, doi:10.1002/2015WR017016

-Blakely, R. 1995. Potential Theory in Gravity and Magnetic Applications. Cambridge, United Kingdom: Cambridge University Press.

-Cai, Shaokun, Wu, Meiping, Zhang, Kaidong, Cao, JuLiang, Tuo, ZhaoHui, Huang, Yangming. (2013). The first airborne scalar gravimetry system based on SINS/DGPS in China. Science China Earth Sciences. 56. 2198-2208. 10.1007/s11430-013-4726-y.

-Cartwright D. E., 1977 "Ocean tides" Rep. Prog. Phys. 40 665 DOI 10.1088/0034-4885/40/6/002

-Chen, J., Cazenave, A., Dahle, C. et al. “Applications and Challenges of GRACE and GRACE Follow-On Satellite Gravimetry”. Surv Geophys 43, 305–345 (2022). https://doi.org/10.1007/s10712-021-09685-x

-W. T. Cochran *et al*., "What is the fast Fourier transform?," in *Proceedings of the IEEE*, vol. 55, no. 10, pp. 1664-1674, Oct. 1967, doi: 10.1109/PROC.1967.5957.

-Cooke, A.-K., Characterisation of a new mobile absolute quantum gravimeter : application in groundwater storage monitoring. Geophysics [physics.geo-ph]. Université Montpellier, 2020. English. ffNNT : 2020MONTG043ff. fftel-03211175f

-Crossley, D., J. Hinderer, and U. Riccardi. 2013. “The Measurement of Surface Gravity.” Reports on Progress in Physics 76 (4). IOP Publishing: 046101.

-**de Saint Jean, B. (2008):** Étude et développement d'un système de gravimétrie mobile.

-Din H., Iqbal F., Lee B., Design Approach for Reducing Cross-Axis Sensitivity in a Single-Drive Multi-Axis MEMS Gyroscope. Micromachines (Basel). 2021 Jul 29;12(8):902. doi: 10.3390/mi12080902. PMID: 34442524; PMCID: PMC8401296.

-**Farrell, J., Barth, M. (1998)**: The global positioning system and inertial navigation. New York: McGraw-Hill

-Featherstone W.E. (2003) Improvement to long-wavelength Australian gravity anomalies expected from the CHAMP, GRACE and GOCE dedicated satellite gravimetry missions. *Exploration Geophysics* **34**, 69-76. https://doi.org/10.1071/EG03069

-Fores, B., Champollion, C., Moigne, N. L., & Chery, J. (2017). Impact of ambient temperature on spring-based relative gravimeter measurements. *Journal of Geodesy*, *91*, 269-277.

-Fu, L.-L., Christensen, E. J., Yamarone, C. A., Lefebvre, M., Ménard, Y., Dorrer, M., and Escudier, P. (1994), “TOPEX/POSEIDON mission overview”, *J. Geophys. Res.*, 99(C12), 24369– 24381, doi:10.1029/94JC01761.

-Ekman, M. (1989): Impacts of geodynamic phenomena on system for height and gravity, Bulletin Geodesique, 63(3), pp. 281-296

-Flechtner, F., Reigber, C., Rummerl, R. et al. Satellite Gravimetry: A review of its realization. Surv Geophys 42, 1029-1074 (2021). doi: 10.1007/s10712-021-09658-0

-Francis, O. “Performance assessment of the relative gravimeter Scintrex CG-6”. J Geod 95, 116 (2021). https://doi.org/10.1007/s00190-021-01572-y

-Gaillot P. et al., 1997, The normalised anisotropic wavelet coefficient (NOAWC) Method: An image processing tool for multi-scale analysis of rock fabric, doi.org/10.1029/97GL01601

-Gerlach, C. and R. Dorobantu. “A Testbed for Airborne Inertial Geodesy : Terrestrial Gravimetry Experiment by INS / GPS.” 2004.

-Chambat F. et al., Flattening of the Earth: further from hydrostaticity than previously estimated, *Geophysical Journal International*, Volume 183, Issue 2, November 2010, Pages 727–732, https://doi.org/10.1111/j.1365-246X.2010.04771.x

-Chambodut, A., Panet, I., Mandea, M., Diament, M., Holschneider, M., & Jamet, O. (2005). Wavelet frames: an alternative to spherical harmonic representation of potential fields. *Geophysical Journal International*, *163*(3), 875-899.

-Godah, W., Szelachowska, M., & Krynski, J. (2019). On the recovery of temporal variations of geoid heights determined with the use of GGMs based on SST-hl data from non-dedicated gravity satellite missions. *Boletim de Ciências Geodésicas*, *25*.

-Grafarend, Erik W. "What is a geoid." *Geoid and its Geophysical Interpretation* (1994): 1-32.

-Grinsted, A., Moore, J.C., Jevrejeva, S. (2004) Application of the cross wavelet transform and wavelet coherence to geophysical time series, Nonlin. Processes Geophys., 11, 561–566, doi:10.5194/npg-11-561-2004

-Harriet C.P. Lau, Schindelegger, M. (2023): A journey through tides, Chapter 15 Solid Earth Tides, Elsevier, 2023, Pages 365-387, ISBN 9780323908511, https://doi.org/10.1016/B978-0-323-90851-1.00016-9.

-**Heiskanen, W. A. and Moritz, H.** Physical Geodesy. W. H. Freeman and Company, 1967.

-V.J. Inglezakis, S.G. Poulopoulos, E. Arkhangelsky, A.A. Zorpas, A.N. Menegaki, Aquatic Environment, Environment and Development, 2016, Pages 137-212, ISBN 9780444627339.

-Jastrow, R., and Pearse, C. A. (1957), Atmospheric drag on the satellite, J. Geophys. Res., 62(3), 413– 423, doi:10.1029/JZ062i003p00413.

-Jekeli, C. (2001): Inertial navigation systems with geodetic applications. Berlin-New York: Walter de Gruyter.

-Jevrejeva, S., Moore, J.C., Grinsted, A. (2003) Influence of the Arctic Oscillation and El Niño-Southern Oscillation (ENSO) on ice conditions in the Baltic Sea: The wavelet approach, J. Geophys. Res., 108(D21), 4677, doi:10.1029/2003JD003417

-Kaixin Luo, Juliang Cao, Chao Wang, Shaokun Cai, Ruihang Yu, Meiping Wu, Bainan Yang, Wenkai Xiang, (2022), First unmanned aerial vehicle airborne gravimetry based on the CH-4 UAV in China, Journal of Applied Geophysics 206(2022), 104835, ISSN 0926-9851

-Karl, J (1971), The Bouguer correction for spherical Earth, Geophysics 36: 761-762

-Kim Y and Bang H (2019) Introduction to Kalman Filter and Its Applications. Introduction and Implementations of the Kalman Filter. IntechOpen. DOI: 10.5772/intechopen.80600.

-Koks, D. (2022). A study of the EGM2008 model of Earth's gravitational field. The Journal of Navigation, 75(5), 1017-1034. doi:10.1017/S0373463322000480

-Koop, R. (1993). Global gravity field modeling using satellite gravity gradiometry.

-Kwon J.H., Jekeli C.(2001): A new approach for airborne vector gravimetry using GPS /INS. J. Geoid., 74 (10) (2000), pp. 690-700.

-Le Provost C. , Chapter 6 Ocean Tides, International Geophysics, Academic Press, Volume 69, 2001, Pages 267-303, ISSN 0074-6142, ISBN 9780122695452, https://doi.org/10.1016/S0074-6142(01)80151-0.

-Lin, C., Chiang, K. and Kuo, C. (2017): Development of INS/GNSS UA-Borne Vector Gravimetry System.
IEEE Geoscience and Remote Sensing Letters, 14 (2017) 315--333

-Marshall, S. J.: Meltwater run-off from Haig Glacier, Canadian Rocky Mountains, 2002–2013, Hydrol. Earth Syst. Sci., 18, 5181–5200, doi.org/10.5194/hess-18-5181-2014, 2014.

-Meyer, Y., & Roques, S. (1993). Progress in wavelet analysis and applications.

-McCarthy, D. , Petit, G. (2004): Frankfurt am Main: Verlag des Bundesamts für Kartographie und Geodäsie, 2004, 127 pp., ISBN 3-89888-884-3

-McKenzie, D., and Bowin, C. (1976), The relationship between bathymetry and gravity in the Atlantic Ocean, J. Geophys. Res., 81(11), 1903– 1915, doi:10.1029/JB081i011p01903.

-Middlemiss, R., Samarelli, A., Paul, D. et al. Measurement of the Earth tides with a MEMS gravimeter. Nature 531, 614–617 (2016). https://doi.org/10.1038/nature17397

-Newton, I. 1686. “Philosophiae Naturalis Principia Mathematica.” Reg. Soc. Praeses, London 2: 1–4.

-Niebauer, T. (2007). Gravimetric methods-absolute gravimeter: instruments concepts and implementation. *Geodesy*, *3*, 43-64.

-Lambert, W. D.. The International Gravity Formula. U.S. Coast and Geodetic Survey. 1945.

-Patton R. B., "Orbit Determination from Single Pass Doppler Observations," in *IRE Transactions on Military Electronics*, vol. MIL-4, no. 2/3, pp. 336-344, April-July 1960, doi: 10.1109/IRET-MIL.1960.5008246.

-Prasad, A., Middlemiss, R.P., Noack, A. *et al*. A 19 day earth tide measurement with a MEMS gravimeter. *Sci Rep* 12, 13091 (2022). https://doi.org/10.1038/s41598-022-16881-1

-Ramillien, G. Seoane, L., Darrozes, J. (2021): An Innovative Slepian Approach to Invert GRACE KBRR for Localized Hydrological Information at the Sub-Basin Scale. Remote Sens. 2021, *13*, 1824

-Ray, R.D., Rowlands, D.D. & Egbert, G.D. Tidal Models in a New Era of Satellite Gravimetry. Space Science Reviews 108, 271–282 (2003). doi.org/10.1023/A:1026223308107

-Reigber Ch. , H. Lühr, P. Schwintzer, “CHAMP mission status”, Advances in Space Research, Volume 30, Issue 2, 2002, Pages 129-134, ISSN 0273-1177, https://doi.org/10.1016/S0273-1177(02)00276-4.

-Rummel, R. (1980). *Geoid Heights, Geoid Height Differences, and Mean Gravity Anomalies from" low-low" Satellite-to-satellite Tracking: An Error Analysis* (p. 0049). Ohio State University, Department of Geodetic Science.

-**Sánchez L., Barzaghi R., Pearlman M., Heki K.**, Satellite gravimetry [ggos.org/item/satellite-gravimetry], 2023

-Schwartz, R., Lindau, A. (2002): Das europäische Gravitationszonen Konzept nach WELMEC für eichpflichtige Waagen (The new gravity zone concept in Europe for weighing instruments under legal control)

-Schwarz, K.-P., and Li, Y. C. (1996), What can airborne gravimetry contribute to geoid determination?, *J. Geophys. Res.*, 101(B8), 17873– 17881, doi:10.1029/96JB00819

-Seoane, L.; Ramillien, G.; Beirens, B.; Darrozes, J.; Rouxel, D.; Schmitt, T.; Salaün, C.; Frappart, F. Regional Seafloor Topography by Extended Kalman Filtering of Marine Gravity Data without Ship-Track Information. Remote Sens. 2022, 14, 169.

-SHEN, Y. Z., XSU, H. Z., & WU, B. (2005). Simulation of Recovery of Geopotential Model Based on the Intersatellite Acceleration Data in Low‐Low Satellite to Satellite Tracking Gravity Mission. *Chinese Journal of Geophysics*, *48*(4), 880-885.

-Skaloud J., Colomina I., Parés M. E., Blasquez M., Silva J. & Chersich M., A method of airborne gravimetry by combining strapdown inertial and new satellite observations via dynamic networks In: Freymueller, J.T., Sanchez, L. (eds) International Symposium on Earth and Environmental Sciences for Future Generations. International Association of Geodesy Symposia, vol 147. Springer, Cham. DOI: 10.1007/1345_2016_229

-Slabaugh, Gregory G. "Computing Euler angles from a rotation matrix." Retrieved on August 6.2000 (1999): 39-63.

-Smith, W. H. F., and D. T. Sandwell, Global seafloor topography from satellite altimetry and ship depth soundings, Science, v. 277, p. 1957-1962, 26 Sept., 1997.

-Sung-Ho, N.: Prediction of Earth tide, book: Basics of Computational Geophysics, DOI: 10.1016/B978- 524 0-12-820513-6.00022-9

-Teixeira da Encarnação, J., Visser, P., Arnold, D., Bezdek, A., Doornbos, E., Ellmer, M., Guo, J., van den Ijssel, J., Iorfida, E., Jaggi, A., Klokucnik, J., Krauss, S., Mao, X., Mayer-Gurr, T., Meyer, U., Sebera, J., Shum, C.K., Zhang, C., Zhang, Y. and Dahle, C. (2020). “Description of the multi-approach gravity field models from Swarm and GPS data”, Earth System Science data, DOI: 10.5194/essd-2019-158.

-Timmen, L. (2010). Absolute and relative gravimetry. *Sciences of Geodesy-I: Advances and Future Directions*, 1-48.

-Torrence, C., Compo, G.P. (1998) A practical guide to wavelet analysis, Bull. Am. Meteorol. Soc., 79, 61–78

-Torrence, C., Webster, P. (1999) Interdecadal changes in the ENSO-Monsoon System, J.Clim., 12, 2679–2690

-**Tscherning, C.,** The Geodesist's Handbook 1984. Association Internationale de Géodésie. 1984.

-**Van Camp, M., and Vauterin, P.,** "Tsoft: graphical and interactive software for the analysis of time series and Earth tides" Computers and Geosciences, 31(5) 631-640, doi:10.1016/ j.cageo.2004.11.015, 2005.

-van der Meijde M. , R. Pail, R. Bingham, R. Floberghagen, "GOCE data, models, and applications: A review", International Journal of Applied Earth Observation and Geoinformation, Volume 35, Part A, 2015, Pages 4-15, ISSN 1569-8432

-Verdun, J., Roussel, C., Cali, J., Maia, M., D'Eu, J.-F., Kharbou, O., Poitou, C., Ammann, J., Durand, F. & Bouhier, M.-É., (2022). Development of a Lightweight Inertial Gravimeter for Use on Board an Autonomous Underwater Vehicle: Measurement Principle, System Design and Sea Trial Mission. Remote Sensing. 14. 2513. 10.3390/rs14112513.

-Vörösmarty, C. J., C. Léveque, C. Revenga, R. Bos, C. Caudill, J. Chilton, EM. Douglas, et al. 2005. "Fresh Water." Millennium Ecosystem Assessment 1. Island Press, Washington: 165–207.

-Wang, L., Zhang, Z., & Sun, P. (2015). Quaternion-based Kalman filter for AHRS using an adaptive-step gradient descent algorithm. International Journal of Advanced Robotic Systems, 12(9), 131.

-Wang, R. (1997). Tidal response of the solid Earth. In: Wilhelm, H., Zürn, W., Wenzel, HG. (eds) Tidal Phenomena. Lecture Notes in Earth Sciences, vol 66. Springer, Berlin, Heidelberg. https://doi.org/10.1007/BFb0011456